A POINT-OF-CARE DIAGNOSTIC ASSAY UTILIZING THE
HYDRODYNAMICS OF AN EVAPORATING DROP

By

Joshua R. Trantum

Dissertation

Submitted to the Faculty of the

Graduate School of Vanderbilt University

in partial fulfillment of the requirements

for the degree of

DOCTOR OF PHILOSOPHY

in

Biomedical Engineering

August, 2013

Nashville, Tennessee

Approved:

Professor Frederick R. Haselton

Professor Todd D. Giorgio

Professor Craig L. Duvall

Professor David W. Wright

Professor Raymond L. Mernaugh

TABLE OF CONTENTS

ACKNOWLEDGEMENTS

LIST OF TABLES

LIST OF FIGURES

CHAPTER I

INTRODUCTION

The purpose of this work is to develop a diagnostic assay based on the hydrodynamics of an evaporating drop that may be used for point-of-care applications requiring a low-cost, simple-to-use, and rapid indicator of disease. This project follows three phases of development – an initial proof-of-concept design, characterization of underlying phenomena that affect assay performance, and an improved diagnostic design based on observations made in the first two phases. This work is organized into six chapters. The first introductory chapter summarizes the original specific aims of the project. The second chapter provides a rationale for the project and background information. The third chapter presents the initial proof-of-concept assay, "Biomarker-mediated disruption of coffee-ring formation as a low resource diagnostic indicator", which was published in *Langmuir* in 2012. The fourth chapter, "Cross-sectional tracking of particle motion in evaporating drops: flow fields and interfacial accumulation" investigates some features of the underlying hydrodynamic phenomena and was published in *Langmuir* in 2013. The fifth chapter presents an improved diagnostic design, "Biosensing in an evaporating drop", which is in the process of being submitted for publication. The sixth and final chapter summarizes the conclusions and future direction of the research.

Specific Aim 1: Design and characterize a proof-of-concept test of the coffee ring effect and a Ni(II)NTA biointerface as a detector of the poly-L-histidine peptide mimic of the malaria biomarker, *pf*HRP-II.

The goal of this aim is to demonstrate an assay design in which the presence of target biomarker causes the disruption of radial flow of a reporter particle in an evaporating drop. In this design, a positive test is visually distinguishable from a negative test due to a color shift in the final deposition patterns. The approach uses three particles, a reporter particle, magnetic

particle, and control particle. Therefore, colloidal stability, specific and non-specific interactions are important considerations for assay function and are investigated. A Ni(II)NTA biointerface and poly-L-histidine target were chosen in order evaluate the assay design under ideal conditions in the absence of salt and proteins, which are known to affect colloidal stability in evaporating drops.

Specific Aim 2: Identify and characterize major design parameters that affect particle motion during drop evaporation.

The goal of this aim is to characterize three-dimensional particle motion during drop evaporation and determine the parameters that promote radial flow fields and secondary flow fields. Optical coherence tomography is used to image dynamic changes in cross-sectional particle distribution. The effects of substrate material, particle density, solution additives, and relative humidity on particle motion were investigated and characterized.

Specific Aim 3: Implement and assess a revised assay design that improves the limit of detection in a solution with physiologic salinity.

The goal of this aim is to design and test a revised assay design that has a limit of detection at least 1000-fold better than the initial proof-of-concept assay and is not adversely affected by the presence of physiologic salinity. The assay design evaluated in Aim 1 does not achieve the limit of detection recommended by the World Health Organization for diagnosing malaria. Moreover, the initial proof-of-concept design was tested in an ideal solution lacking materials that may interfere with biomarker-mediated particle-particle assembly and/or interfere with the formation of particle rings in an evaporating drop. The revised assay design, however, relies on inwardly-directed flow fields observed in Aim 2 and should be capable of detecting biomarker in complex biological samples with an improved limit of detection.

Specific Aim 4: Demonstrate use of an antibody interface strategy.

The objective of this aim is to incorporate an antibody biointerface in the assay design to demonstrate potential utility in detecting biomarkers that don't readily coordinate metal chelates. An M13K07 bacteriophage and anti-M13K07 monoclonal antibody is used as a model system.

CHAPTER II

BACKGROUND AND SIGNFICANCE

Rationale

Point-of-care (POC) diagnostics are an important element of future healthcare delivery. Shifting confirmatory diagnosis and therapeutic response monitoring closer to the caregiver and patient and away from centralized laboratories has the potential to expedite treatment decisions, improve patient compliance, and reduce cost. The convenience, portability, and cost advantages of POC technologies also have the potential to bring diagnostic capability to environments where it is currently deficient or absent. These prospective benefits of POC diagnostics are clinically meaningful and applicable to all healthcare settings including both developed nations and resource-limited regions.[1]

Point-of-care diagnostic technologies can be broadly divided into two categories, resource-abundant and resource-limited, based on the availability of infrastructure and resources necessary for procurement, storage and operation. Access to reliable electricity, refrigeration, equipment, and trained personnel determines the suitability of a particular diagnostic technology for a given setting in terms of cost, simplicity, and performance. An example of a POC setting in a developed nation is the physician's office where access to basic infrastructure like electricity, refrigeration, and equipment is readily available. In this case, necessary reagents can be stored on site, testing is performed by a trained person, and the cost of the test is generally not a barrier to use. POC diagnostic technologies designed for this environment may rely on the availability of external instrumentation for test result measurement and interpretation. Moreover, the diagnostic test may be designed assuming the operator is trained to perform tasks like patient sample collection and handling, instrument operation, and test interpretation.

The implementation of point-of-care diagnostics in developed nations has been limited due, in part, to the prevalence and accessibility of advanced, clinical laboratories. The

convergence of several emerging trends, however, is likely to drive future demand for POC diagnostic tests in developed nations. The first of these trends is personalized medicine, in which companion diagnostics are developed in conjunction with therapeutic agents to assist with individual treatment decisions. On-going research in biomarker discovery and disease association provides an increasing number of molecular targets for use in diagnostic tests, which further increases the potential utility of POC testing. Additionally, escalating healthcare costs are expected to constrain the ways in which healthcare services are allocated and delivered. Finally, technological advances in miniaturizing biomarker detection strategies are rapidly improving the performance, cost, and operational complexity of diagnostic tests. For example, microfluidics, which is the processing and manipulation of small amounts of fluids (10^{-9} – 10^{-18}L), has the potential to improve the capability of POC diagnostics by reducing sample and reagent volumes, increasing reaction kinetics, and enabling integrated processes like sample preparation, purification, and test read-out in a single device.[2] Current microfluidic devices, however, tend to rely on external instruments for reading and interpreting the signal generated in the assay. A simplified, visually interpretable test read-out capable of being integrated with existing microfluidic architectures could facilitate the development of a self-contained, easy-to-use diagnostic test suitable for the POC setting of developed countries. The approaches taken in this research represent one possible means of achieving this goal.

However, nowhere do POC diagnostics hold more promise for improving healthcare delivery than resource-limited settings. Approximately half of the world's population lives in poverty, a third lack basic sanitation, and more than a billion people do not have access to basic healthcare services.[3] These people are predominantly concentrated in low-income, resource-limited regions of the world where infectious diseases are projected to account for over 22% of deaths by 2030 versus 3.6% in high income countries.[4] Infectious diseases, particularly malaria, tuberculosis, and HIV, disproportionately affect resource-limited regions of the world.[5] Sub-Saharan Africa exemplifies the challenges of dealing with this disease burden. This region often

lacks refrigeration, stable electricity, access to trained personnel, and calibrated and maintained equipment – the requisite infrastructure for standard clinical diagnostic tests. Due to dilapidated roads and dispersed population centers, the most effective confirmatory diagnosis must be performed in rural villages and townships. POC diagnostic tests must be designed with these constrained resources and rugged environments in mind. The diagnosis of malaria in sub-Saharan Africa illustrates the importance of simple, low-cost, confirmatory disease diagnosis at the point-of-care.

Malaria as an example

According to the World Health Organization, malaria alone caused 660,000 deaths from approximately 219 million cases in 2010.[6] The disease is caused by any one of four different types of protozoan parasites belonging to the genus *Plasmodium*. *P. falciparum* is the most prevalent malaria-causing species. Since the anopheles mosquito is the primary disease vector, malaria infects at pandemic levels in some tropical climates that are most conducive to mosquito infestations. Wealthier nations have successfully eradicated malaria by deploying mosquito containment strategies combined with effective anti-malarial therapies. However, lower-income and less developed countries incapable of such prophylactic measures remain highly vulnerable to the disease. The economic burden imparted on highly infected regions represents a positive feedback mechanism in which therapeutic costs absorb the scarce capital resources that could otherwise be used for preventative measures. The largest infectious disease burden is concentrated in Sub-Saharan Africa, where in 2010 malaria caused 594,000 deaths and was responsible for one in five childhood deaths.[6]

Standard of care treatment has changed over the last decade as the parasite that causes the disease has gained resistance to the most commonly prescribed therapeutic, chloroquine.[7] Early on, patients were ubiquitously treated without confirmatory diagnosis, contributing to drug resistance. To maximize the time over which newer anti-malarial drugs, for example artemisinin-

based combination therapies (ACT),[8] remain effective, confirmatory POC diagnosis is critical. Moreover, the high cost of the newer anti-malarials makes non-confirmatory diagnosis cost prohibitive. Malaria represents an enormous economic burden on the low-income countries of sub-Saharan Africa with as much as 40% of healthcare spending attributed to fighting malarial infections.[6] The World Health Organization estimates the malaria economic burden to be approximately 1.3% of gross domestic product in severely affected countries.[6] A low-cost, early, and accurate diagnosis is an essential component of an effective anti-malaria campaign.

Effective POC diagnostic strategies must consider the paucity of medical resources, including facilities, instrumentation, and trained personnel, in addition to potentially harsh storage and operating conditions. Early and accurate disease detection is most beneficially deployed at the front-line of infection. In this setting, the operator is likely to be an untrained layperson. Under these conditions an effective POC diagnostic must be low-cost, intuitive, and require minimal-to-no instrumentation for sample processing and test interpretation. The assay must also be sufficiently robust to withstand long and harsh storage conditions and to generate repeatable results in a sub-optimal operating setting. Over the last two decades much progress has been made toward the design and distribution of POC diagnostics for low-resource regions.[5] However, currently available POC diagnostics fall short of meeting the requirements necessary for effective and reliable detection of malaria.[9-12]

Current methods and limitations

The gold standard for malaria diagnosis is thick or thin smear microscopy, which can detect as low as 5-20 parasites per μL.[13] The instrumentation and training required, however, make microscopy methods unsuitable for POC diagnosis. The disease is most commonly diagnosed in the POC setting with an immunochromatographic strip, also known as a lateral flow assay or rapid diagnostic test (RDT). RDTs have also shown utility as rapid pregnancy tests as well as diagnosing sexually transmitted diseases, not just resource-limited applications like

malaria. This technology uses capillary flow to transport sample fluid across a substrate layer. The label, e.g. antibody-conjugated colloidal gold, binds the parasite biomarker, *pf*HRPII, and is captured by immobilized secondary antibody in the substrate layer which forms a concentrated, visible line as the sample flows down the strip (Figure 1). RDTs have a limit of detection of approximately 100 parasites per µL.[13,14] Recent evaluations of current RDTs highlight significant variability in their efficacy.[15] A recent study has found overall RDT sensitivity of 92.6% for samples containing 500-1,000 parasites per µL.[16] However, 84% of malaria infections occur with parasitemia levels < 500 parasites per µL.[17,18] RDT sensitivity falls to 89.3% and 53.9% for parasitemias of 100-500 and 0-100 parasites per µL, respectively. The WHO recommends a minimum 95% sensitivity for parasite densities of 100/µL.[19] The WHO's recommended sensitivity threshold corresponds to approximately 1nM of *pf*HRP-II.[20-23] Currently available RDTs do not exhibit adequate sensitivity for the most clinically meaningful parasitemia levels. In addition, because the test relies on antibodies, they require an unrealistically narrow storage temperature range of 1 – 40°C. The ideal POC diagnostic assay for malaria would be low cost, easy to use, rapid, and able to withstand harsh environmental conditions over long periods, and exhibit stable sensitivity and specificity within the WHO guidelines. However, RDTs have several limitations that prevent use in broader POC applications: (1) difficulty integrating with microfluidic processes for improved performance and more advanced functionality, (2) inability to multiplex, and (3) a limited ability to quantitate biomarker.[24]
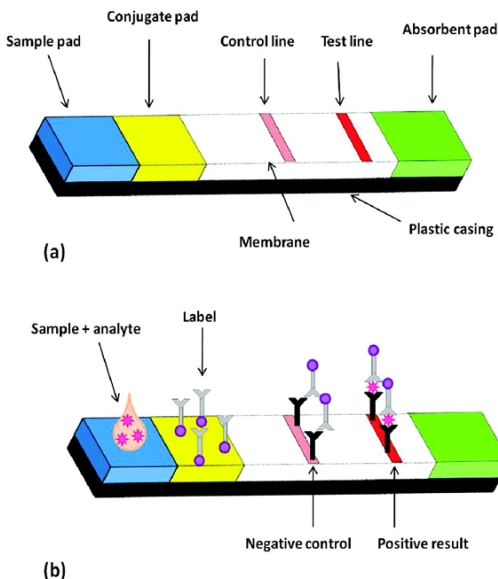
Figure 1. (a) Typical lateral flow immunoassay format. (b) Sample is applied to the sample pad. Analyte present in the sample binds to the antibody-conjugated label, then binds to the test line to return a positive result. If the analyte is absent, the label binds to the control line, generating a negative control result.[1]

Hydrodynamics of an evaporating drop

An evaporating drop represents a convenient environment for a simple, low-cost diagnostic assay due to the unique microfluidic flow that is naturally generated without an external power source. Water drops containing colloidal or dissolved materials have long been known to produce dried ring patterns upon evaporation on a surface. Some common manifestations of this occurrence include salt rings on pavement and coffee rings on countertops. First described by Deegan et al, this phenomenon, commonly referred to as the coffee ring effect, is caused by axisymmetric flow fields which transport particles in solution toward the edge.[25-27] Particles accumulate at the edge of the drop throughout evaporation and form a non-uniform deposition pattern upon drying. When the drop is first deposited on the substrate, colloidal particles present at the tri-phase interface, i.e. the wetted contact line, are pinned to the substrate as a result of surface tension effects and substrate topological heterogeneities.[27] Maximum evaporative flux occurs at the periphery due to greater volume of unsaturated gas into which

solvent molecules can disperse. The surface tension-dependent drop geometry is then constrained by a pinned contact line, unable to recede as solvent evaporates preferentially from the edge. An internal, radial flow is established to maintain mass conservation and replenish this lost solvent at the edge. Colloidal particles are transported by this flow and deposited at the edge resulting in a readily visible ring pattern. The phenomenon has been previously examined with respect to boundary conditions and the contribution of physical parameters on deposition patterns, such as pinning criteria,[28] particle size,[28] solvent type,[26] surfactant effects,[29] modeling evaporation flux,[30] microfluidic velocity vectors,[29,31,32] and imaging flow patterns.[33] In addition to the outwardly-directed coffee ring effect, evaporating drops may also contain secondary flow fields, known as Marangoni flow. This type of flow refers to eddy currents that result from a surface tension gradient at the air-liquid interface.[25,26,29,34,35] The non-uniform evaporative flux across the surface of a drop necessarily leads to a corresponding temperature and surface tension gradient.[25,26] This surface tension gradient, which is radially symmetric, causes fluid to flow from regions of low surface tension to high surface tension. Fluid transport across these temperature and surface gradients may result in a cross-sectional eddy current. We hypothesize that the unique hydrodynamics in an evaporating drop can be used as a basis for a diagnostic assay design.

Design considerations

An effective drop-based diagnostic system must take into account the dynamic nature of the evaporation process as well as the numerous variables that govern the physical and hydrodynamic properties of an evaporating drop. The two greatest contributing factors to colloidal stability are salt concentration and pH, both of which change with time as water evaporates from the drop. Dynamic changes in these variables affect both specific and non-specific interactions between particles. A prevailing theory originally described by Derjaguin, Landau, Verwey, and Overbeek, known as DLVO theory, quantitatively explains the balance of forces that maintain a dispersed colloid.[36-38] Ionic strength and pH both play a significant role in

maintaining colloidal stability by screening electric charges and determining particle surface charges, or zeta potentials. These variables therefore require careful consideration in establishing design parameters.

The choice of biorecognition element is also an important consideration because proper function is often dictated by solution conditions like salt and pH. Antibodies are an advantageous choice since they bind their cognate antigen with high affinity and specificity and can be designed against a large number of target biomarkers. Antibodies, however, function most effectively at physiologic pH and salinity. Antibodies also tend to degrade with multiple freeze/thaw cycles and long exposure to high temperatures. Other biorecognition elements, each with different advantages and disadvantages, include nucleic acids, peptides, aptamers, and metal chelates.

The physical properties of the particles and fluid, like particle size, density, and shape, as well as fluid viscosity and density, affect flow fields and to what extent the particles follow these flow fields. Stokes Law quantifies a particle's settling velocity in terms of radius, density, fluid density, and viscosity.[39] If the particles are too large or dense, they may settle to the substrate too quickly or slowly and compromise signal-to-noise in the assay.

Drop volume is an important variable because it determines, along with ambient temperature and relative humidity, total evaporation time and therefore the time-to-result. Drop volume also affects the size of the deposition pattern and therefore the visual detectability of the test result. The substrate surface is also a critical design feature for several reasons. First, the substrate must have sufficient surface heterogeneities to enable contact line pinning, a requisite condition for the coffee ring effect. The substrate hydrophobicity affects contact angle, which in turn influences the evaporative flux along the air-liquid interface and consequently internal flow patterns.[25,26] A hydrophobic surface may also promote non-specific interactions with other hydrophobic materials in solution. Finally, the thermal conductivity of the substrate has been shown to affect secondary flow patterns in an evaporating drop.[40]

11

Despite the challenges the dynamic nature of an evaporating drop presents for designing a diagnostic assay, the approach has the potential benefits of being simple for the user, easily interpretable, low cost, and relatively fast. These advantages underscore the potential utility a drop-based biosensor may have as a point-of-care diagnostic assay.

References

(1)   Gubala, V.; Harris, L. F.; Ricco, A. J.; Tan, M. X.; Williams, D. E.: Point of Care Diagnostics: Status and Future. *Analytical Chemistry* **2012**, *84*, 487-515.

(2)   Whitesides, G. M.: The origins and the future of microfluidics. *Nature* **2006**, *442*, 368-373.

(3)   Yager, P.; Edwards, T.; Fu, E.; Helton, K.; Nelson, K.; Tam, M. R.; Weigl, B. H.: Microfluidic diagnostic technologies for global public health. *Nature* **2006**, *442*, 412-418.

(4)   Mathers, C. D.; Loncar, D.: Projections of global mortality and burden of disease from 2002 to 2030. *Plos Medicine* **2006**, *3*.

(5)   Yager, P.; Domingo, G. J.; Gerdes, J.: Point-of-care diagnostics for global health. *Annu Rev Biomed Eng* **2008**, *10*, 107-44.

(6)   WHO: World Malaria Report 2012. World Health Organization, 2012; pp 195.

(7)   Bloland, P. B.: Drug resistance in malaria. CDC: Chamblee, GA, United States of America, 2001.

(8)   Nosten, F.; Brasseur, P.: Combination therapy for malaria: the way forward? *Drugs* **2002**, *62*, 1315-29.

(9)   *Malaria : evaluation of rapid diagnostic tests*, 2009.

(10)   Bell, D.; World Health Organization. Regional Office for the Western Pacific.: *The use of malaria rapid diagnostic tests*; 2nd ed.; World Health Organization: Geneva, 2006.

(11)   Wongsrichanalai, C.; Barcus, M. J.; Muth, S.; Sutamihardja, A.; Wernsdorfer, W. H.: A review of malaria diagnostic tools: Microscopy and rapid diagnostic test (RDT). *American Journal of Tropical Medicine and Hygiene* **2007**, *77*, 119-127.

(12)   World Health Organization. Regional Office for the Western Pacific.: *Malaria rapid diagnosis: making it work : informal consultation on field trials and quality assurance on malaria rapid diagnostic tests : meeting report 20-23 January 2003*; WHO Regional Office for the Western Pacific: Manila, 2003.

(13)   Gay, F.; Traore, B.; Zanoni, J.; Danis, M.; FribourgBlanc, A.: Direct acridine orange fluorescence examination of blood slides compared to current techniques for malaria diagnosis. *Transactions of the Royal Society of Tropical Medicine and Hygiene* **1996**, *90*, 516-518.

(14)   Singh, N.; Valecha, N.: Evaluation of a rapid diagnostic test, 'Determine malaria pf', in epidemic-prone, forest villages of central India (Madhya Pradesh). *Ann Trop Med Parasitol* **2000**, *94*, 421-7.

(15)   Perkins, M. D.; Bell, D. R.: Working without a blindfold: the critical role of diagnostics in malaria control. *Malaria Journal* **2008**, *7*.

(16)   Murray, C. K.; Bennett, J. W.: Rapid Diagnosis of Malaria. *Interdiscip Perspect Infect Dis* **2009**, *2009*, 415953.

(17)   Piper, R.; Lebras, J.; Wentworth, L.; Hunt-Cooke, A.; Houze, S.; Chiodini, P.; Makler, M.: Immunocapture diagnostic assays for malaria using Plasmodium lactate dehydrogenase (pLDH). *American Journal of Tropical Medicine and Hygiene* **1999**, *60*, 109-18.

(18)   Bustos DG, O. R., Negishi M, Kurimura T.: Evaluation of a new rapid diagnostic test "Determine Malraia Pf" against standard blood film, ICT Malaria P. f and ParaSight F. *Japanese J. Trop. Med. & Hyg.* **1999**, *27*, 417-425.

(19)   Bell, D.; Peeling, R. W.: Evaluation of rapid diagnostic tests: malaria. *Nat Rev Microbiol* **2006**, *4*, S34-8.

(20)   Minigo, G.; Woodberry, T.; Piera, K. A.; Salwati, E.; Tjitra, E.; Kenangalem, E.; Price, R. N.; Engwerda, C. R.; Anstey, N. M.; Plebanski, M.: Parasite-Dependent Expansion of TNF Receptor II-Positive Regulatory T Cells with Enhanced Suppressive Activity in Adults with Severe Malaria. *Plos Pathogens* **2009**, *5*.

(21)   Dondorp, A. M.; Desakorn, V.; Pongtavornpinyo, W.; Sahassananda, D.; Silamut, K.; Chotivanich, K.; Newton, P. N.; Pitisuttithum, P.; Smithyman, A. M.; White, N. J.; Day, N. P. J.: Estimation of the total parasite biomass in acute falciparum malaria from plasma PfHRP2 (vol 2, art. no. e204, 2005). *Plos Medicine* **2005**, *2*, 1047-1047.

(22)   Rajasekariah, G. H.; Martin, S. K.; Awinda, G.; Waitumbi, J.; Kifude, C.: Unified Parasite Lactate Dehydrogenase and Histidine-Rich Protein ELISA for Quantification of Plasmodium falciparum. *American Journal of Tropical Medicine and Hygiene* **2009**, *80*, 516-522.

(23)   Waitumbi, J. N.; Kifude, C. M.; Rajasekariah, H. G.; Sullivan, D. J.; Stewart, V. A.; Angov, E.; Martin, S. K.; Diggs, C. L.: Enzyme-linked immunosorbent assay for detection of Plasmodium falciparum histidine-rich protein 2 in blood, plasma, and serum. *Clinical and Vaccine Immunology* **2008**, *15*, 1012-1018.

(24)   Chin, C. D.; Linder, V.; Sia, S. K.: Lab-on-a-chip devices for global health: Past studies and future opportunities. *Lab on a Chip* **2007**, *7*, 41-57.

(25)   Deegan, R. D.: Pattern formation in drying drops. *Physical Review E* **2000**, *61*, 475-485.

(26)   Deegan, R. D.; Bakajin, O.; Dupont, T. F.; Huber, G.; Nagel, S. R.; Witten, T. A.: Contact line deposits in an evaporating drop. *Physical Review E* **2000**, *62*, 756-765.

(27)   Deegan, R. D.; Bakajin, O.; Dupont, T. F.; Huber, G.; Nagel, S. R.; Witten, T. A.: Capillary flow as the cause of ring stains from dried liquid drops. *Nature* **1997**, *389*, 827-829.

(28)   Sangani, A. S.; Lu, C. H.; Su, K. H.; Schwarz, J. A.: Capillary force on particles near a drop edge resting on a substrate and a criterion for contact line pinning. *Physical Review E* **2009**, *80*.

(29)   Hu, H.; Larson, R. G.: Analysis of the effects of Marangoni stresses on the microflow in an evaporating sessile droplet. *Langmuir* **2005**, *21*, 3972-3980.

(30)   Hu, H.; Larson, R. G.: Evaporation of a sessile droplet on a substrate. *Journal of Physical Chemistry B* **2002**, *106*, 1334-1344.

(31)   Hu, H.; Larson, R. G.: Analysis of the microfluid flow in an evaporating sessile droplet. *Langmuir* **2005**, *21*, 3963-3971.

(32)   Harris, M. T.; Widjaja, E.: Particle deposition study during sessile drop evaporation. *Aiche Journal* **2008**, *54*, 2250-2260.

(33)   Kajiya, T.; Kaneko, D.; Doi, M.: Dynamical Visualization of "Coffee Stain Phenomenon" in Droplets of Polymer Solution via Fluorescent Microscopy. *Langmuir* **2008**, *24*, 12369-12374.

(34)   Barash, L. Y.; Bigioni, T. P.; Vinokur, V. M.; Shchur, L. N.: Evaporation and fluid dynamics of a sessile drop of capillary size. *Physical Review E* **2009**, *79*.

(35)   Hu, H.; Larson, R. G.: Marangoni effect reverses coffee-ring depositions. *Journal of Physical Chemistry B* **2006**, *110*, 7090-7094.

(36)   Derjaguin, B. L., L: Theory of the stability of strongly charged lyophobic sols and the adhesion of strongly charged particles in solutions of electrolytes. *Acta Physico Chemica URSS* **1941**, *14*.

(37)   Derjaguin, B.; Landau, L.: Theory of the Stability of Strongly Charged Lyophobic Sols and of the Adhesion of Strongly Charged-Particles in Solutions of Electrolytes. *Progress in Surface Science* **1993**, *43*, 30-59.

(38)   Derjaguin, B. V.: Problems of Adhesion. *Progress in Surface Science* **1994**, *45*, 223-231.

(39)   Brenner, H.: The slow motion of a sphere through a viscous fluid towards a plane surface. *Chem Eng Sci* **1961**, *16*, 242-251.

(40)   Ristenpart, W. D.; Kim, P. G.; Domingues, C.; Wan, J.; Stone, H. A.: Influence of substrate conductivity on circulation reversal in evaporating drops. *Physical Review Letters* **2007**, *99*.

CHAPTER III

BIOMARKER-MEDIATED DISRUPTION OF COFFEE-RING FORMATION

AS A LOW RESOURCE DIAGNOSTIC INDICATOR

Joshua R. Trantum[1]
David W. Wright[2]
Frederick R. Haselton[1]

[1]Department of Biomedical Engineering
[2]Department of Chemistry
Vanderbilt University
Nashville, Tennessee

Abstract

The ring pattern resulting from the unique microfluidics in an evaporating coffee drop is a well-studied mass transport phenomenon generating interest in the research community mostly from a mechanistic perspective. In this report, we describe how biomarker-induced particle-particle assemblies, magnetic separation, and evaporation-driven ring formation can be combined for simple pathogen detection. In this assay design, the presence of biomarkers causes self-assembly of a magnetic nanoparticle and a fluorescently-labeled micron-sized particle. A small spherical magnet under the center of the drop prevents these assemblies from migrating to the drop's edge while a non-reactive control particle flows to the edge forming a ring pattern. Thus the presence or absence of biomarker results in distinctly different distributions of particles in the dried drop. Proof-of-principle studies using poly-L-histidine, a peptide mimic of the malaria biomarker *pf*HRPII, show that the predicted particle distributions occur with a limit of detection of approximately 200-300nM.

Introduction

Deegan et al. were the first to elucidate evaporation-driven capillary flow as the underlying mechanism of ring formation in a drying drop.[1-3] There have since been many studies of how various physical parameters affect ring deposition patterns, such as pinning criteria,[4] particle size,[4] solvent type,[2] surfactant effects,[5] and modeling evaporation flux,[6] microfluidic velocity vectors,[5,7,8] and imaging flow patterns.[9] Efforts to understand conditions that promote or obstruct ring patterns in colloidal drops have mostly been applied to eliminate its occurrence, which causes deleterious effects in applications as wide ranging as microarray deposition, ink jet printing, and paint manufacturing. For example, Yunker et al.[10] recently showed that sufficiently high aspect ratio ellipsoidal particles at the air-liquid interface arrests outward migration resulting in a homogenous film deposition pattern, Bhardwaj et al.[11] demonstrated that deposition patterns can be tuned by controlling pH-dependent particle-substrate forces, and Wong et al.[12] demonstrated how the phenomenon can be used for chromatographic separation of nano-sized colloidal particles. Some recent studies have also investigated pattern formation in drying drops containing biological material.[13-16] However, efforts to exploit the visual appeal of this phenomenon for disease detection have not been described.

Particles in an evaporating colloidal drop migrate to the drop's edge forming a ring on the underlying substrate. As originally described by Deegan et al., colloidal particles present at the tri-phase interface, i.e. the wetted contact line, are pinned to the substrate as a result of surface tension effects and substrate topological heterogeneities.[3] Maximum evaporative flux occurs at the periphery due to greater volume of unsaturated gas into which solvent molecules can disperse. The surface tension-dependent drop geometry is then constrained by a pinned contact line, unable to recede as solvent evaporates preferentially from the edge. An internal, radial flow is established replenishing lost solvent at the edge. Colloidal particles are transported by this flow and deposited at the edge resulting in a readily visible ring pattern (Figure 1). We hypothesize that this ring pattern can be controlled by biomarker-mediated interference of particle migration

18

to the edge and therefore disruption of ring formation. For example, biomarker assembly of a colored particle to a magnetic iron oxide particle immobilized in the drop center by an applied magnetic field should cause a shift in the color pattern. If true, the coffee ring effect could potentially be developed as a self-contained visual indicator of biomarker-mediated binding events with potential diagnostic utility in a low resource setting.

We have chosen malaria detection as a model system for proof-of-concept studies because it has a well-identified biomarker, *Plasmodium falciparum* histidine rich protein (*pf*HRPII), and biomarker mimics are both well-characterized and readily available.[17-19] The most common malaria-causing parasite, *P. falciparum*, secretes *pf*HRPII into the serum of infected individuals at levels ranging from 10^7 to 10^{10} molecules per µL depending on the degree of parasitemia. For initial proof-of-concept studies, we chose poly-L-histidine (PLH) as a *pf*HRPII biomimic. Our objective is to determine if we can use the unique microfluidics present in an evaporating drop to detect the presence of biomarkers in this model system.
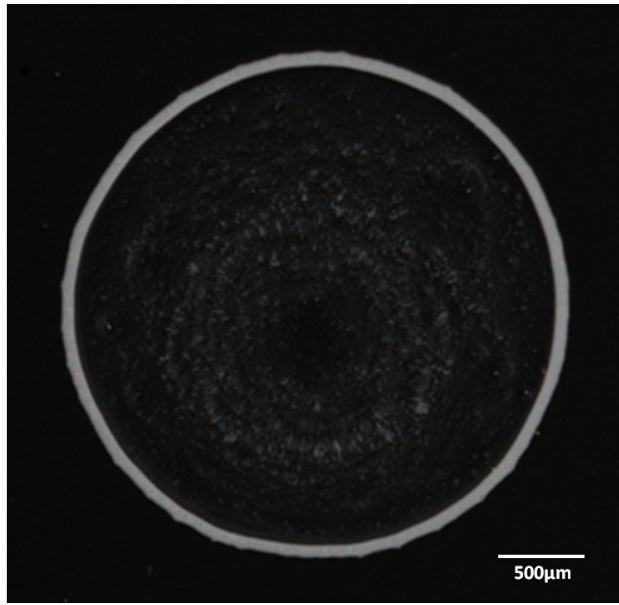
Figure 1. Photograph of the characteristic "coffee ring" particle deposition pattern after evaporation of a 3μL drop containing 10^6, 1μm white latex particles taken with a Nikon D100 camera using an AF Micro Nikkor lens and extension tube. The drop has a diameter of approximately 3mm.

Experimental Methods

Particle Functionalization

    PEGylation.

Carboxylated polystyrene beads, mean diameter 0.97μm, were obtained from Bang's Laboratories with two different fluorescence excitation/emission profiles: 540/600 and 480/520. The beads were washed by centrifugation three times (4.6g) and re-suspended in PBS (pH 7.2) at stock concentration (1.975×10^{10} per mL). Particles were made sulfhydryl reactive by coupling N-β-maleimidopropionic acid hydrazide (BMPH, Fisher Scientific) via 1-ethyl-3(3-dimethylaminopropyl) carbodiimide (EDC, Sigma Aldrich). The BMPH was dissolved in PBS (pH 7.2) and added to the particle suspension at a ten-fold molar ratio to carboxyl sites. EDC dissolved in 100mM MES buffer (pH 4.9) was immediately added to the reaction volume to yield a fifty-fold molar excess relative to carboxyl sites. The reaction volume incubated at least two hours. Particle suspensions were then washed three times via centrifugation and re-suspended in PBS (pH 7.2). The red control particles were pegylated by reacting with thiol-PEG-methyl (Quanta Biodesign Ltd) dissolved in PBS (pH 7.2) to yield a ten-fold molar excess relative to maleimide groups. The suspension incubated for at least two hours, was washed three times via centrifugation, and re-suspended in deionized water. The green particle suspension was reacted with thiol-PEG-carboxylic acid (Quanta Biodesign Ltd) dissolved in PBS (pH 7.2). The suspension incubated for two hours, was washed three times via centrifugation, and was re-suspended in MES buffer (pH 4.9).

    Conjugation of NTA to polystyrene particles

EDC and N-hydroxysulfosuccinimide (NHS, Sigma Aldrich) were together dissolved in MES buffer (pH 4.9) at a molar ratio of 1:2.5. The EDC/NHS solution was added to the reaction volume (in MES) to yield a ten-fold molar excess of EDC to carboxyl sites. The solution reacted for fifteen minutes at room temperature, washed three times via centrifugation, and re-suspended in PBS (pH 7.4). A solution of nitrilotriacetic acid (Sigma Aldrich) in PBS (pH 7.2) was added to

yield a ten-fold molar excess relative to active sites. The reaction volume reacted for two hours, washed via centrifugation, and re-suspended in 100mM HEPES buffer (pH 7.2).

Ni^{2+} *Charging of polystyrene-PEG-NTA particles.*

Nickel chloride was dissolved in deionized water and added to the PEG-NTA-conjugated particles in 100mM HEPES buffer (pH 8) to yield a ten-fold nickel molar excess over NTA groups. The reaction volume reacted two hours, was washed five times via centrifugation, and re-suspended in deionized water.

Ni^{2+} *Charging of iron oxide-NTA particles.*

Dextran-stabilized iron oxide particles having a mean diameter of 250nm and surface-modified with NTA were obtained from Micromod Gmbh. The particles were washed three times via magnetic separation (or centrifugation) and re-suspended in deionized water (0.2% Tween 20) at stock concentration (4.9×10^{11} per mL). Nickel chloride was dissolved in deionized water and added to the iron oxide-NTA particles to yield a ten-fold nickel molar excess over NTA groups. The reaction volume reacted for two hours, was washed five times via centrifugation, and re-suspended in deionized water. The reaction volume reacted for two hours, was washed five times via centrifugation, and re-suspended in deionized water.

Particle Characterization

Particle concentration and size distributions of polystyrene particles were measured using a Beckman Coulter Multisizer 3 coulter counter. One microliter of stock particles was diluted in 20mL of Isoton II diluent (Beckman Coulter) and measured using a 30μm aperture. Iron oxide particle size distribution was measured using dynamic light scattering (Malvern Zetasizer NanoZS) by diluting 20μL of stock particle solution in 1mL deionized water. Polystyrene and iron oxide particle surface modification was verified by measuring zeta potentials (Malvern Zetasizer NanoZS) of the functionalized particles versus non-functionalized. For all zeta potential measurements, 20μL of particles were diluted in 1mL of 1mM aqueous NaCl (pH 7.76).

22

Nickel coordination to the NTA ligand was verified by inductively coupled plasma optical emission spectroscopy (ICP-OES). Nickel was stripped from the NiNTA functionalized particles following two-hour incubation in 2% nitric acid. Particles were removed from the nitric acid via a 2µm syringe filter. Nickel content was measured on an Optima 7000 ICP-OES.

Experimental Protocol

The green PS-PEG-NiNTA particle (3.86×10^6 per µL in H_2O) was mixed 1:1 with the magnetic nanoparticle (1×10^7 per µL in H_2O). Poly-l-histidine (PLH) or poly-l-aspartic acid (PLD) was then added at a given concentration. Six concentrations of target or control were assessed: 1.74µM, 870nM, 435nM, 218nM, 109nM, 0nM. Following thirty minute incubation at room temperature, the red particle (3.86×10^6 per µL) was added to the reaction volume in equal part to the other components. Particle concentrations were determined based on the number required to generate a visible ring and the optimal signal-to-noise output at [target] = 435nM (supporting information). A glass slide was cleaned in an acid wash containing 70% ethanol / 30% hydrochloric acid (1N) for two hours, rinsed with deionized water, and dried under nitrogen gas. Drops (3µL) were deposited in triplicate on the slide, each centered over a 3mm spherical magnet (neodymium magnet with 179 mT field strength, Engineered Concepts) with the magnetic pole oriented orthogonal to the slide. Upon complete evaporation, the deposition patterns were imaged under fluorescence microscopy (Nikon TE2000U inverted fluorescence microscope), fluorescence intensity in pre-defined areas of interest (supporting information) was measured using Image Pro software (v7). Due to position variability during manual drop deposition the location of settled magnetic particles relative to the ring varied from drop to drop. Areas of interest (AOI) in the software program were therefore manually moved to the appropriate location in the image prior to taking the measurement. Total and mean intensities (green channel only) were recorded. Mean background noise was subtracted from each respective area of interest, and the signal metric was calculated as f_{center} / $f_{ring-center}$ (where f = background-adjusted fluorescence

intensity). The three calculations were averaged per data point. The experiment was conducted in triplicate and signal values averaged and plotted. In addition to center signal, a ring signal calculation was made by measuring the green fluorescence intensity in the ring as a percentage of total ring fluorescence intensity (green + red).

Particle tracking

The relationship between magnetic field strength and iron oxide particle motion was quantified by tracking the velocity of individual iron oxide particles near the drop perimeter both with and without the magnet in place. Colloidal suspensions in water were prepared using the same particle types and concentrations as described above. Deionized water was added to the suspension in place of the PLH or PLD solutions that were added according to the sample preparation described in the Experimental Protocol section. Three microliter volumes were deposited on a clean glass slide and centered over the magnetic field. Videos of particle motion were recorded using a 20x objective on a Nikon TE2000U inverted microscope with a charge coupled device (CCD) camera (Hamamatsu Photonics model C7780-20). Individual particle motion was tracked using Image Pro software (v.7). Average particle velocity was calculated from the motion of ten particles tracked over a period of five seconds. Magnetic field strength was measured at the drop perimeter with a gaussmeter (LakeShore, model 421).

A similar experiment was conducted using the same particle types, particle concentrations, and magnet but with larger drop volumes to determine the approximate drop volume and radius at which iron oxide particles at the perimeter do not migrate to the drop's center. After a sample volume was deposited on a clean glass slide, iron oxide particles at the drop's perimeter were tracked as the magnet was placed at the drop's center. The experiment was repeated for drop volumes ranging from 10μL to 40μL.

Results and Discussion

Details of the assay design are shown in Scheme 1. A biological sample is mixed with a solution containing three different particles. Two of these particles, a magnetic particle and a biomarker indicator particle (green), have interfaces designed to interact with the disease biomarker, while a third is a non-reactive control particle (red). Biomarkers present in solution cross-link the two surface functionalized particles (magnetic and indicator) inducing self-assembly. A small volume of the particle suspension is deposited on a glass substrate centered above a magnetic field and the non-reactive control particles (red) are transported to the edge forming a red ring. The indicator particles (green) are either transported to the edge in the absence of biomarker or magnetically pulled to the center in the presence of biomarker. The co-location of indicator (green) and control (red) particles at the edge creates a yellow ring (left panel) and indicates a negative result while a red ring and a green center spot indicates a positive result (right panel). As Scheme 1a illustrates, the assay generates an easily interpretable pattern.

Experimentally observed changes (Figure 2) are in general agreement with the theoretical model presented in Scheme 1a (top view). In the presence of the malaria surrogate, poly-L-histidine (PLH, top row), the indicator particle (green) is cross-linked to the magnetic particle and consequently pulled to the center resulting in a red ring and green center. In the absence of PLH (bottom row), both control (red) and indicator (green) particles flow to the edge creating a yellow ring leaving only magnetic particles in the drop center as seen in the corresponding phase contrast image. Poly-L-aspartic acid (PLD) is used as a negative control peptide (bottom row). In addition to the color changes seen in the fluorescence images, the phase images also show the change in particle distribution. The PLH (top row) phase contrast image shows a greater number of particles in the center relative to the PLD (bottom row) image as a result of magnetic particle-green particle assemblies. The PLH and PLD phase contrast images contain the same number of magnetic particles, however the presence of the cross-linked green particle in the PLH center results in a greater number of total particles at the drop center compared to the PLD sample.
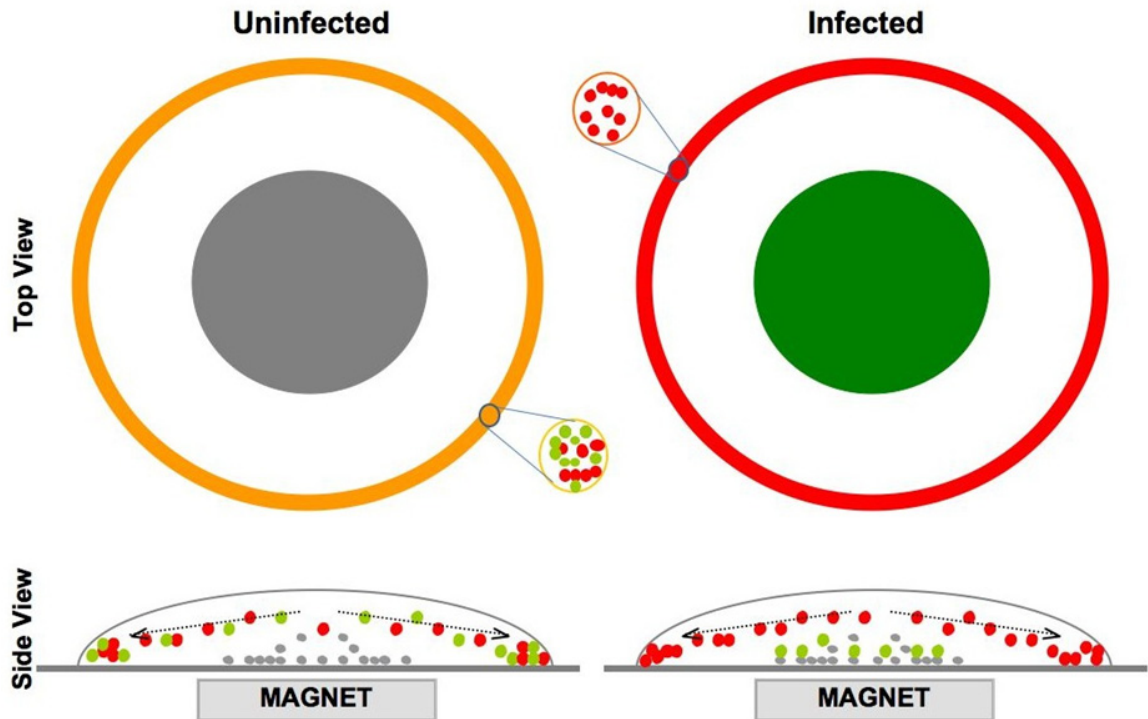
Scheme 1a. Coffee ring assay schematic. As illustrated in the left panel, in the absence of biomarker, green particles are free to migrate to the edge, and co-location of red and green particles at the edge yields a yellow ring. In the right panel, the presence of biomarker cross-links green and iron oxide particles creating a green center spot and a ring color change from yellow to red.
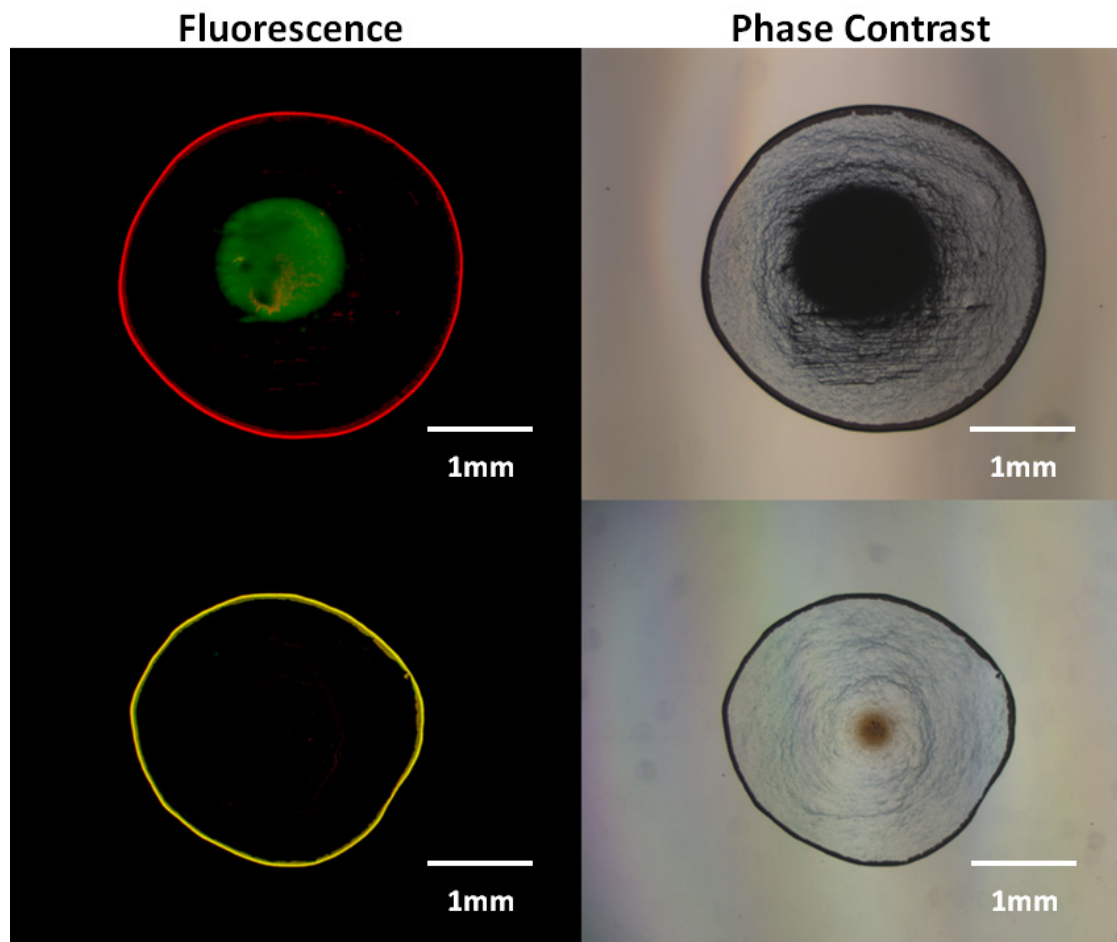
Figure 2. **Fluorescence (left panels) and phase images (right panels) of particle deposition patterns observed with poly-L-histidine target (top row) and poly-L-aspartic acid control (bottom row). Fluorescence images show the change in color triggered by the presence of biomarker (1.74μM) from a red ring/green center to a yellow ring without biomarker. Phase images show that magnetic particles are concentrated in the drop center in both positive and negative assays. The center spot in the positive phase contrast image (upper right) consists of both iron oxide and green polystyrene particles resulting in a larger mass spot than the corresponding negative image (lower right).**

The assay demonstrates biomarker concentration dependence with peptide target (Figure 3). Images obtained with the addition of PLH (+, left panels) and PLD (- control, right panels) are shown for peptide concentrations of 1.74μM (top panels) to zero (bottom panels) using the optimized parameters determined in prior experiments (supplementary information). At the highest concentration, the biomarker-induced pattern is similar to that observed in Figure 2. Biomarker-induced assemblies reduce the number of green indicator particles at the drop edge and increase the number of green indicator particles in the center of the drop. As shown in the left panels, decreasing PLH concentration causes the ring color to become progressively more orange/yellow in color due to co-location of a greater number of green indicator particles and red control particles at the drop edge. A greater number of indicator particles at the drop edge reduces the number of indicator particles in the drop center, reducing the positive signal. In contrast, the color patterns of all negative samples maintain a constant orange/yellow ring appearance with no indicator particles in the drop center. At PLH concentrations below 218nM the positive becomes qualitatively indistinguishable from the negative, indicating the visual limit of detection for the system as currently configured. A consistent pattern similar to that observed with a PLH concentration of zero was observed at all concentrations of the non-specific control peptide, PLD.
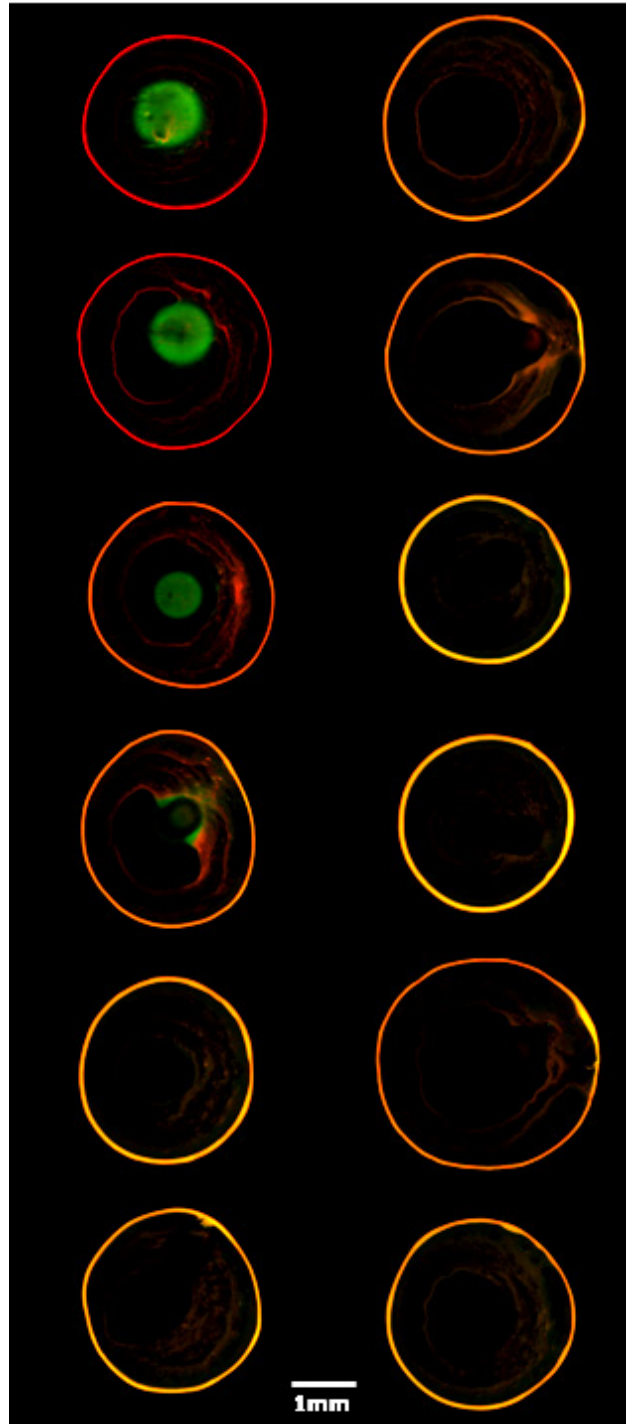
Figure 3. Change in coffee ring fluorescence images produced by a decrease in target concentration. Positive (PLH), shown in the left column, and negative (PLD), in the right column. Concentration decreases down the rows: 1.74µM, 870nM, 435nM, 218nM, 109nM, 0nM. Signal, defined as a green center and a ring color shift from orange/yellow to red, decreases with decreasing PLH concentration.
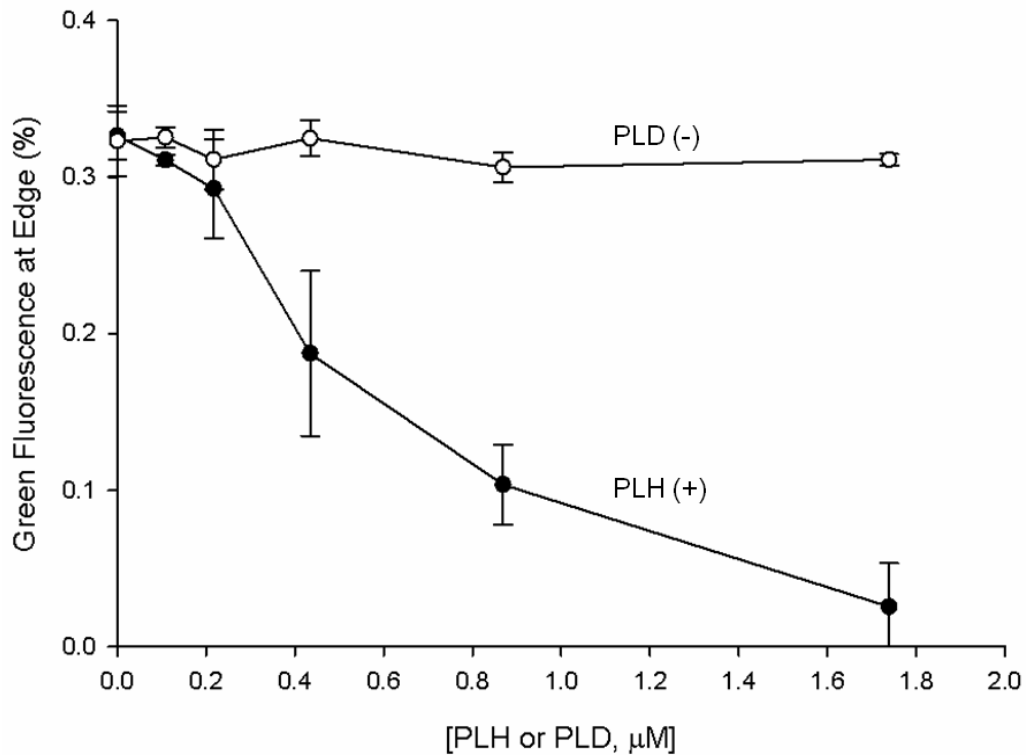
Figure 4. Edge-based signal measurement as a function of biomarker and control peptide concentrations. Green fluorescence intensity as a percentage of green + red fluorescence intensity at the ring is plotted against [PLH],•, or [PLD],o. N=3, mean ± 1 s.d.

Quantification of the images in Figure 3 shows that the limit of detection with this design is between 200 and 300nM. Positive and negative assay particle deposition patterns were measured under fluorescence microscopy and quantified using two different methods. Neglecting particles distributed in the drop center, signal generation at the ring was calculated by measuring the ratio of green to green+red fluorescence at the drop edge and plotted as a function of peptide concentration (Figure 4). When all indicator particles are removed from the ring, this value should approach zero. Alternatively, center signal was calculated neglecting the particles distributed at the ring by dividing the green fluorescence in the center by the non-specific green

fluorescence of the local background, i.e. the region surrounding the center spot expanding out toward but not including the ring, and plotted as a function of peptide concentration (Figure 5). This value is expected to increase with a greater number of indicator particles in the drop center.

Fluorescence signal measured at the drop's edge (Figure 4) measures disruption of indicator particle flow to the ring due to PLH-mediated cross-linking of the Ni(II)NTA ligands present on the indicator particle and magnetic particle surfaces. This metric is the ratio of green to green+red fluorescence at the drop's edge. As expected, this value decreases with increasing PLH concentration. Since the data were not normalized for differences in fluorescence quantum yield between the indicator and control particles, the PLD negative control values are fairly constant at approximately 0.33 rather than 0.5. Based on this metric the limit of detection is approximately 200-300nM.

Fluorescence signal in the drop's center (Figure 5) indicates the number of indicator particles bound to magnetic particles relative to the number of indicator particles that have non-specifically settled between the ring and the drop center. An underlying assumption in this calculation is that all green fluorescence co-located with magnetic particles is due to PLH-mediated cross-linking between indicator particles and magnetic iron oxide particles. Consistent with the assay image appearance, center signal increases with increased PLH concentration but remains constant at approximately zero in the corresponding negative (PLD) assay. This center-based metric also indicates an assay limit of detection of 200-300nM.
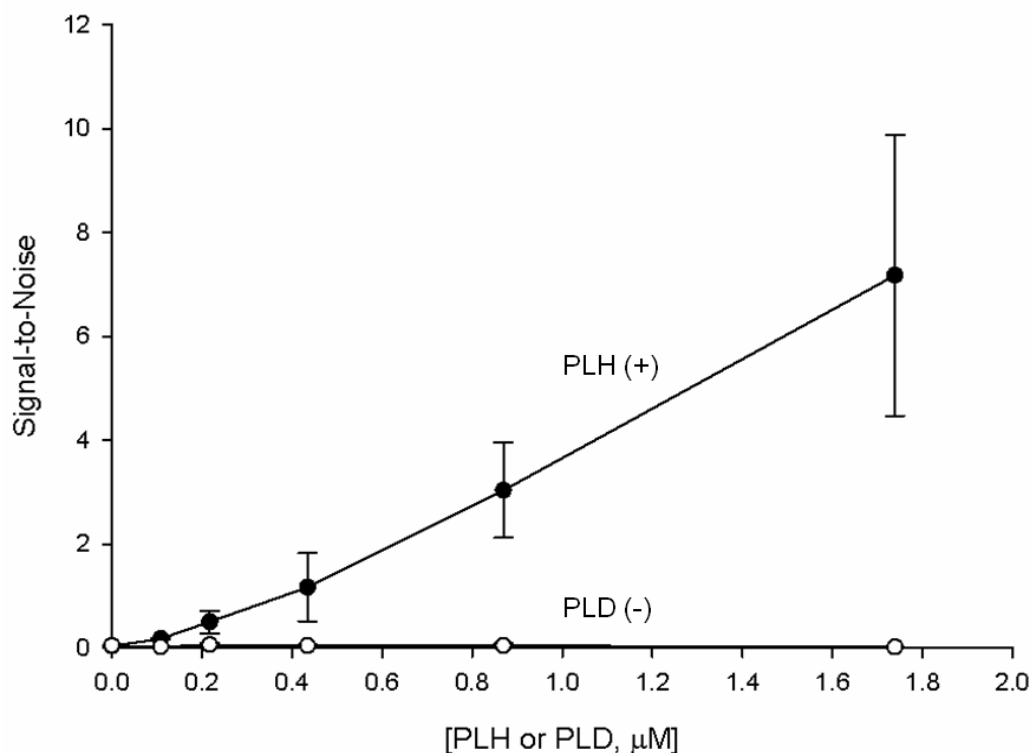
Figure 5. Center-based signal measurement as a function of biomarker and control peptide concentrations. Signal is measured as green fluorescence intensity in the center of the drop and noise is calculated as the green fluorescence intensity difference between the two inner areas of interest. Signal-to-noise ratio is plotted against [PLH] (positive,•) and [PLD] (negative, o), N=3, mean ± 1 s.d.

The two metrics quantify two ways in which the assay color distribution can be perceived and a positive and negative test result discriminated: a change in edge color and a change in the color of the drop's center. The edge-based metric plotted in Figure 4 identifies a positive result by the number of indicator particles relative to control particles in the drop ring and therefore a change in ring color. Conversely, the underlying assumption of the center-based metric (Figure 5) is that positive signal is generated when magnetic particle-indicator particle assemblies are concentrated in the drop center appearing as a green fluorescent spot. Excluding non-specific particle-substrate binding affects, the indicator particle either migrates to the edge (no biomarker) or becomes magnetically trapped in the center (with biomarker). Although the two methods of

measuring assay signal are not strictly independent, PLH concentration-dependent signal generation shown in Figure 4 is corroborated by and consistent with results shown in Figure 5.

The particle-biomarker interface is a critical design feature that affects the particle deposition patterns shown in Figure 2 and Figure 3. The interface employed in this study (Scheme 1b) is Ni(II) nitrilotriacetic acid (NTA) chelation, a common method for isolating and purifying histidine-tagged proteins.[20,21] The Ni(II)NTA ligand is the target recognition element that induces particle aggregation in the presence of pfHRPII (Figure 3). PLH mimics the metal binding characteristics of pfHRPII, a 67kDa protein containing 54 histidine dimer repeats conducive to metal-ion coordination. In this model system, the intrinsic metal reactivity of pfHRPII is the basis for biomarker-mediated particle self-assembly. This aspect has been recently demonstrated by Swartz et al. who showed pfHRPII concentration-dependent aggregation of Ni(II)NTA-functionalized gold and silver nanoparticles induced a shift in surface plasmon resonance.[22] Additionally they showed the same aggregation-inducing effect using PLH and BNTII,[18] another *pf*HRPII biomimic.
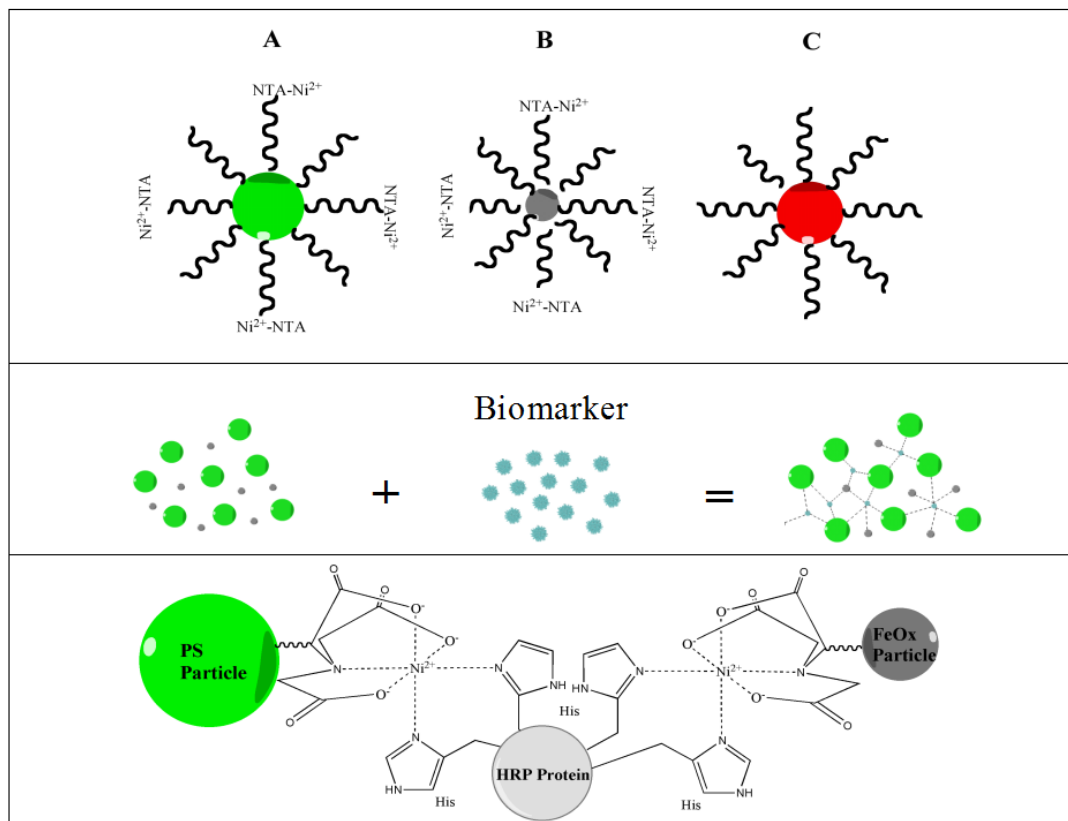
Scheme 1b. **Surface chemistry and particle-particle interactions. Upper panel. The assay consists of three particles: (A) 1μm diameter green fluorescent polystyrene; (B) 250nm diameter dextran-coated iron oxide; (C) 1μm diameter red fluorescent polystyrene. Particles (A) and (B) are surface modified with PEG groups terminated with Ni-NTA. Particle (C) is pegylated. Center panel. Histidine residues in the biomarker cross-link particles (A) and (B). Lower panel. NiNTA coordinates biomarker histidines.**

The surface of the indicator particle was functionalized with Ni(II)NTA following modified procedures originally developed by Nolan et al.[23] A polyethylene glycol (PEG) spacer was incorporated between the particle surface and the NTA ligand to minimize non-specific interactions caused by the hydrophobic particle surface. Both the indicator and magnetic particles were charged with Ni(II). The control particle was surface-modified with methyl-terminated PEG to minimize non-specific interactions. Many different particle-biomarker interfaces could be used in this assay design. For example, antibody/antigen, phage selective binding, avidin/biotin, aptamer/antigen, or metal chelate/histidine coordination could all be developed to target a biomarker of interest. This design flexibility allows the particles to bind to a wide variety of different biomarkers and therefore potentially enables diagnostic utility for a number of diseases.

In this proof-of-concept study, the data presented (Figure 3, Figure 4, and Figure 5) suggest a limit of detection in the 200-300nM range, which is somewhat higher than current rapid diagnostic tests. The World Health Organization's recommended sensitivity of 2000 parasites/µL corresponds to an approximate pfHRPII concentration near 1nM.[24-27] Recent research has determined currently available rapid diagnostic tests can detect pfHRPII concentrations as low as 800pM to 20nM pfHRPII.[28] Assuming that PLH suitably mimics pfHRPII nickel binding behavior, the detection limit of the proposed assay is approximately one order of magnitude above the biologically relevant pfHRPII concentration. We anticipate that with design enhancements the limit of detection can be improved.

In theory, the detection limit of this approach can be improved by six orders of magnitude. If we conservatively assume that all indicator particles (green) in the top left panel of Figure 3 are at the drop center for a biomarker concentration of 1.74µM, we can use this observation and the number of indicator particles present in the drop (10^6) to estimate how many biomarkers would be theoretically required to produce this image. At the theoretical limit of detection, each indicator particle is brought from the edge into the drop center by one and only

one biomarker. If this were achieved experimentally then the panel in Figure 3 (top left) would correspond to 1.74pM, well within the acceptable limits for malaria detection. Controlling the number of binding sites per particle is one potential strategy to approach the theoretical limit of detection.

Drop size is another critical design consideration affecting multiple aspects of assay performance. The effect of drop size on pattern formation in evaporating drops has been previously observed. For example, Deegan et al. empirically demonstrated that ring width scales linearly with drop radius for a given initial particle concentration.[1] Therefore, a larger drop volume generates a wider ring that facilitates visual interpretation of the assay. In the format described here, maximum drop volume is constrained by both evaporation time, which affects time-to-result, and the magnetic field strength, which decreases with increasing distance from the drop's center. The 3μL drops fully evaporated within approximately 20min (ambient conditions: approximately 25°C, 30% relative humidity). This evaporation time represents a time-to-result that is consistent with that achieved with commercially available tests used to diagnose malaria in low resource environments.[29] Drop volumes larger than 3μL may require an evaporation time that is less desirable compared to currently available diagnostic technologies (Supporting Information).

As drop volume increases, a greater magnetic field is required to pull the iron oxide particles to the drop's center. Iron oxide particles change position in the drying drop due to a time-dependent net force, the dominant components of which include the outward force caused by evaporation-induced radial flow and the inward-directed magnetic force. In order to separate particle assemblies from control particles at the drop perimeter, the magnetic force must sufficiently exceed the force caused by evaporation-induced radial flow. The magnitude of the magnetic force experienced by the iron oxide particles is a function of both the particles' magnetic susceptibility and the magnetic field strength. The iron oxide particles used in this

36

study have a magnetic susceptibility of 43emu/g of particles (H-field = 1,000 Oe). The small

spherical magnet employed in this preliminary design generated a field strength of 17mT at the

drop perimeter when the poles were aligned orthogonally to the substrate. Under the influence of

this magnetic field, iron oxide particles near the contact line migrate toward the drop's center

with an average velocity of 80μm/s within ten seconds after the drop is deposited over the

spherical magnet. All iron oxide particles are pulled to the drop's center within 30 seconds of

applying the magnet. With no magnet present, iron oxide particles exhibit almost no radial flow

within the first ten seconds of drop evaporation. Outward radial flow of iron oxide particles

increases as the drying process progresses reaching an average radial velocity of 6μm/s at 6.5

minutes into evaporation. The inward magnetic-driven velocity occurs immediately upon drop

deposition and at a rate that is at least an order of magnitude greater than the outward radial flow

that occurs later in the evaporation process without the magnet present. The maximum distance

iron oxide particles can be from the drop's center and still experience sufficient magnetic force to

migrate to the drop's center is approximately 5.5mm, which corresponds to a drop volume of

40μL. These data suggest that the drop size used in this study was well within the size required

for the magnet to effectively attract magnetic particle assemblies, but that larger drop volumes

could also be used given a sufficiently long evaporation time.

Additional assay design features expected to impact assay performance include a larger

particle radius and enhanced image analysis. For a fixed number of biomarkers, a larger particle

would be expected to improve the limit of detection by producing a greater change in visual

appearance. Employing automatic pattern recognition and image processing techniques, such as

those described by Kim et al.,[30] may further improve assay performance.

Optimizing the number of Ni(II)NTA ligands per particle, drop size, and particle radius

will be particularly important for developing a version of this assay that has an improved limit of

detection and uses colorimetric rather than fluorescent particles to enable simple visual interpretation.

Conclusions

This work demonstrates a prototype diagnostic assay based on the mechanism that causes a ring to form in an evaporating coffee drop. In the presence of a biomarker, a positive result produces a ring and center color pattern in an evaporated drop that is easily distinguished from a negative result. The difference in visual appearance is caused by biomarker-mediated disruption of particle migration to the edge producing a red ring and a green center signal, while a negative result produces a yellow ring with no center signal. This method is potentially well-suited for low-resource applications that require a simple-to-use, low cost method for pathogen detection.

Acknowledgements

Supporting Information

Particle count requirement for ring visualization

The proposed assay must contain enough fluorescent particles so that a ring can be visually detectable when the particles are concentrated at the edge of the drop. To determine the minimum number of particles required, 0.97μm diameter carboxylated polystyrene particles (Bang's Labs) were serially diluted in deionized water (10^7, 10^6, 10^5, 10^4, and 10^3 per μL), deposited in 3μL drops in triplicate on a plain glass slide, allowed to evaporate, and imaged using a Nikon TE2000U inverted fluorescence microscope. The process of perceiving a ring shape within an image incorporates not only objective physical aspects of the imaged object, but also subjective variables such as visual acuity and psychology. The subjective components are beyond the scope of this work.

We determined the number of 1μm fluorescent polystyrene particles required to detect a ring in a 3μL drop to be in the range of 10^5 to 10^7 per μL (data not shown). A ring can be detected with as few as 100 – 1,000 particles per μL, but the ring structure is not wide enough to be easily detected on a consistent basis. The lower limit is dictated both by the human eye's ability to resolve a thin ring structure and the minimum particle volume fraction required to pin the contact line. The upper limit is bounded by the fact that a certain percentage of particles in an evaporating drop will settle before reaching the contact line. As the number of particles increases, a greater absolute number of particles settle in the center making it more difficult to resolve a ring at the edge. In other words, more non-specifically settled particles obscures the distinction between a clear ring and a film of particles. Based on this study, we determined that the concentration of an indicator particle (red or green) in the final reaction volume must fall within 10^5 to 10^7 per μL in order to generate an easily detectable ring. Assay design used in

variable analysis / optimization experiments were performed using polystyrene concentrations within this range.

Areas of interest used in fluorescence intensity measurements
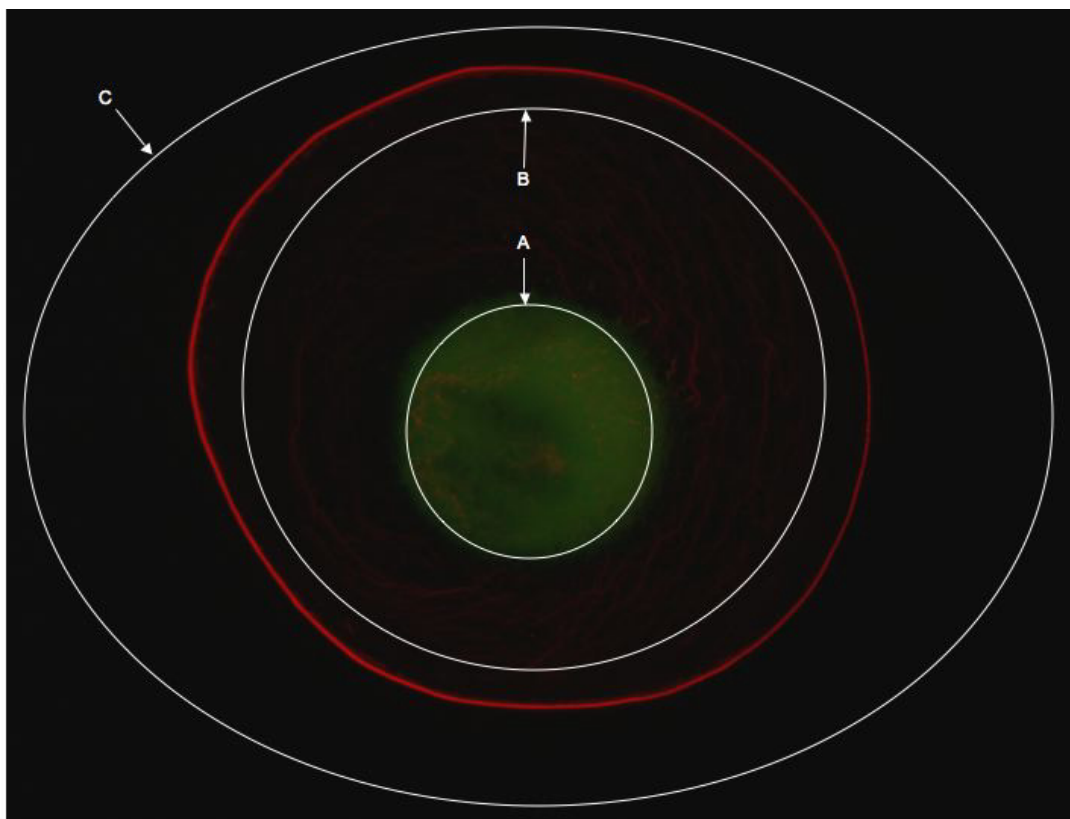
Figure S6. Areas of interest for intensity measurements. (A) area of interest is placed around the magnetic particles that accumulate in the drop center above the magnetic field lines. In a positive sample, indicator (green) particles co-locate with magnetic particles – the fluorescence intensity of which represents signal in the system. (B) secondary inner area of interest captures both signal in the center and particles that have non-specifically and randomly settled throughout the inner region. (C) outer area of interest measures the total fluorescence intensity of the drop. (B) – (A) represents noise. (A) represents signal. (C) – (B) represents a surrogate marker for both signal and noise since particles not transported to the edge either non-specifically settle in the inner region as noise or specifically trans-locate to the center as signal.

Determination of particle concentrations

The ratio of PS-PEG-Ni(II)NTA : Iron oxide-Ni(II)NTA : PLH is expected to be a critical relationship due to competitive binding characteristics and the total number of Ni(II)NTA sites relative to the number of PLH molecules. Using a 384-well plate, a matrix of varying [PS-PEG-Ni(II)NTA] and [iron oxide-Ni(II)NTA] was generated. Iron oxide-Ni(II)NTA initial concentrations (per μL) evaluated were: $4x10^7$, $3x10^7$, $2x10^7$, $1x10^7$. PS-PEG-Ni(II)NTA initial concentrations (per μL) evaluated were: $1.3x10^7$, $1x10^7$, $7x10^6$, $3.86x10^6$. The particles were pre-mixed in each well and then 435nM PLH was added and incubated for thirty minutes. Three microliter drops were deposited on a plain glass slide in triplicate on the magnet-slide apparatus. Fluorescence intensities were measured for each image and signal metrics were calculated. The three calculations were averaged for each data point and the mean plotted (Figure S2).
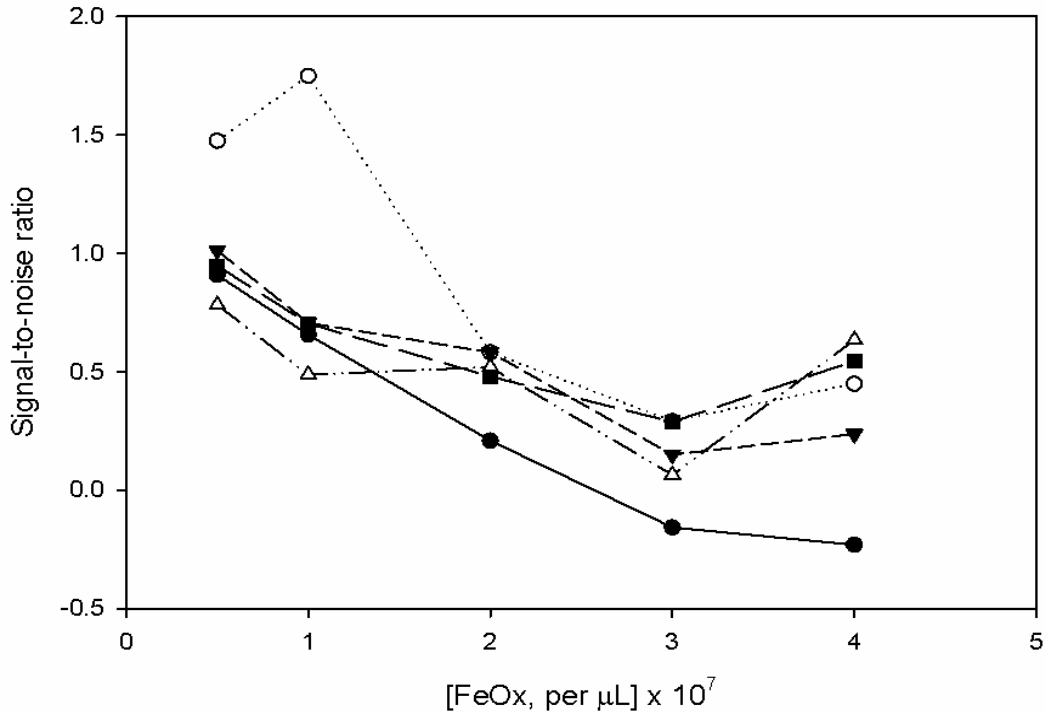
Figure S7. **Signal-to-noise ratio generated in a two-particle assay with varying concentrations of polystyrene and iron oxide particles (n=3). PLH concentration was held constant at 435nM.**

Optimal particle concentrations of PS-PEG-NiNTA to iron oxide-NiNTA were determined by varying each and calculating and comparing signal at each combination. PLH concentration was held constant at 435nM. Peak signal was found to coincide with polystyrene and iron oxide concentrations of 3.86×10^6 and 1×10^7 per μL, respectively (Figure S2).

Holding other variables constant, increasing particle concentrations reduces assay sensitivity. If for a given PLH concentration the concentration of indicator particles is optimized, then all indicator particles will be shifted to the center and none will transport to the drop edge. If the number of indicator particles increases at the same PLH concentration, there will not be

enough target available to cross-link the extra particles to iron oxide particles and they will migrate to the edge adding more green to the ring. If the number of indicator particles is decreased, then signal will not be maximized because there will be PLH molecules present not being used to cross-link particles. A multivariate regression model was performed using [PS-PEG-NiNTA and [iron oxide-NiNTA] as independent variables and center signal as the dependent variable. The PS-PEG-NiNTA concentration was found to have a statistically significant positive effect on signal (p-value < .001; t-statistic 3.55) within the concentration ranges studied. The iron oxide particle concentration did not have a statistically significant impact on signal probably because the number of nickel binding sites on iron oxide particles exceeded those required at a [PLH] = 435nM. A lower limit of detection is expected using particle concentrations determined by optimizing signal at a lower PLH concentration.

Drop evaporation time

To determine the relationship between drop volume and evaporation time, 1μm diameter carboxylated polystyrene beads were suspended in deionized water at 1×10^{6} particles per μL. Drops of varying volumes were deposited on a plain, clean glass slide in triplicate and the time to complete evaporation was measured and recorded. The mean evaporation times are plotted below. Error bars represent +/- one standard deviation. The experiment was conducted at room temperature with a relative humidity of approximately 60%.
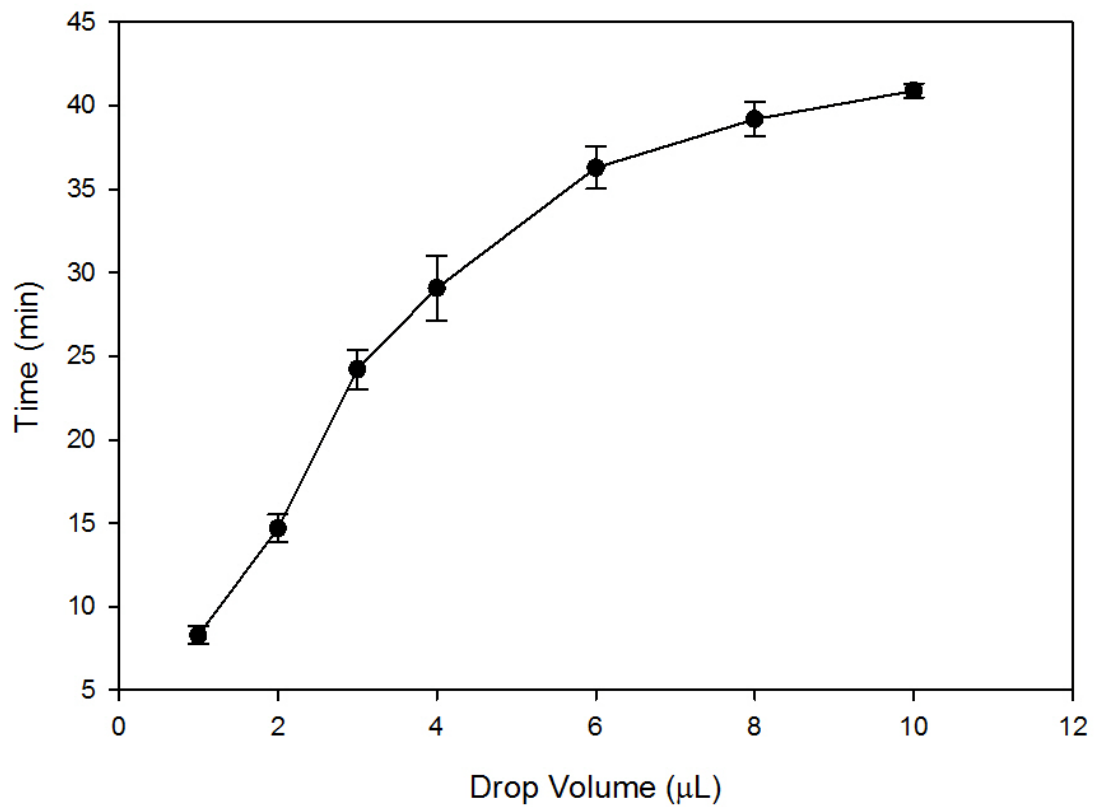
Figure S8 Evaporation time as a function of drop volume.

References

(1)   Deegan, R. D.: Pattern formation in drying drops. *Physical Review E* **2000**, *61*, 475-485.

(2)   Deegan, R. D.; Bakajin, O.; Dupont, T. F.; Huber, G.; Nagel, S. R.; Witten, T. A.: Contact line deposits in an evaporating drop. *Physical Review E* **2000**, *62*, 756-765.

(3)   Deegan, R. D.; Bakajin, O.; Dupont, T. F.; Huber, G.; Nagel, S. R.; Witten, T. A.: Capillary flow as the cause of ring stains from dried liquid drops. *Nature* **1997**, *389*, 827-829.

(4)   Sangani, A. S.; Lu, C. H.; Su, K. H.; Schwarz, J. A.: Capillary force on particles near a drop edge resting on a substrate and a criterion for contact line pinning. *Physical Review E* **2009**, *80*.

(5)   Hu, H.; Larson, R. G.: Analysis of the effects of Marangoni stresses on the microflow in an evaporating sessile droplet. *Langmuir* **2005**, *21*, 3972-3980.

(6)   Hu, H.; Larson, R. G.: Evaporation of a sessile droplet on a substrate. *Journal of Physical Chemistry B* **2002**, *106*, 1334-1344.

(7)   Hu, H.; Larson, R. G.: Analysis of the microfluid flow in an evaporating sessile droplet. *Langmuir* **2005**, *21*, 3963-3971.

(8)   Harris, M. T.; Widjaja, E.: Particle deposition study during sessile drop evaporation. *Aiche Journal* **2008**, *54*, 2250-2260.

(9)   Kajiya, T.; Kaneko, D.; Doi, M.: Dynamical Visualization of "Coffee Stain Phenomenon" in Droplets of Polymer Solution via Fluorescent Microscopy. *Langmuir* **2008**, *24*, 12369-12374.

(10)   Yunker, P. J.; Still, T.; Lohr, M. A.; Yodh, A. G.: Suppression of the coffee-ring effect by shape-dependent capillary interactions. *Nature* **2011**, *476*, 308-311.

(11)   Bhardwaj, R.; Fang, X. H.; Somasundaran, P.; Attinger, D.: Self-Assembly of Colloidal Particles from Evaporating Droplets: Role of DLVO Interactions and Proposition of a Phase Diagram. *Langmuir* **2010**, *26*, 7833-7842.

(12)   Wong, T. S.; Chen, T. H.; Shen, X. Y.; Ho, C. M.: Nanochromatography Driven by the Coffee Ring Effect. *Analytical Chemistry* **2011**, *83*, 1871-1873.

(13)   Tarasevich, Y. Y.; Pravoslavnova, D. M.: Segregation in desiccated sessile drops of biological fluids. *European Physical Journal E* **2007**, *22*, 311-314.

(14)   Tarasevich, Y. Y.; Pravoslavnova, D. M.: Drying of a multicomponent solution drop on a solid substrate: Qualitative analysis. *Technical Physics* **2007**, *52*, 159-163.

(15)   Larson, R. G.; Lopez, M. A.; Lim, D. W.; JLahann, J.: Complex Protein Patterns in Drying Droplets. *MRS Proceedings* **2010**, *1273*.

(16)   Brutin, D.; Sobac, B.; Loquet, B.; Sampol, J.: Pattern formation in drying drops of blood. *Journal of Fluid Mechanics* **2011**, *667*, 85-95.

(17)   Wright, D. W.; Ziegler, J.: Exploring metalloporphyrin binding in histidine-rich protein models. *Abstracts of Papers of the American Chemical Society* **1998**, *216*, U277-U277.

(18)   Ziegler, J.; Chang, R. T.; Wright, D. W.: Multiple-antigenic peptides of histidine-rich protein II of Plasmodium falciparum: Dendrimeric biomineralization templates. *Journal of the American Chemical Society* **1999**, *121*, 2395-2400.

(19)   Marletta, M. A.; Schneider, E. L.: Heme binding to the histidine-rich protein II from Plasmodium falciparum. *Biochemistry* **2005**, *44*, 979-986.

(20)   Terpe, K.: Overview of tag protein fusions: from molecular and biochemical fundamentals to commercial systems. *Applied Microbiology and Biotechnology* **2003**, *60*, 523-533.

(21)   Mori, S.; Takahashi, H. K.; Yamaoka, K.; Okamoto, M.; Nishibori, M.: High affinity binding of serum histidine-rich glycoprotein to nickel-nitrilotriacetic acid: The application to microquantification. *Life Sciences* **2003**, *73*, 93-102.

(22)   Swartz, J. D.; Gulka, C. P.; Haselton, F. R.; Wright, D. W.: Development of a Histidine-Targeted Spectrophotometric Sensor Using Ni(II)NTA Functionalized Au and Ag Nanoparticles. *Langmuir* **2011**, *in press*.

(23)   Lauer, S. A.; Nolan, J. P.: Development and characterization of Ni-NTA-bearing microspheres. *Cytometry* **2002**, *48*, 136-145.

(24)   Minigo, G.; Woodberry, T.; Piera, K. A.; Salwati, E.; Tjitra, E.; Kenangalem, E.; Price, R. N.; Engwerda, C. R.; Anstey, N. M.; Plebanski, M.: Parasite-Dependent Expansion of TNF Receptor II-Positive Regulatory T Cells with Enhanced Suppressive Activity in Adults with Severe Malaria. *Plos Pathogens* **2009**, *5*.

(25)   Dondorp, A. M.; Desakorn, V.; Pongtavornpinyo, W.; Sahassananda, D.; Silamut, K.; Chotivanich, K.; Newton, P. N.; Pitisuttithum, P.; Smithyman, A. M.; White, N. J.; Day, N. P. J.: Estimation of the total parasite biomass in acute falciparum malaria from plasma PfHRP2 (vol 2, art. no. e204, 2005). *Plos Medicine* **2005**, *2*, 1047-1047.

(26)   Rajasekariah, G. H.; Martin, S. K.; Awinda, G.; Waitumbi, J.; Kifude, C.: Unified Parasite Lactate Dehydrogenase and Histidine-Rich Protein ELISA for Quantification of Plasmodium falciparum. *American Journal of Tropical Medicine and Hygiene* **2009**, *80*, 516-522.

(27)   Waitumbi, J. N.; Kifude, C. M.; Rajasekariah, H. G.; Sullivan, D. J.; Stewart, V. A.; Angov, E.; Martin, S. K.; Diggs, C. L.: Enzyme-linked immunosorbent assay for detection of Plasmodium falciparum histidine-rich protein 2 in blood, plasma, and serum. *Clinical and Vaccine Immunology* **2008**, *15*, 1012-1018.

(28)   Reyburn, H.; Mbakilwa, H.; Mwangi, R.; Mwerinde, O.; Olomi, R.; Drakeley, C.; Whitty, C. J.: Rapid diagnostic tests compared with malaria microscopy for guiding outpatient treatment of febrile illness in Tanzania: randomised trial. *BMJ* **2007**, *334*, 403.

(29)   WHO: Results of WHO product testing of malaria RDTs: Round 3 (2010-2011). *Malaria Rapid Diagnostic Test Performance* **2011**.

(30)   Kim, N.; Li, Z.; Hurth, C.; Zenhousern, F.; Chang, S.-F.; Attinger, D.: Identification of fluid and substrate chemistry based on automatic pattern recognition of stains. *Analytical Methods* **2011**, *in press*.

CHAPTER IV

CROSS-SECTIONAL TRACKING OF PARTICLE MOTION IN EVAPORATING DROPS:
FLOW FIELDS AND INTERFACIAL ACCUMULATION

Joshua R. Trantum
Zachary E. Eagleton
Chetan A. Patil
Jason M. Tucker-Schwartz
Mark L. Baglia
Melissa C. Skala
Frederick R. Haselton

Department of Biomedical Engineering
Vanderbilt University
Nashville, Tennessee

Abstract

The lack of an effective technique for three-dimensional flow visualization has limited the experimental exploration of the "coffee ring effect" to the two dimensional, top-down viewpoint. In this report, high-speed, cross-sectional imaging of the flow fields was obtained by using optical coherence tomography to track particle motion in an evaporating colloidal water drop. This approach enables z-dimensional mapping of primary and secondary flow fields and changes in these fields over time. These sectional images show that 1μm diameter polystyrene particles have a highly non-uniform vertical distribution with particles accumulating at both the air-water interface and water-glass interface during drop evaporation. Particle density and relative humidity are shown to influence interfacial entrapment, which suggests that both sedimentation rate and evaporation rate affect the dynamic changes in the cross-sectional distribution of particles. Furthermore, entrapment at the air-water interface delays the time at which particles reach the ring structure. These results suggest that the organization of the ring structure can be controlled based on the ratio of different density particles in a colloidal solution.

Introduction

The coffee ring effect is a dynamic process in which colloidal particles are transported to the drop edge by thermocapillary mass convection and deposited on the substrate. The physical basis of this phenomenon, originally described by Deegan, is that colloidal particles deposit at the contact line, i.e. air-water-substrate interface, early in the evaporation process due to surface tension interactions and topological heterogeneities.[1-3] These deposited particles pin the contact line and prevent it from receding during evaporation. The evaporative flux is greatest at the contact line due to the proximal location of ambient, unsaturated gas, and internal flow is established to replenish evaporated solvent at the edge. This axisymmetric and outwardly directed current transports particles to the edge of the drop where they are deposited resulting in the characteristic ring pattern. More than just a curiosity, these non-uniform deposits have profound effects in a wide range of industrial applications including DNA microarray manufacturing, inkjet printing, and microelectronics.[4-6]

Previous reports of mitigating, reversing, or enhancing this phenomenon span a wide range of strategies including solution conditions, particle shape, and secondary flow fields. For example, Bhardwaj et al. have shown how pH-induced Derjaguin-Landau-Verwey-Overbeek (DLVO) interactions can shift particle deposition from the edge to the center of the drop,[8] Yunker et al. have shown that particle aspect ratio is correlated to the degree of pattern uniformity,[9] and Hu et al. have shown that Marangoni stresses, which result from surface tension gradients, can induce internal eddies that oppose the coffee-ring effect.[10,11] Several groups have reported the effects of surfactants on Marangoni-Bénard flow in evaporating colloidal drops.[12-14] Ristenpart et al. have shown that a difference in thermal conductivities between solution and substrate can reverse the Marangoni circulation.[15]

Understanding the conditions that inhibit or promote deposition patterns is also of great interest in applications in which the phenomenon is manipulated for a desired effect. For example, Ho et al. recently demonstrated that the inherent size exclusion geometry present near

the contact line can be used to chromatographically separate particles.[16] Other groups have reported that residues from dried drops of biological fluids can potentially be used as an indication of disease.[17-19] A diagnostic assay design in which the coffee ring effect organizes surface functionalized particles in unique colorimetric patterns depending on the presence or absence of target antigen has also been recently reported.[20] In fact, observations made in this latter application motivated this study.

Tracking cross-sectional particle motion during drop evaporation would provide new information which is important for mapping fluid dynamics and elucidating the mechanism by which system variables affect deposition patterns. Previous studies have most commonly employed video and fluorescence microscopy to generate a top-down, two-dimensional view of particle flow during drop evaporation.[10,13,21,22] This method has proven useful for imaging the primary radial fluid fields associated with the coffee ring effect. However, as previous studies on Marangoni-Bénard flows have shown, evaporating drops can contain eddies and secondary flows under certain conditions that are difficult to resolve with two-dimensional microscopy-based techniques.[11,23] Hu et al. demonstrated cross-sectional reconstruction of 3D flows based on side-directed, out-of-focus microscopy.[10] While this method enables some cross-sectional visualization of the coffee ring effect, the limited spatial and temporal resolutions of this technique limit precise mapping of 3D flow patterns. Bodiguel et al. used confocal microscopy to cross-sectionally image tracer particles in an evaporating drop.[24,25] Despite using fast scanning techniques, the imaged slice in this study was limited to a fixed distance from the substrate in order to generate a temporal resolution adequate for particle tracking. Confocal microscopy has a shallow depth of field thereby spatially limiting the focal plane. To our knowledge, confocal microscopy is currently not capable of imaging an entire cross-section of a colloidal drop, having a maximum height of 300μm, within a timeframe that enables particle tracking during drop evaporation.

This study explores the use of optical coherence tomography (OCT) to investigate cross-sectional flow patterns in evaporating water drops. OCT is a real time imaging modality that generates cross-sectional images of sample backscattering with micron-scale axial and transverse resolution and millisecond temporal resolution.[26] The spatio-temporal resolution of OCT is well-suited for identifying and tracking movement of micron-sized particles. In addition, the depth-of-field of OCT is typically >1mm, approximately two orders of magnitude greater than confocal microscopy and well-matched to the 300μm maximum height of sessile drops of the volumes used in this study (~1μL). This capability enables imaging of the entire drop cross section. Unlike microscopic techniques, OCT provides accurate z-dimension information of 1μm particles, and over time the images can directly resolve z-dimensional features of flow within the sample. OCT has been previously shown to effectively track polystyrene particle motion for other applications.[27-30] For example, Jonas et al. used OCT-based particle tracking velocimetry to image fluid flow created by oscillating cilia.[28] Since flow fields are axisymmetric around the drop center, particle motion captured by a single cross-sectional plane through the drop diameter provides a comprehensive depiction of flow fields in the entire drop. While the data generated from a single plane is inherently two-dimensional, three dimensional motion can be inferred from the radial (axisymmetric) geometry of the drop. It follows that cross-sectional imaging, such as with OCT, provides 3D information about particle motion in an evaporating drop. Thus, OCT appears to be well-suited for measuring particle motion and particle distribution which is necessary for obtaining a better understanding of this seemingly simple phenomenon.

In this report, OCT is used to qualitatively describe the cross-sectional motion of particles in evaporating water drops. The effect of particle density and ambient relative humidity on vertical particle distribution is quantified and shown to influence the organization of the dried ring structure. OCT-based particle tracking velocimetry using a two-frame nearest neighbor approach is also employed to quantitatively describe the motion of different particle types using

52

an approach similar to Jonas et al.[28] Video sequences of OCT images recorded at 0.2s per frame show complete particle motion under several experimental conditions.

Experimental Methods

Material Preparation and Characterization

Four different particle types were used in the study, all 1μm-diameter: carboxylated polystyrene (Bangs Laboratories, Inc.), aminated polystyrene (Invitrogen), carboxylated melamine formaldehyde (Sigma Aldrich), and silica (Kisker Biotech). Physical properties of the particles are summarized in Table 1. All particles were fluorescent (polystyrene – red, melamine formaldehyde – green, and silica – blue) to enable imaging of dried deposition patterns with fluorescence microscopy. Particle solutions were prepared by diluting stock particles in distilled, filtered water (MiliQ) at pH 4.1. Solutions were centrifugally washed 8x and particles were resuspended at a volume fraction, φ, of 0.005% (or 10^5 particles per μL) in MiliQ water at pH = 4.1. Particle surface charge was determined by measuring the zeta potential (Malvern Zetasizer) of particles suspended in a 10mM NaCl, pH 4.1 solution. Plain glass slides (Fisher Scientific) were used as the substrate in all experiments and were cleaned by washing with 100% ethanol followed by distilled water and air-dried. All particle solutions were thoroughly sonicated prior to drop deposition.

Optical Coherence Tomography

A drop (1μL) was deposited on a clean glass slide and cross-sectional images were recorded using a commercial OCT system (Bioptigen, Inc.) with a laser source (860nm center wavelength, 51nm full width half max bandwidth) fixed at an angle of 9° from normal. The drop was manually positioned so the OCT laser was aligned with the diameter of the drop. This was done while imaging with OCT, and the diameter was identified as the position at which drop height was a maximum. Total evaporation time, t_f, was measured for each sample, and OCT

frames were sequenced according to percent of total evaporation time. This approach allowed OCT frames from different samples to be compared on the basis of normalized evaporation time.

Particle Type	Surface	Mean Diameter (µm)	Density (g/cm^3)	Stokes Sedimentation Rate (µm/s)	Zeta Potential, ζ (mV)
Polystyrene	-COOH	0.97	1.04	0.02	-23
Polystyrene	-NH$_2$	1.00	1.04	0.02	39
Melamine Formaldehyde	-COOH	1.00	1.50	0.27	-16
Silica	Plain	1.00	2.00	0.54	-13

Table 1. Physical properties of the four particle types.

This experimental set-up resulted in a transverse digital sampling resolution of 3µm/pixel and an axial digital sampling resolution of 1.69µm/pixel. The optical resolution of the system is approximately 8µm in the lateral direction, defined as the full-width half max of the point-spread function of the system, and 6.4µm in the axial direction. In OCT, ballistic photons from a broadband laser source are split between the imaging sample and a reference mirror at a known distance from the source. The light reflected from the reference mirror recombines with backscattered light from the sample and generates an interference pattern. The axial depth of a scattering object in the sample is calculated from the oscillation frequencies in this interference pattern. Axial resolution is determined by the wavelength and coherence length of the source light. All axial data at a particular position (A-scan) is acquired during one integration cycle of the charge-coupled device (CCD), and transverse images are obtained by raster scanning the laser across the sample with motorized mirrors.

Interference patterns from the reference and sample arm were captured with a 2048 pixel CCD with 10kHz integration time, and approximately 700μW on the sample. Interference data was then processed by: (1) resampling the data to be linear with respect to wavenumber, (2) correcting dispersion using well-established processing algorithms, (3) subtracting the background to remove the source spectrum, and (4) generating OCT image data as a function of depth via Fourier transform.[31,32]

Due to memory limitations of the instrument software, only 200 B-scans could be recorded in a given sequence, which equals 40s of recorded video at a 0.2s time step per frame. A barrier was placed around the experimental set-up to prevent ambient air currents from reaching the evaporating drop. Ambient temperature and relative humidity were recorded during evaporation. Following OCT imaging, the dried deposition pattern was imaged under phase contrast and fluorescence microscopy at 2x magnification. All drop evaporation experiments were repeated in triplicate, and blank drops (no particles) were also imaged with OCT to quantify background noise for image processing.

Image Processing and Analysis

OCT files were converted to tagged image file (TIFF) format in Matlab. ImageJ software was used to edit video sequences and image stacks. OCT images were taken of plain water drops in preliminary experiments to determine the threshold intensity in post-image processing that removed 95% of the background noise. OCT images from all subsequent experiments were thresholded at this predetermined level to ensure that remaining signal in the images is attributed to particles. Vertical particle distributions in the OCT images were quantified using a Matlab program that defined a rectangular area of interest encompassing the drop cross-section and equal to 20% of the drop diameter centered at the drop midpoint. This area was subdivided into equally-sized, stacked, rectangular areas-of-interest each with a height of 10 pixels, or 16.9μm, with the top area-of-interest vertically centered on the air-water interface

(see Figure 6 inset). The Matlab program computed average pixel intensity in each of the stacked areas of interest. Data arrays were exported to Excel and interfacial accumulation was calculated as the average pixel intensity in the particular area of interest divided by the summed average pixel intensities for all areas of interest. The analysis was repeated for 1,200 OCT frames for each data set.

OCT-based particle tracking velocimetry was performed following a method similar to that used by Jonas et al.[28] Each OCT frame of a 200-frame sequence, 0.2s time step per frame, was thresholded as previously described and pixel intensities were converted to binary values. The time step was then increased to 2s per frame by retaining every tenth frame. Using Image-Pro Plus software (MediaCybernetics, version 7), particles were identified as any group of at least five connected pixels having an intensity value equal to one. Particles were then tracked over a sequence of frames using a nearest neighbor approach based on the center pixel of each object. Particles moving into or out of the imaged slice (i.e. B scan) were removed from the data set. Also, all particles were spatially binned, and those present at the air-water interface and water-glass interface were removed from the data set. Cartesian coordinate values for each particle per frame were exported to Excel, and average velocities, v_i, and angle of motion, θ_i relative to the substrate were calculated for each particle, p_i, as:[28]

$$v_i = \frac{\sqrt{(A\Delta x)^2 + (B\Delta y)^2}}{\Delta t} \qquad\qquad \theta_i = \tan^{-1}\left(\frac{v_{iy}}{v_{ix}}\right)$$

Where A and B are scaling factors equal to 3μm/pixel and 1.69μm/pixel, respectively.

This simple method of particle tracking is most applicable due to the low volume fraction of particles used in the study. As the OCT videos (Supporting Information) show, the relatively low concentration of particles enables discrete particle identification. Moreover, this method has been previously and successfully employed at similar particle velocities.[28] After performing the above analysis at timesteps of both 0.2s and 2s, it was determined that the latter timestep was sufficient for tracking particles.

Results and Discussion

Figure 1a shows the radial fluid motion due to the coffee ring effect from a top-down view, characteristic of 2-D microscopy. Outwardly directed and axisymmetric flow fields are easily observed from this vantage point and result in the characteristic dried ring pattern shown in Figure 1b. With this technique it is difficult to resolve three dimensional flow fields. An OCT scan through the diameter of the drop, shown in Figure 1c, enables cross-sectional mapping of these flow fields, which are often times more complex than what is represented by two-dimensional imaging methods.

A single OCT frame taken through the diameter of a 1μL drop, containing 10^5 carboxylated polystyrene particles on a glass slide, shows the position of individual particles. In these images particles appear as white spots on a black background and, in this case, are distributed within the cross-section of the drop with particles at the interfaces outlining the drop's shape (Figure 2a). Some particles appear smaller than others, despite being monodisperse, because they are not all aligned at the center of the imaged plane (B-scan). Particles slightly off center of the B-scan will appear smaller than those at the center of the B-scan. For this image at the instant during evaporation (time point) corresponding to $t=0.33t_f$ where t_f is the total evaporation time, particles are fairly diffuse with a small fraction collected at the air-water interface and the glass substrate. A single OCT cross-sectional scan is acquired in 0.1s, so the particles, which travel at velocities on the order of μm/s or less,[1] appear stationary. The bottom of the drop appears slightly curved due to refraction of the incident OCT laser by the curved drop surface as well as the difference between actual distance and optical path length caused by difference refractive indices of air and water. This artifact decreases as the drop flattens during evaporation and is discussed in greater detail later.
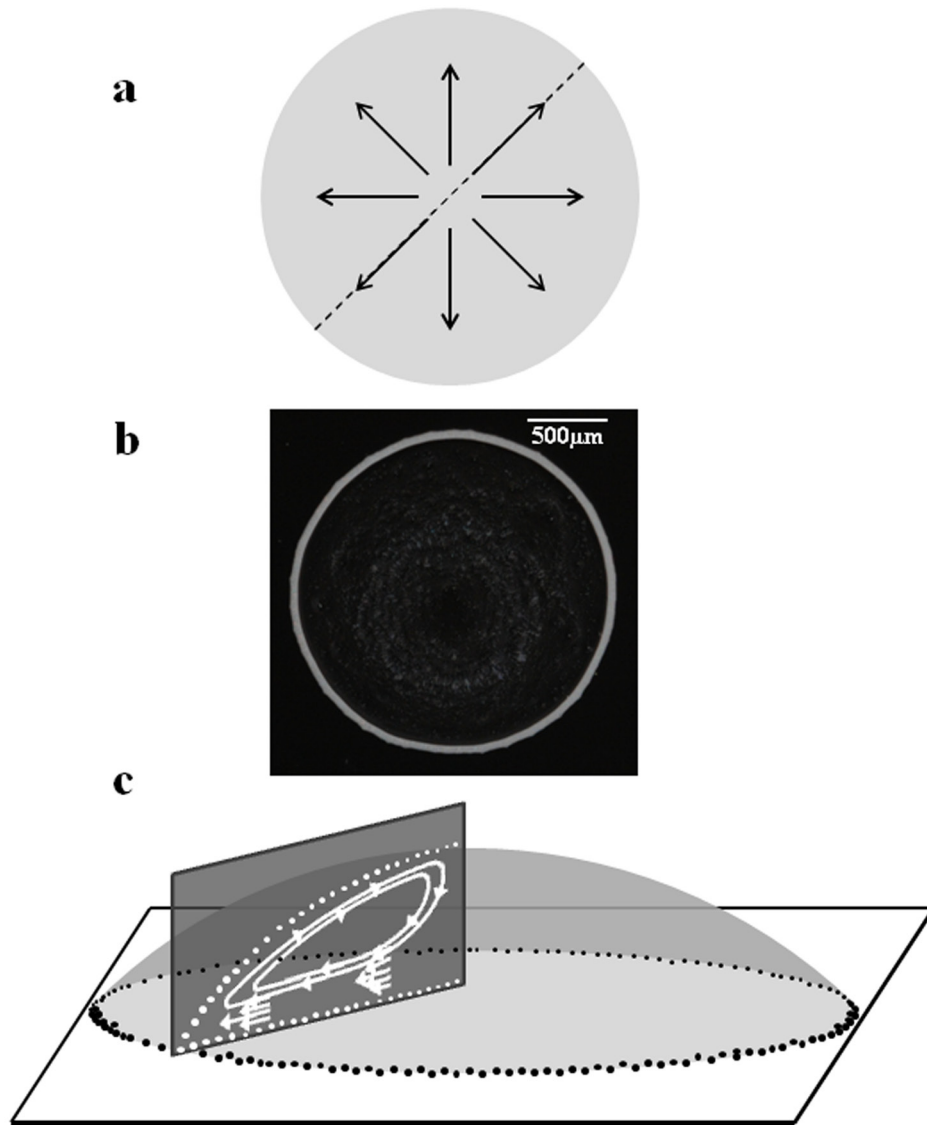
Figure 1. **(a) Particle flow fields in an evaporating drop imaged with top-down microscopy are dominated by radial flow; (b) top-down phase contrast micrograph of a characteristic deposition pattern produced by the coffee ring effect; and, (c) a simplified schematic with no angular offset showing one half of a cross-sectional slice generated by OCT that reveals three-dimensional detail of flow fields.**

The left panel in Figure 2b is a time-lapse composite image representing 20s before and after the same evaporation time point shown in Figure 2a. The image is generated by overlaying a stack of sequential OCT frames taken at 0.1s intervals. A track represents the distance a single particle traveled over 20s, and the length and direction of the track indicates particle velocity. Track lengths, on average, increase with time and radial position toward the contact line. These findings are consistent with previously reported experimental findings and models of the coffee ring effect which show that capillary-induced velocity increases with evaporation time and increasing distance from the drop center.[1,2,7,23,33-35] Radial velocity increases with evaporation time because the fluid required to replenish evaporated solution at the edge must travel through a decreasing volume as the drop height diminishes. Moreover, radial velocity increases with greater distance from the drop center due to the non-uniform evaporative flux that increases along the drop surface with greater distance from the drop center.[35]
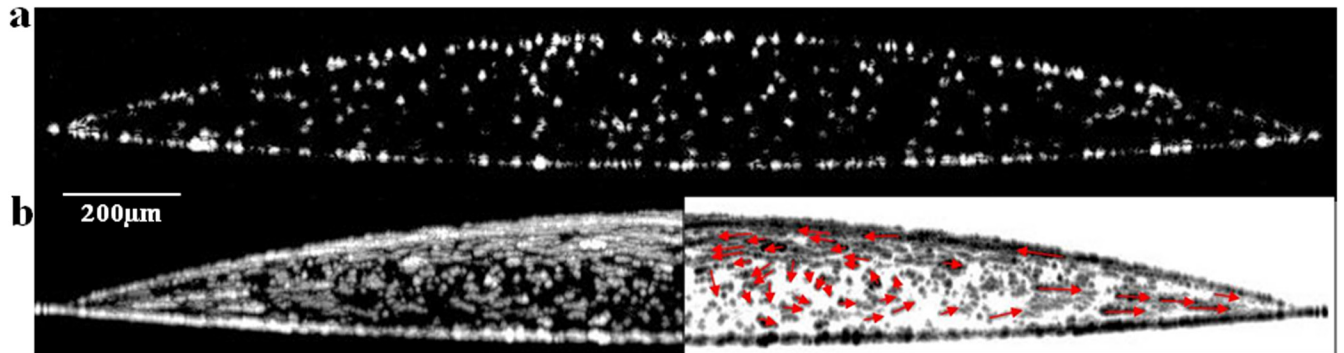
Figure 2. (a) A single OCT frame along the diameter of a 1µL sessile water drop containing 1µm diameter carboxylated polystyrene particles (10^5 per µL) at t=0.33t_f, where t_f is total evaporation time. Individual particles are seen as white dots. (b) Time-lapse composite of 200 consecutive OCT images of a 1µL sessile water drop containing 1µm diameter carboxylated polystyrene particles (10^5 per µL) spanning 20s of drop evaporation beginning at t=0.33t_f. Each white track shows the trajectory of a single particle. The right panel is a mirror image of the left panel but with inverted contrast and red vector lines showing particle trajectories.

59

The right panel in Figure 2b is the same as the left panel but with reverse contrast and superimposed vector lines (red arrows) indicating particle direction. This vector plot reveals flow fields that are more complex than what would typically be observed in top-down video microscopy. A video has been provided in Supporting Information that compares a cross-sectional sequence of OCT images to a top-down video taken with phase contrast microscopy. The dynamic particle motion is even more apparent in the video than in the time-lapse composite images. As these videos illustrate, particles near the drop's edge are deposited at the contact line. Particles at the drop surface remain entrapped at the interface and some are observed traveling back toward the drop center. Additionally, the time-lapse composite image in Figure 2 shows a slight circular eddy in the bulk fluid rotating counterclockwise. These observations suggest the presence of Marangoni flow, which is caused by a surface tension gradient at the air-water interface. According to theory, an interfacial region with high surface tension exerts a pulling force on neighboring regions of lower surface tension having the effect of inducing flow across the gradient. In the case of an evaporating drop, the lowest surface tension occurs at the contact line. Previous investigations have shown a non-uniform surface tension gradient arises from a non-uniform temperature gradient.[11] Early in evaporation, the greatest surface temperature occurs at the contact line due to the close proximity of the substrate, while the lowest surface temperature occurs at the drop center due to the greater conduction path to the substrate. Surface tension at the air-water interface is inversely proportional to temperature. This causes a Marangoni flow early in evaporation along the surface of the drop directed toward the drop center. At later time points the evaporation rate increases near the contact line and the fluid height at the drop center (conduction path to the substrate) decreases sufficiently to eliminate the surface temperature gradient which stops the Marangoni flow. Hu et al numerically demonstrate that the temperature gradient is at or near zero when the contact angle is < 14°.[11] In Figure 2b, the contact angle is approximately 17°, sufficiently high enough, at least theoretically,

to generate Marangoni flow. These results are therefore consistent with Hu et al.'s prediction.[10,11]

Weak Marangoni flow has been shown to occur in colloidal water drops.[1] However, there are conflicting reports on this issue with some groups indicating little-to-no Marangoni flow in colloidal water drops due to the susceptibility of aqueous interfaces to surface contaminants like surfactants that can offset surface tension gradients.[10,36] Moreover, the precise effect of surfactants on Marangoni flow in water drops is unclear. Previous reports have shown that surfactants can both induce and inhibit Marangoni flow depending on the conditions.[14,36] Great care was taken in this study to minimize residual surfactants (Tween 20) from stock particle solutions by centrifugally washing particle solutions eight times with deionized, distilled water. Nonetheless, it is possible the flow fields seen in Figure 2b are due to residual contaminants. Ambient air currents also could have affected surface flow patterns, although a rigid cardboard barrier surrounded the sample stage during all experiments to minimize air currents. All experiments were repeated in triplicate, and this weak Marangoni eddy was only observed in one trial. This lack of repeatability is consistent with these previous studies indicating that the presence of Marangoni flow in water drops is uncommon and weak at best. The most likely explanation is that the secondary flow fields observed in Figure 2b are the result of a weak Marangoni stress.

As others have reported using 2D imaging, particle motion develops slowly and changes over time. In general, particle motion is known to accelerate toward the contact line and average particle speed increases with time. Hu et al have shown theoretically that Marangoni flows occur early in evaporation when the height of the drop at the center is relatively large, and as the drop height falls, Marangoni flows dissipate and particle flow follows a predominantly outward trajectory. The time evolution of these flow fields in cross-section are shown in Figure 3, which shows a time-lapse composite OCT (a) and vector plots (b) at multiple time points during drop evaporation along with the corresponding theoretical flow fields (c). Early in evaporation,

polystyrene particle flow is mostly parallel to the substrate in a region comprising the top half of the drop and extending radially to approximately 0.25R. The distance these parallel trajectories extend down in the z-direction into the bulk drop volume decreases with time. At t = 0.3t_f (second panel in Figure 3), a Marangoni eddy becomes evident. Particles flow toward the drop center at or near the air-water interface and descend toward the substrate near the drop center. The particles then flow toward the contact line, and, upon reaching the eddy, either ascend toward the air-water interface or continue to the contact line. By the last time point shown in Figure 3, the Marangoni eddy has dissipated and the thermocapillary mass convection becomes the dominant flow field transporting polystyrene particles to the contact line.

Particle motion shown in Figure 3a and Figure 3b do not form concentric eddies and therefore do not completely match theoretically predicted Marangoni flow fields (Figure 3c).[7,11] The reason(s) for this are unclear. It is possible that the flow fields seen early in evaporation result from a Marangoni stress are too weak to generate a Marangoni eddy. As previously mentioned, residual surfactants and/or ambient air currents could have affected surface flow patterns, which might be more dominant in cases where only weak Marangoni stresses are present.

Interestingly, Figure 3 appears to show a time dependent accumulation of particles at the two interfaces. It should be noted that the air-water interface appears blurry due to the change in drop height that occurs during the 20s represented in each image. Despite this artifact, it is clear that polystyrene particles accumulate at both interfaces. Previously reported studies on the coffee ring effect do not completely explain this time-dependent non-uniformity. As the drop evaporates, particles accumulate at both the air-water and water-glass interfaces resulting in a non-uniform distribution. At the theoretical sedimentation rate (0.022µm/s), the polystyrene particles are expected to fall approximately 13µm by gravitational settling, excluding the effects of other flows, during the 10min it takes a 1µL drop to dry at 30% relative humidity and 21°C. Therefore, gravitational sedimentation can account at least for some of the accumulation at the

water-glass interface. However, since the density of polystyrene exceeds water, the particles do not experience a net buoyant force that would cause accumulation at the air-water interface.
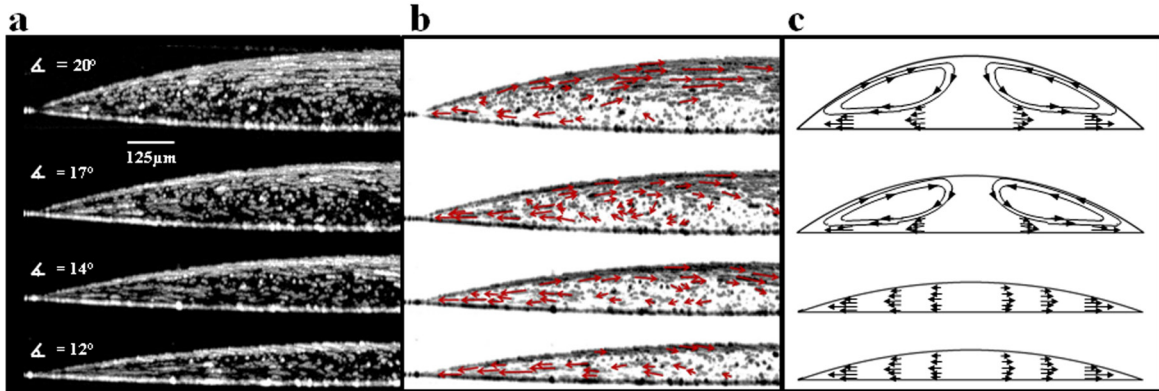
Figure 3. **(a) Time-lapse composite of 200 consecutive OCT images of a 1μL water drop containing 1μm diameter carboxylated polystyrene particles (10[5] per μL) spanning 20s of drop evaporation at four time points during evaporation (from top to bottom): t=0.1t$_f$, 0.3t$_f$, 0.5t$_f$, and 0.6t$_f$. (b) The same images as (a) but with inverted contrast and superimposed vector lines. (c) Sketch of theoretical flow fields adapted from previously reported studies.[10,11]**

One hypothesis for this observation is that, holding all else equal, the ratio of the rate of change in drop height, dh/dt, to particle sedimentation rate, V_s, determines the extent to which colloidal particles accumulate at the air-water interface during evaporation. A greater ratio results in a greater particle fraction accumulating at the drop surface. Physical parameters that affect V_s or dh/dt would necessarily affect particle accumulation at the air-water interface. Two such parameters are particle density and relative humidity. A higher particle density corresponds to a faster sedimentation rate relative to dh/dt and so a lower particle fraction is expected to accumulate at the air-water interface. As discussed previously, polystyrene particle motion at and near the drop surface is influenced by Marangoni stress at early evaporation time points creating flow fields approximately parallel to the glass. During this time, polystyrene particle

63

sedimentation rate is reduced and particles caught in this flow field would be more susceptible to entrapment in the retreating air-water interface than at later evaporation stages when these Marangoni flows subside and particles assume a more downward trajectory. However, it should be noted that the presence of weak Marangoni flow was observed in only one trial and particle accumulation at the interfaces in this trial was no different than that measured in the other two trials. Therefore, the presence of a Marangoni stress does not explain the interfacial accumulation of particles in this study. In fact, the OCT videos included as Supporting Information show the accumulation of particles at the interfaces with no Marangoni flow. The advancing interface provides an explanation for this behavior. Lower relative humidity causes faster evaporation and therefore a faster dh/dt. In this case, the air-water interface falls at a faster rate than in high relative humidity resulting in more particles being caught in the air-water interface.

This hypothesis was tested by comparing the effects of particle density and relative humidity on cross-sectional particle distribution. Figure 4a shows the cross-sectional particle distribution of drops containing three different density particles – polystyrene ("PS", 1μm diameter ρ = 1.04 g/cm^3), melamine formaldehyde ("MF", 1μm diameter, ρ = 1.50 g/cm^3), and silica ("Si", 1μm diameter, ρ = 2.00 g/cm^3) – at three different time points. Physical properties of these particles are summarized in Table 1. As shown in Figure 4, at t = 0.1t_f both the PS and MF particles appear uniformly distributed in the z-direction whereas a significant fraction of the Si particles have already been deposited on the substrate. At t = 0.33t_f, there is an increase in the fraction of PS particles at the air-water interface while a greater fraction of MF particles have accumulated on the glass. The majority of Si particles are on the substrate at this time point. At t = 0.66t_f, a majority of the PS particles have collected at the two interfaces. MF particles at t = 0.66t_f are more uniformly distributed than the PS, but the largest fraction is on the substrate. Si particles at the t = 0.66t_f time point are virtually all on the substrate. These qualitative observations are consistent with our hypothesis that a low particle density and/or a low relative
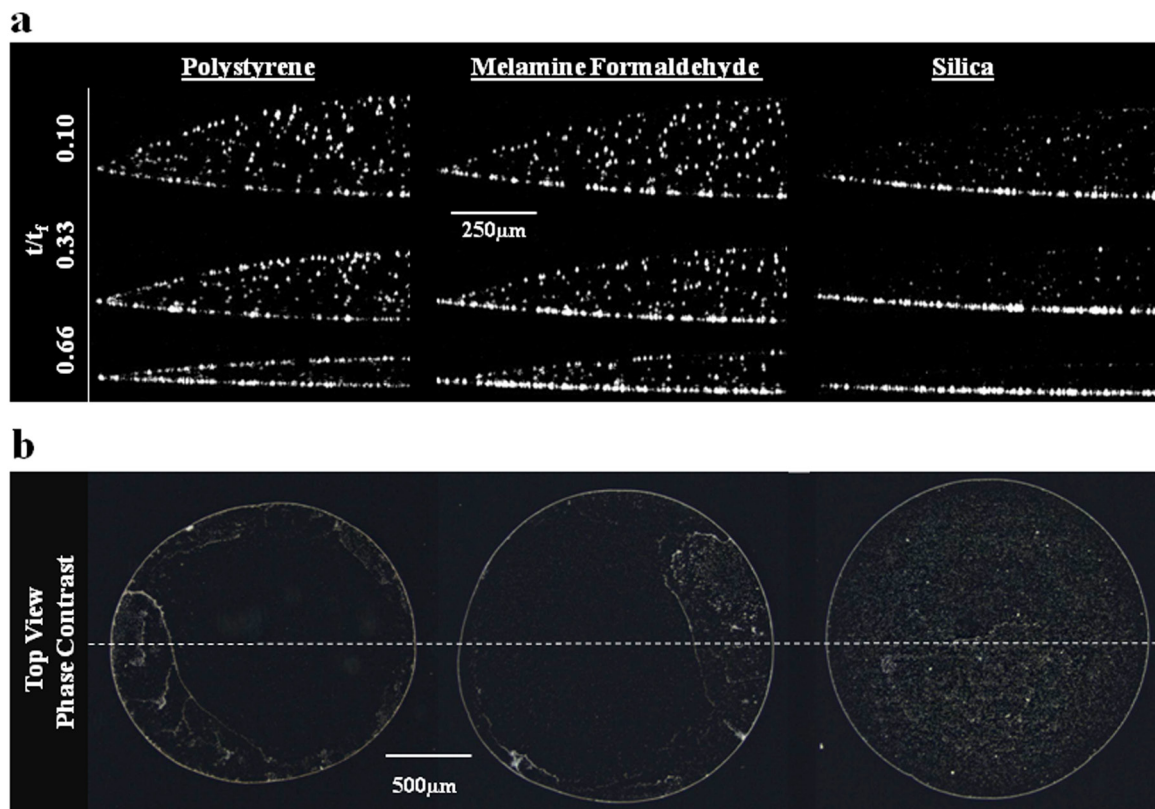
Figure 4. (a) Time-dependent particle accumulation at the air-water interface decreases with an increase in particle density (Si<MF<PS). (b) Corresponding top-down micrographs showing the full diameter of the same dried 1μL drops after complete evaporation show similar outer ring structures and changes in deposition patterns in the drop interior at 2x magnification. The dotted line indicates the orientation of the corresponding OCT slices presented in (a).

The PS, MF, and Si particles, shown in Figure 4, travel in very different trajectories. Video sequences for the time points represented in Figure 4 demonstrate the difference in particle motion (Supporting Information). In contrast to the PS particles, MF particles exhibit a downward sloping vector toward the contact line. Vector slopes decrease with time and distance from both the air-water interface and drop center. Si particles, on the other hand, sediment relatively quickly on the glass substrate.

Unlike the PS particles, the motion of the MF particles in Figure 4 does not show any Marangoni flow. This is likely due to the greater density of melamine formaldehyde ($\rho = 1.50$

65

g/cm^3) versus polystyrene (ρ = 1.04 g/cm^3). According to Stoke's Law, the MF particle sediments in water at 0.27μm/s compared to 0.022μm/s for a PS particle of equal diameter (Table 1). This implies an approximate 10x relative contribution of sedimentation over convection on particle trajectory for the MF particle versus the PS particle.

In theory, a high resolution flow field in the evaporating drop could be mapped by tracking particle motion. However, in this initial report demonstrating the utility of OCT we focus on a simplified analysis in which the velocity and trajectory of low, medium, and high-density particles were tracked for 20s before and after 50% of evaporation. This data is shown in Figure 5. The drop volumes were divided into three sections (see inset). Particle velocity versus angle is plotted in the color corresponding to a particular volume section. This analysis shows that particles accelerate with increasing distance from the drop center, in accordance with the coffee ring effect.[1,2] The plots for all three particle types, PS (Figure 5a), MF (Figure 5b), and Si (Figure 5c), show a rightward shift in particle distributions as the volume sections approach the contact line. If particle motion perfectly tracked pure radial flow with no secondary flow fields, then all data points would be along the overlaid line in Figure 5. The standard deviation of the angles decreases and the mean angle approaches zero as the volume sections approach the contact line. This suggests that particles increasingly move with a trajectory parallel to the substrate as they approach the contact line. This particle motion is evident in Figure 3. With increasing particle density (PS<MF<Si), a greater fraction of ordinate values are negative indicating more particles move in a downward direction. Given the time and computationally-intensive process involved in generating particle tracking data, only one time point was generated in this study (t = 0.5t$_f$). However, a more thorough analysis of particle velocity distributions throughout the entire evaporation process may help explain the observations discussed in this study with respect to interfacial particle accumulation.
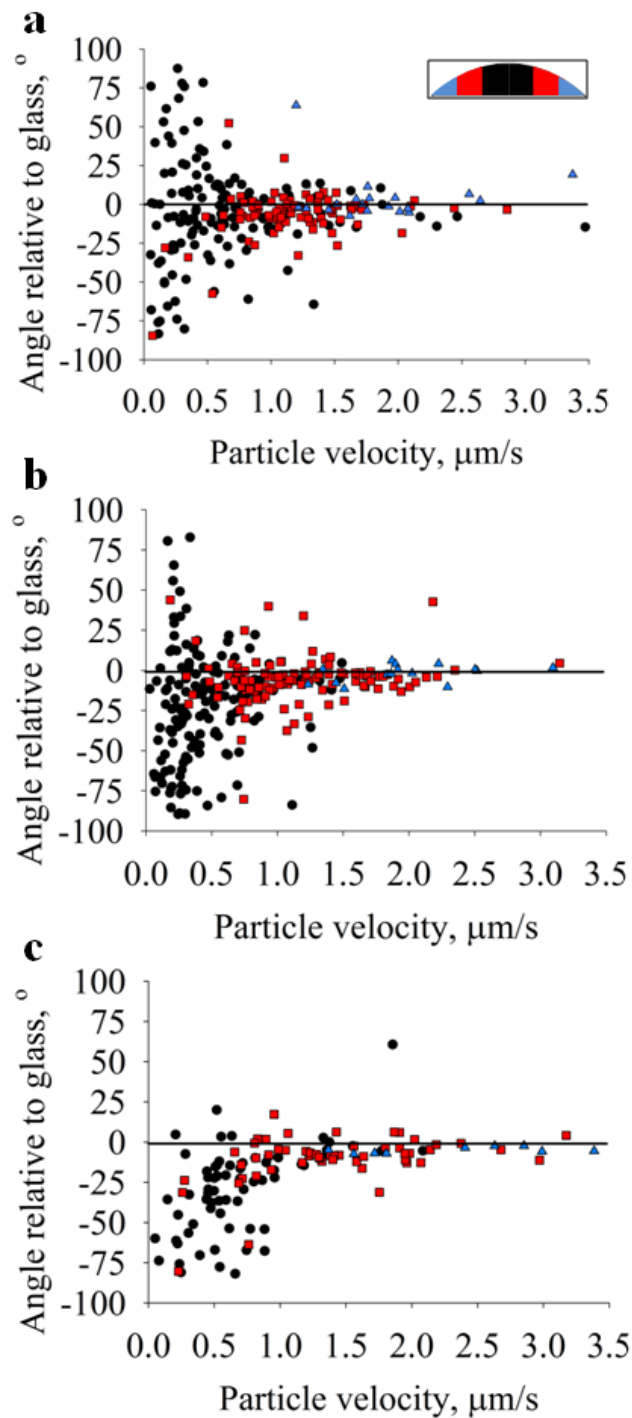
Figure 5. Particle velocities are plotted against direction (angle) at $t=0.5t_f$ for: (a) polystyrene (PS), (b) melamine formaldehyde (MF), and (c) silica (Si). Each plot contains data points from three drop samples. Data points are spatially binned into three sections (inset): inner sections, O; middle sections, □; outer sections, Δ). The Si plot (c) has fewer data points because a majority of particles had reached the glass substrate by $t=0.5t_f$. Particles traveling at a non-zero angle to the glass slide deviate from the pure radial flows as originally described by Deegan et al.[1] and modeled by Hu et al.[7]

One hypothesis is that interfacial particle accumulation is determined, at least in part, by parameters affecting particle sedimentation rate and the rate at which the air-water interface retreats. To test this hypothesis, z-axis particle distributions as a function of normalized evaporation time were quantified for different particle densities and relative humidities and are presented in Figure 6. Particle fraction at the interface was calculated by dividing average pixel intensity for the top or bottom area-of-interest (shown in the inset) by the summation of average pixel intensities for all areas-of-interest. Particle fractions were calculated for each OCT frame, taken at 0.2s intervals, and plotted against normalized evaporation time, t/t_f. Each data series is the average of three experiments and each series is fitted with a linear regression. The plots are discontinuous because only 40s of data could be recorded in a given sequence due to memory limitations of the Bioptigen software, and at the end of each acquisition approximately 20s was required to save the data set and start a new sequence. The y-intercept indicates the particle fraction at the interface at $t/t_f = 0$. If the particles are perfectly uniformly distributed at $t/t_f = 0$, the fraction at the interface would be $\sim .08$. The y-intercepts for PS and MF particle fractions are ~ 0.06. The error is likely due to the average point spread function for the particles as well as the fact that the area-of-interest at the air-liquid interface is rectangular while the interface is a spherical cap. As the drop dries, this interface flattens and the geometry more closely matches the area-of-interest.

The PS particles accumulate at the air-water interface linearly with evaporation time and at a rate approximately four times greater than the MF particles. Particle fractions at the air-liquid interface for each particle density are shown in Figure 6a. MF particles accumulate only slightly at the air-water interface while the fraction of Si particles in the air-water interface declines with evaporation time. These results are consistent with our hypothesis that, all else equal, particle density is inversely related to accumulation at the air-water interface.

68
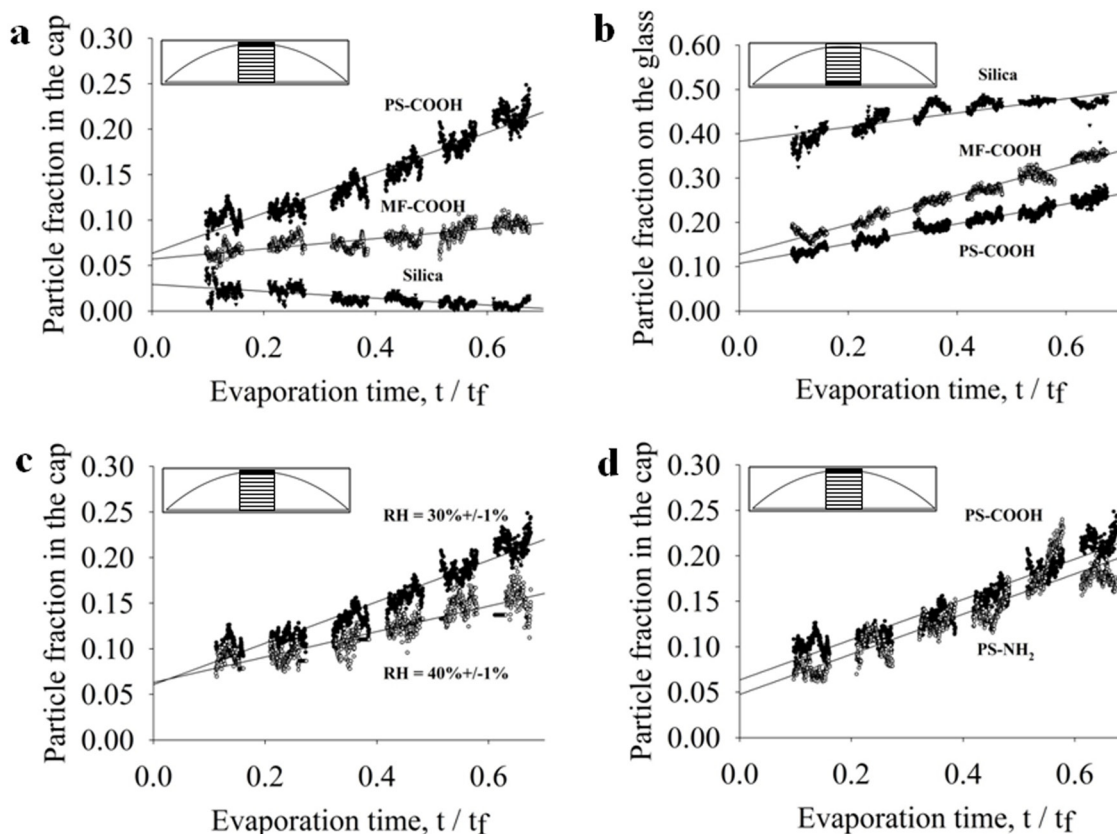
Figure 6. The effect of particle density, relative humidity, and particle surface charge on particle accumulation at the air-water and water-glass interfaces. Vertical distribution of particles in a region defined as 20% of drop diameter at the drop center (see inset) is measured as a function of normalized evaporation time for 1μm particles with different densities ranging from 1.05g/cm^3 (PS), to 1.5 g/cm^3 (MF), and 2.0g/cm^3 (Si) at the air-water interface (a) and water-glass interface (b). Panel (c) shows the rate of accumulation of PS particles at the air-water interface in drops evaporated at 30% and 40% relative humidity, and panel (d) shows the rate of accumulation of negatively charged PS-COOH and positively charged PS-NH$_2$ particles at the air-water interface. Each data set is the average three samples.

Particle density does, in fact, also affect the rate of accumulation at the drop and glass surfaces. Figure 6b shows particle fractions at the water-glass interface for each of the three particle densities. The PS particles accumulate at both interfaces at approximately the same rate. The MF particles accumulate at the water-glass interface at a faster rate than the PS particles but at a slower rate than MF particles at the air-water interface. While the video sequences and time-

lapse OCT images show that the vast majority of Si particles reach the water-glass interface within $t=0.1t_f$, the particle fraction data show only 48% of particles on the glass by $t=0.6t_f$. The reason for this is that so many particles are on the glass substrate that the bottom-most area-of-interest is not tall enough to capture all the particles. In fact, 98% of Si particles are contained within the bottom two areas-of-interest by $t=0.5t_f$. The slope of the linear regression for the Si particle fraction on the glass is less than the other two particle types because most of the Si particles have reached the glass substrate before the first data sequence is captured.

Relative humidity also affects particle accumulation at the air-water interface. This observation is consistent with our hypothesis that particle sedimentation rate and drop evaporation rate affect interfacial particle accumulation since the evaporation rate and dh/dt are greater at lower relative humidity. PS particle fractions at the air-water interface at two different relative humidities are shown in Figure 6c. The diverging slopes of the linear regressions indicate that particles accumulate at the air-water interface more quickly at a lower relative humidity. Goniometer measurements confirm the difference in dh/dt: 0.2918μm/s and 0.8615μm/s for 30% RH and 40% RH, respectively (data not shown). Based on the reports of others that drop evaporation rate, J(t), is a linear process,[1,2] the mass flux for these cases was estimated to be 0.2918μg/s and 0.8615μg/s for 30% RH and 40% RH, respectively.

Particle surface charge does not appear to significantly affect the tendency of PS particles to collect at the air-water interface. Accumulation of negatively charged PS-COOH particles and positively charged PS-NH$_2$ particles at the air-water interface were quantified and are shown in Figure 6d. The slopes of linear regressions for the two data sets are identical suggesting that both positively-charged and negatively-charged particles accumulate at the same rate at the drop surface. This result indicates that interfacial accumulation is independent of particle surface charge.

Brownian motion likely plays a role in the adsorption of particles at the air-water interface. The characteristic diffusion length of a 0.97μm-diameter particle, calculated as $(Dt)^{1/2}$,

70

where D is the diffusion coefficient and t is time, is 0.71μm/s compared to a dh/dt value of 0.3μm/s (30% relative humidity). These values, being the same order of magnitude, imply that Brownian motion plays a role in the entrapment of particles at the interface, but only those particles in close proximity to the interface.

The reason why colloidal PS particles remain adsorbed at air-water interface is not entirely clear. Previous investigations suggest surface tension interactions and buoyancy force can offset particle weight to promote particle adsorption at air-liquid interfaces.[37,38] However, Aveyard et al. have reported that colloidal polystyrene particles of the same size range used in this study do not penetrate the air-liquid interface, but rather settle in an energy barrier just below the interface.[39] Another explanation, not mutually exclusive, is that interparticle electrostatic repulsive forces contribute to particle adsorption at both the air-water and water-glass interfaces in the context of an evaporating drop. As previously discussed, convective flow fields in the drop create a non-uniform vertical distribution of particles. As the drop dries, the distance between the air-water and water-glass interfaces decreases, which increases the interparticle electrostatic force between the two interfaces. In the case of a monodisperse water drop containing carboxylated polystyrene particles, all particles carry a negative surface charge causing this electrostatic force to be repulsive. The distance over which coulombic repulsive forces interact is inversely proportional to the ionic strength of the solution, which effectively screens electrostatic forces. In our studies, particles were suspended in deionized water, and so the charged ions are not present to screen charge effects. The effect of electrostatic interactions on particles adsorbed at an air-liquid interface has been previously described.[39,40] To our knowledge, however, electrostatic interactions between particles at different interfaces separated by a dynamic liquid barrier less than 300μm in height, such as that found in an evaporating drop, has not been described. Further investigation of the nature of particle adsorption at the interfaces of an evaporating drop is warranted but is not investigated here.

The observation made in this report that polystyrene particles accumulate at the air-water interface in a time-dependent manner was also observed by Deegan et al.[1] He observed a 50% shortfall in ring growth compared to the predicted value from his model, which assumed a uniform vertical distribution of particles. Deegan attributed this behavior to the possibility that as particles get close to the air-liquid interface, Marangoni flow would drag particles toward the interface and flow back toward the top-center of the drop.[1,2] However, as previously discussed, Marangoni flow is not prevalent in water drops and therefore this explanation does not completely explain observations made in this study.

Video sequences of polystyrene particle motion taken with OCT imaging suggest that particles accumulated at the air-water and water-glass interfaces enter the ring structure in the final seconds of evaporation (Supporting Information). This may, in part, explain the deviation between Deegan's experimental and predicted values of ring growth. One implication of this finding is that the organization of particles in the ring structure can be controlled by tuning the parameters which affect the degree of non-uniform particle distribution in the vertical direction during drop evaporation. In this initial application of OCT to study evaporating drops, we have shown the effects of particle density and relative humidity. To demonstrate the effect of non-uniform, vertical particle distribution on ring structure, residue patterns of drops containing a mixture of particles with different densities were analyzed. A less dense particle like polystyrene tends to accumulate more at the air-water interface and enter the ring structure later in the evaporation process whereas a more dense particle like melamine formaldehyde is transported to the drop edge by the coffee ring effect throughout the evaporation process. As a result, the ring structure of a drop containing both particle types is not homogeneous but rather organized by the arrival time of particles at the drop's edge.

We tested this explanation and our results indicate that particle density can be used to control radial deposition order. Applying these insights to control ring structure, final residue patterns of drops containing different density fluorescent particles were imaged with

fluorescence microscopy (Figure 7). Figure 7a shows a fluorescence micrograph of the ring structure of a dried drop containing all three particle types, PS (red), MF (green), and Si (blue) at a ratio of 2:1:1, respectively. In Figure 7b the green MF particles have been substituted with a green PS particle so the ring structure contains equal fractions of two different PS particles (one red and one green) and blue Si particles. A corresponding fluorescence line profile indicates the particle composition along the white line drawn through the ring structure. The line profiles of the two ring structures show a shift in the spatial distribution of particle type at the ring depending on whether or not the MF particle type is present. With all three particle types (Figure 7a), the inner region of the ring structure (away from the contact line) is mostly comprised of red PS particles while the majority of MF particles are settled at the outside region (contact line) of the ring structure. The greatest fraction of Si particles is in the middle of the ring structure. When the MF particle type is replaced with another PS particle type, all three particles (red PS, green PS, and blue Si) have almost identical distributions in the ring structure. The resulting partial separation of particles in the ring structure creates an altered color pattern because polystyrene particles (red) accumulate on the surface of the drop, enter the ring structure later in evaporation, and are deposited at the inner areas of the ring. The melamine formaldehyde particles (green) are transported to the ring by the coffee ring effect throughout evaporation and therefore are deposited at the outer areas of the ring.
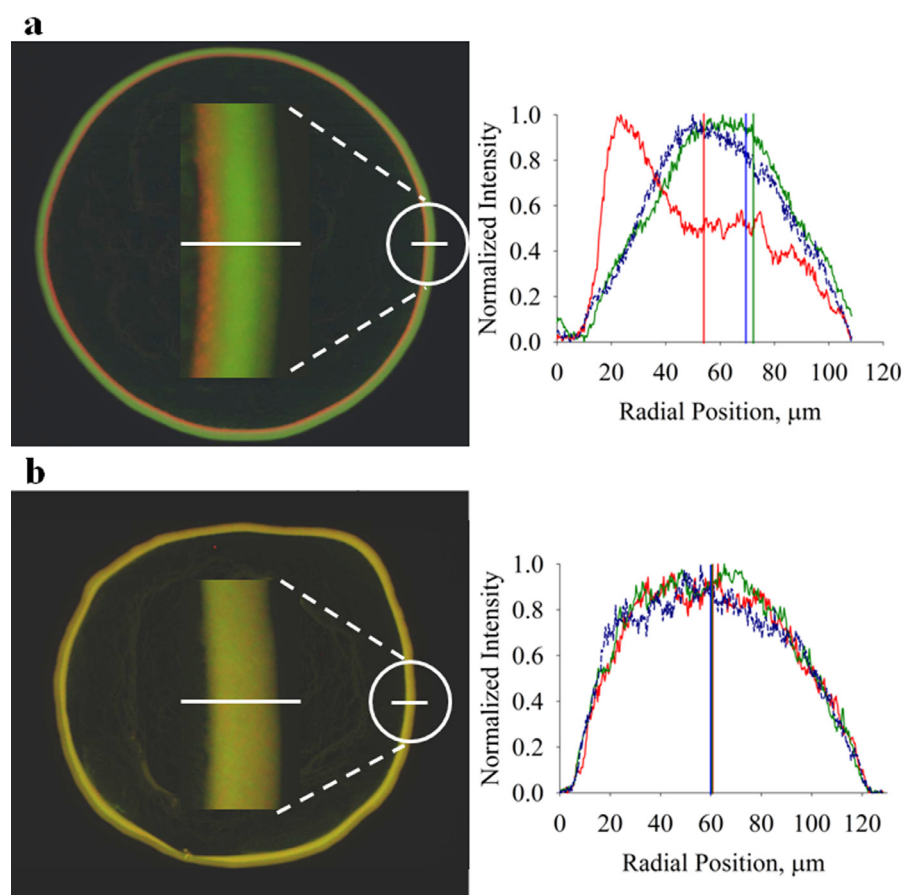
Figure 7. Particle density alters the final coffee ring structure in dried drops. Ring structures of dried, 1μL water drops containing a mixture of different density particles imaged by fluorescence microscopy: (a) 1:2:1 mixture of PS-COOH (red), MF-COOH (green), and Silica (blue), (b) equal fractions of PS-COOH (red), PS-COOH (green), Silica (blue). The fluorescence profiles for the corresponding white line through the ring structure show that radial particle organization at the ring is partly determined by the densities of constituent particles. The red PS-COOH particles are shifted to the left in (a) because a greater fraction of these particles are trapped in the air-water interface compared to the MF-COOH and Si particles, causing them to enter the ring structure at later times compared to MF-COOH and Si particles. When the MF-COOH particle is replaced by a PS-COOH particle (green), all particles enter the ring at approximately the same time (b).

Particle tracking in evaporating drops using OCT has several experimental artifacts. First, in order to minimize specular reflectance on the drop surface, the OCT laser was adjusted to a 9° angle from the normal causing as much as 10% error in particle coordinate data. Additionally, the curvature of the drop surface refracts the incident laser causing lensing in the OCT images. This manifests as a slightly curved substrate in the OCT images that flattens with evaporation time. The greatest amount of refractive error occurs where the angle of the drop surface is greatest relative to the substrate, which occurs at the air-water-glass interface at t=0. This error is quantified as the difference between the actual and perceived location of a particle near the contact line assuming a worst case contact angle of 20°. Under these conditions, the refractive error is less than 1%. No attempt is made to correct for this artifact in this study since the error that it causes appears to be negligible for the purposes of this investigation. In future studies, this artifact can likely be offset during the signal processing of the OCT data. Another type of artifact that contributes to the curved appearance of the bottom of the drop in the OCT images is a mismatch in optical path length, which equals the refractive index times the actual distance. The mismatch arises from the difference in refractive index between air (n=1) and water (n=1.33). A maximum drop height of 300μm can appear as large as 300μm x 1.33 = 399μm. This artifact, while non-trivial in appearance, is negligible in terms of particle tracking because particle velocity is calculated as the difference in particle position relative to the previous frame. The error term in this calculation is based only on the change in drop height that occurs between frames, which is <<1μm. This artifact exists only in the vertical direction, and most of the particle motion occurs in the radial direction. Therefore, we consider this artifact also to be negligible. The particle distribution calculations are not affected by the lensing effect or optical path length artifacts because these calculations are fractional calculations relative to average intensity summed over all areas of interest.

Another artifact arises from the optical resolution of the OCT system, approximately 8μm in the lateral direction, being greater than the 1μm-diameter particles used in the study. As

a result, a single object may in fact represent more than one particle. However, the particle solutions used in the study have a sufficiently low concentration of particles to minimize the effect of this artifact, which affects particle size, not position. Another potential source of measurement variability in system is particle concentration. The number of particles per drop was determined based on the number required to pin the contact line and provide sufficient representation of the flow fields without overcrowding the image. If there are too few particles in the water drop, then the contact line will not pin and the coffee ring effect is not established.[41] If too many particles are present then it is difficult to resolve an individual particle in sequential images, which is necessary for particle tracking and resolving flow fields. A particle concentration of 10^5 per 1μL drop was determined to sufficiently fulfill these requirements. However, the effect of particle concentration on the observations discussed in this study has not been determined. Finally, it is possible the OCT laser itself may cause temperature-induced changes in flow fields in the drop. However, the 860nm laser used in this study with just 700μW incident on the sample coincides with near minimal absorption by water and so temperature effects are relatively insignificant.[42]

Conclusions

This work demonstrates that optical coherence tomography effectively tracks particle motion in evaporating drops and provides a new experimental strategy for determining primary and secondary flow fields, interfacial particle accumulation, and dynamic changes in these flow fields. A time-dependent, non-uniform distribution of particles in the z-direction was observed. In addition, low particle density, and low relative humidity promote particle accumulation at the air-water interface in an evaporating drop. These insights were applied to show that the radial organization of the ring structure is partly controlled by the ratio of different density colloidal particles.

Acknowledgements

Abbreviations

OCT   Optical coherence tomography

PS   Polystyrene

MF   Melamine formaldehyde

Si   Silica
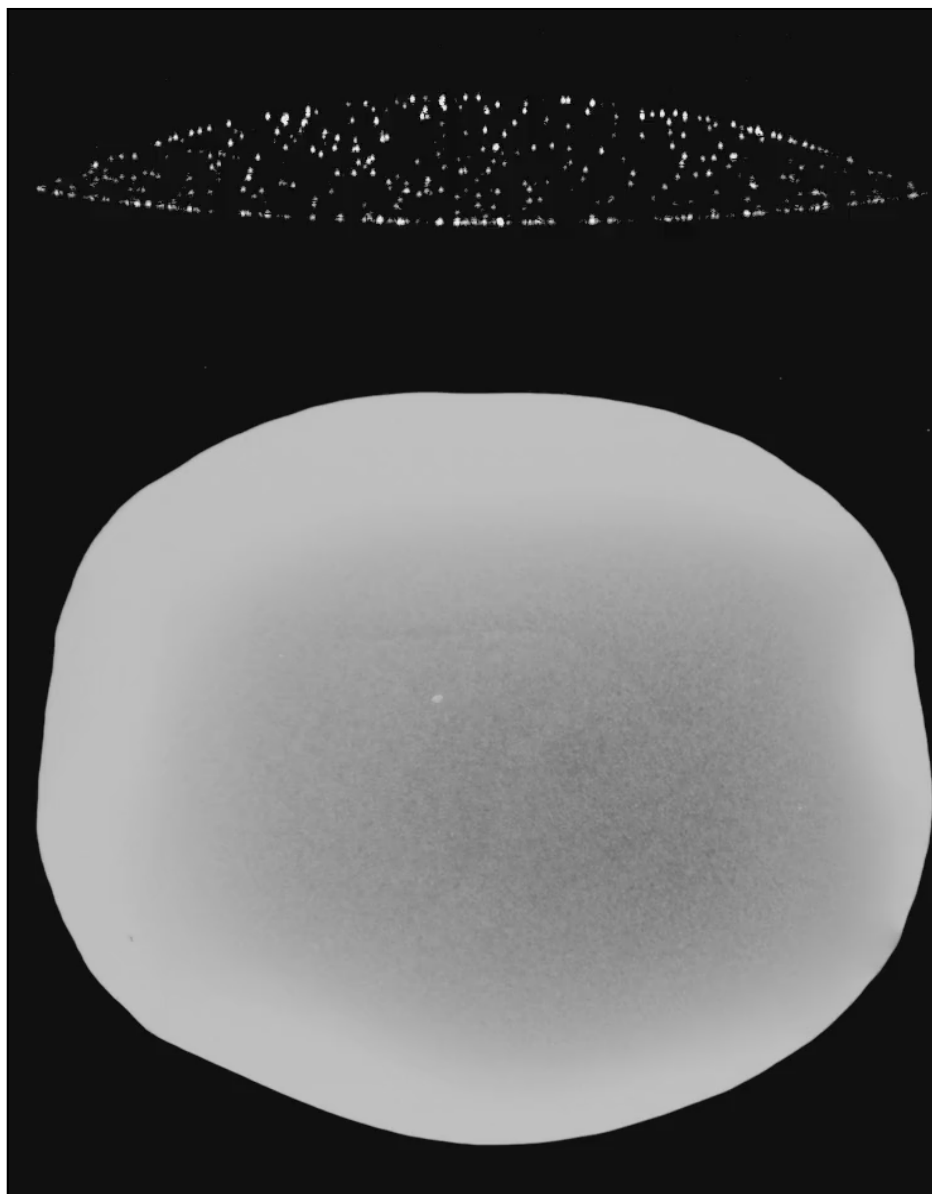
Video 1. Comparison of the flow fields in a 1μL evaporating water drop on a glass slide from two different view points: a cross-sectional video using OCT (top panel) and a top-down video using phase contrast microscopy (bottom panel). Different drops are shown, both containing 1μm-diameter, polystyrene particles (carboxylated). The OCT video was taken of a drop containing 10^5 particles and was generated by concatenating a series of sequences with 20s pauses between sequences. Each sequence consists of 200 frames recorded at 5 frames per second, or 40s total time per sequence. The microscopy video was taken of a drop containing 10^6 particles. Both videos begin at 1min into evaporation. Both drops were dried in similar ambient conditions of 30% relative humidity and 22°C.
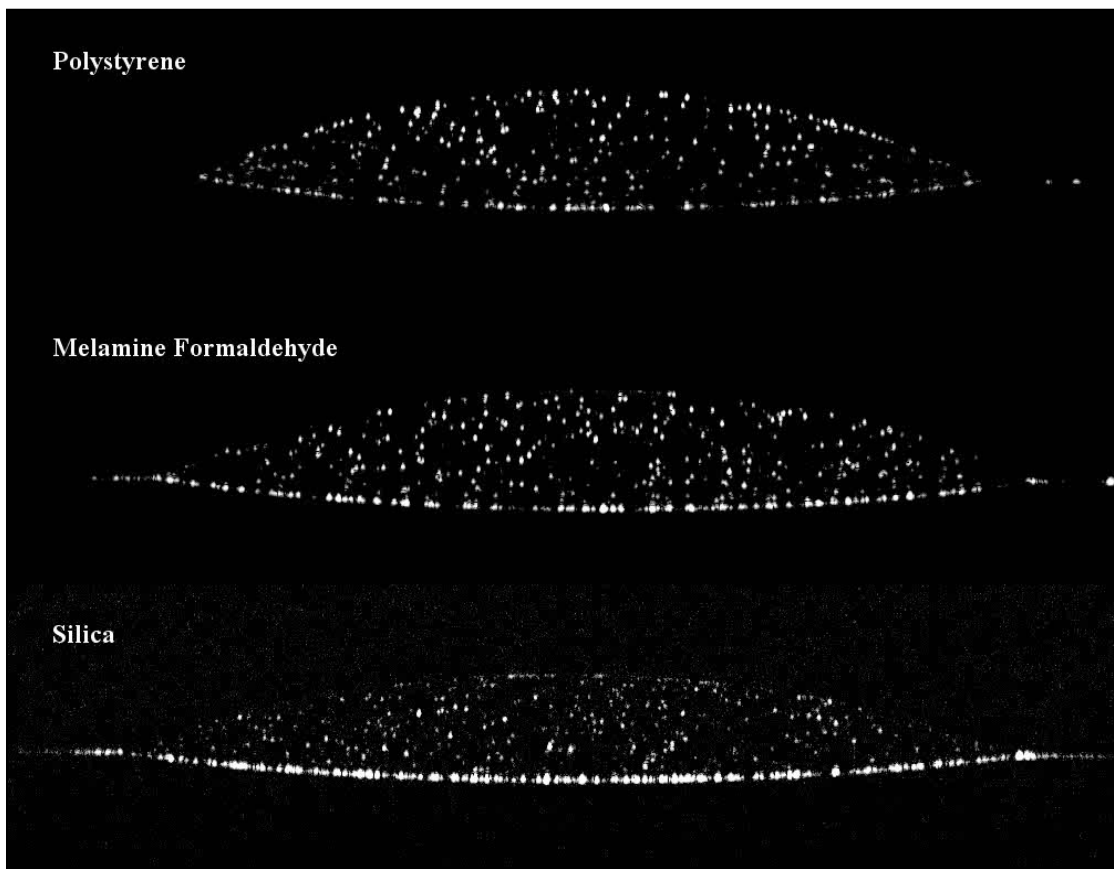
Video 2. **Cross sectional OCT imaging of 1μL water drops containing different density, 1μm-diameter particles: polystyrene (top panel, density = 1.05 g/cm^3), melamine formaldehyde (middle panel, density = 1.5 g/cm^3), and silica (bottom panel, density = 2.0 g/cm^3). All three drops are on a clean glass slide, and all were dried in similar ambient conditions of 30% relative humidity and 22°C. All three videos begin at 1min into evaporation.**

References

     (1)   Deegan, R. D.; Bakajin, O.; Dupont, T. F.; Huber, G.; Nagel, S. R.; Witten, T. A.: Contact line deposits in an evaporating drop. *Physical Review E* **2000**, *62*, 756-765.

     (2)   Deegan, R. D.: Pattern formation in drying drops. *Physical Review E* **2000**, *61*, 475-485.

     (3)   Deegan, R. D.; Bakajin, O.; Dupont, T. F.; Huber, G.; Nagel, S. R.; Witten, T. A.: Capillary flow as the cause of ring stains from dried liquid drops. *Nature* **1997**, *389*, 827-829.

     (4)   Dugas, V.; Broutin, J.; Souteyrand, E.: Droplet evaporation study applied to DNA chip manufacturing. *Langmuir* **2005**, *21*, 9130-9136.

     (5)   Kawase, T.; Shimoda, T.; Newsome, C.; Sirringhaus, H.; Friend, R. H.: Inkjet printing of polymer thin film transistors. *Thin Solid Films* **2003**, *438*, 279-287.

     (6)   Sirringhaus, H.; Kawase, T.; Friend, R. H.; Shimoda, T.; Inbasekaran, M.; Wu, W.; Woo, E. P.: High-resolution inkjet printing of all-polymer transistor circuits. *Science* **2000**, *290*, 2123-2126.

     (7)   Hu, H.; Larson, R. G.: Analysis of the microfluid flow in an evaporating sessile droplet. *Langmuir* **2005**, *21*, 3963-3971.

     (8)   Bhardwaj, R.; Fang, X. H.; Somasundaran, P.; Attinger, D.: Self-Assembly of Colloidal Particles from Evaporating Droplets: Role of DLVO Interactions and Proposition of a Phase Diagram. *Langmuir* **2010**, *26*, 7833-7842.

     (9)   Yunker, P. J.; Still, T.; Lohr, M. A.; Yodh, A. G.: Suppression of the coffee-ring effect by shape-dependent capillary interactions. *Nature* **2011**, *476*, 308-311.

     (10)   Hu, H.; Larson, R. G.: Marangoni effect reverses coffee-ring depositions. *Journal of Physical Chemistry B* **2006**, *110*, 7090-7094.

     (11)   Hu, H.; Larson, R. G.: Analysis of the effects of Marangoni stresses on the microflow in an evaporating sessile droplet. *Langmuir* **2005**, *21*, 3972-3980.

     (12)   Nguyen, V. X.; Stebe, K. J.: Patterning of small particles by a surfactant-enhanced Marangoni-Benard instability. *Physical Review Letters* **2002**, *88*.

     (13)   Truskett, V.; Stebe, K. J.: Influence of surfactants on an evaporating drop: Fluorescence images and particle deposition patterns. *Langmuir* **2003**, *19*, 8271-8279.

     (14)   Still, T.; Yunker, P. J.; Yodh, A. G.: Surfactant-Induced Marangoni Eddies Alter the Coffee-Rings of Evaporating Colloidal Drops. *Langmuir* **2012**, *28*, 4984-4988.

     (15)   Ristenpart, W. D.; Kim, P. G.; Domingues, C.; Wan, J.; Stone, H. A.: Influence of substrate conductivity on circulation reversal in evaporating drops. *Physical Review Letters* **2007**, *99*.

(16)   Wong, T. S.; Chen, T. H.; Shen, X. Y.; Ho, C. M.: Nanochromatography Driven by the Coffee Ring Effect. *Analytical Chemistry* **2011**, *83*, 1871-1873.

(17)   Brutin, D.; Sobac, B.; Loquet, B.; Sampol, J.: Pattern formation in drying drops of blood. *Journal of Fluid Mechanics* **2011**, *667*, 85-95.

(18)   Tarasevich, Y. Y.; Pravoslavnova, D. M.: Segregation in desiccated sessile drops of biological fluids. *European Physical Journal E* **2007**, *22*, 311-314.

(19)   Tarasevich, Y. Y.; Pravoslavnova, D. M.: Drying of a multicomponent solution drop on a solid substrate: Qualitative analysis. *Technical Physics* **2007**, *52*, 159-163.

(20)   Trantum, J. R.; Wright, D. W.; Haselton, F. R.: Biomarker-Mediated Disruption of Coffee-Ring Formation as a Low Resource Diagnostic Indicator. *Langmuir* **2012**, *28*, 2187-2193.

(21)   Kajiya, T.; Kaneko, D.; Doi, M.: Dynamical Visualization of "Coffee Stain Phenomenon" in Droplets of Polymer Solution via Fluorescent Microscopy. *Langmuir* **2008**, *24*, 12369-12374.

(22)   Popov, Y. O.: Evaporative deposition patterns: Spatial dimensions of the deposit. *Physical Review E* **2005**, *71*.

(23)   Barash, L. Y.; Bigioni, T. P.; Vinokur, V. M.; Shchur, L. N.: Evaporation and fluid dynamics of a sessile drop of capillary size. *Physical Review E* **2009**, *79*.

(24)   Bodiguel, H., Leng J.: Imaging the drying of a colloidal suspension: Velocity field. *Chemical Engineering and Processing: Process Intensification* **2012**.

(25)   Bodiguel, H.; Leng, J.: Imaging the drying of a colloidal suspension. *Soft Matter* **2010**, *6*, 5451-5460.

(26)   Drexler, W.: Ultrahigh-resolution optical coherence tomography. *Journal of Biomedical Optics* **2004**, *9*, 47-74.

(27)   Ahn, Y. C.; Jung, W. G.; Chen, Z. P.: Optical sectioning for microfluidics: secondary flow and mixing in a meandering microchannel. *Lab on a Chip* **2008**, *8*, 125-133.

(28)   Jonas, S.; Bhattacharya, D.; Khokha, M. K.; Choma, M. A.: Microfluidic characterization of cilia-driven fluid flow using optical coherence tomography-based particle tracking velocimetry. *Biomedical Optics Express* **2011**, *2*, 2022-2034.

(29)   Wang, L.; Xu, W.; Bachman, M.; Li, G. P.; Chen, Z. P.: Phase-resolved optical Doppler tomography for imaging flow dynamics in microfluidic channels. *Applied Physics Letters* **2004**, *85*, 1855-1857.

(30)   Wang, L.; Xu, W.; Bachman, M.; Li, G. P.; Chen, Z. P.: Imaging and quantifying of microflow by phase-resolved optical Doppler tomography. *Optics Communications* **2004**, *232*, 25-29.

(31)   Tucker-Schwartz, J. M.; Meyer, T. A.; Patil, C. A.; Duvall, C. L.; Skala, M. C.: In vivo photothermal optical coherence tomography of gold nanorod contrast agents. *Biomedical Optics Express* **2012**, *3*, 2881-2895.

(32)   Wojtkowski, M.; Srinivasan, V. J.; Ko, T. H.; Fujimoto, J. G.; Kowalczyk, A.; Duker, J. S.: Ultrahigh-resolution, high-speed, Fourier domain optical coherence tomography and methods for dispersion compensation. *Opt Express* **2004**, *12*, 2404-2422.

(33)   Berteloot, G.; Hoang, A.; Daerr, A.; Kavehpour, H. P.; Lequeux, F.; Limat, L.: Evaporation of a sessile droplet: Inside the coffee stain. *Journal of Colloid and Interface Science* **2012**, *370*, 155-161.

(34)   Harris, M. T.; Widjaja, E.: Particle deposition study during sessile drop evaporation. *Aiche Journal* **2008**, *54*, 2250-2260.

(35)   Marin, A. G.; Gelderblom, H.; Lohse, D.; Snoeijer, J. H.: Order-to-Disorder Transition in Ring-Shaped Colloidal Stains. *Physical Review Letters* **2011**, *107*.

(36)   Savino, R.; Paterna, D.; Favaloro, N.: Buoyancy and Marangoni effects in an evaporating drop. *Journal of Thermophysics and Heat Transfer* **2002**, *16*, 562-574.

(37)   Ally, J.; Kappl, M.; Butt, H. J.; Amirfazli, A.: Detachment Force of Particles from Air-Liquid Interfaces of Films and Bubbles. *Langmuir* **2010**, *26*, 18135-18143.

(38)   Vella, D.; Mahadevan, L.: The "Cheerios effect". *American Journal of Physics* **2005**, *73*, 817-825.

(39)   Aveyard, R.; Clint, J. H.; Nees, D.; Paunov, V. N.: Compression and structure of monolayers of charged latex particles at air/water and octane/water interfaces. *Langmuir* **2000**, *16*, 1969-1979.

(40)   Ghezzi, F.; Earnshaw, J. C.; Finnis, M.; McCluney, M.: Pattern formation in colloidal monolayers at the air-water interface. *Journal of Colloid and Interface Science* **2001**, *238*, 433-446.

(41)   Sangani, A. S.; Lu, C. H.; Su, K. H.; Schwarz, J. A.: Capillary force on particles near a drop edge resting on a substrate and a criterion for contact line pinning. *Physical Review E* **2009**, *80*.

(42)   J.A. Curcio, C. C. P.: The Near Infrared Absorption Spectrum of Liquid Water. *Journal of the Optical Society of America* **1951**, *41*, 1.

CHAPTER V

BIOSENSING IN AN EVAPORATING DROP

Joshua R. Trantum[1]
Mark L. Baglia[1]
Zachary E. Eagleton[1]
Raymond L. Mernaugh[2]
Frederick R. Haselton[1]

[1]Department of Biomedical Engineering
[2]Department of Biochemistry
Vanderbilt University
Nashville, Tennessee

Abstract

Effective point-of-care diagnostics require a biomarker detection strategy that is low-cost and simple-to-use while maintaining a high performance capability. Here we report a biosensor design that combines an immuno-agglutination assay with the hydrodynamics of an evaporating drop to generate an optically detectable signal. We use the bacteriophage, M13K07, as a model biomarker and achieve a 96fM limit-of-detection. The substrate material is shown to influence evaporation-induced hydrodynamics in real-time imaging using optical coherence tomography. Evaporation-driven flow fields generate signal in the assay on a PDMS substrate but not substrates with greater thermal conductivity like indium tin oxide-coated glass. Approximately 80% of the maximum signal is generated within 10 minutes of evaporating a 1μL drop of reacted sample enabling a relatively quick result. Although standard microscopy-based techniques are employed to measure signal in the assay, the biosensor design described in this report could also be used with a camera phone to image and interpret the test result in future applications.

Introduction

The engineering of diagnostic devices suitable for the low resource, point-of-care (POC) setting is challenged by design criteria that include low cost, simplicity of operation, and minimal reliance on external instrumentation.[1,2] The ideal biosensor requires no on-board power source or external input and produces an easily detectable signal in a short period of time. Harnessing the hydrodynamics of an evaporating drop represents one possible means of satisfying these design requirements. First described by Deegan, and commonly referred to as the coffee ring effect, colloidal particles in an evaporating drop tend to travel to the periphery causing a non-uniform, concentrated ring pattern after drying.[3-5] The physical basis of this naturally-occurring phenomenon as well as fluid and particle motion during drop evaporation has been previously described.[6-9]

Recently, several groups have reported using the hydrodynamics of an evaporating drop

84

to discern information about the components of the solution. Wong et al. demonstrated that the size exclusion geometry of the contact line in an evaporating drop can be used for chromatographic separation of colloidal particles.[10] Several groups have shown that dried patterns of drops of biological fluids can be used to characterize sample components and potentially be used as an indicator of disease.[11-13] Teste et al have shown how a magnetic bead-based immuno-agglutination assay can be performed in confined droplets on a microfluidic device with 100pM limit of detection.[14] A diagnostic assay in which the coffee ring effect organizes functionalized particles to generate a colorimetric response based on the presence of a biomarker also been recently reported.[15] Assay limitations of this latter study motivated this report. This previous assay design achieved a relatively high limit of detection of approximately 200nM and had the additional limitations of not working in a solution containing physiologic salinity and requiring drop deposition aligned over a magnetic field. Here we present an assay based on an evaporating drop that overcomes these limitations. The biosensor design reported here is an immuno-agglutination assay that uses Marangoni flow, rather than the coffee ring effect, to generate an optically detectable signal by concentrating biomarker-induced aggregates at the centre of an evaporating drop. The limit of detection is greatly reduced compared to this previous assay design. Also, the assay presented in this study, unlike this previous design, is functional in the presence of physiologic salinity and does not require aligning the drop over a magnetic field.

Materials and Methods

Particle functionalization & characterization

Streptavidin-coated, monodisperse, superparamagnetic particles with a mean diameter of 1μm were obtained from Life Technologies (P/N 656.01). Particles were magnetically washed three times with phosphate-buffered saline (PBS, pH 7.4) containing 0.01% Tween 20 and resuspended in the same buffer at a 10x dilution from the stock concentration. Mouse αM13 monoclonal antibody (1mg/mL in PBS) was purchased from GE Healthcare (P/N 2792001 and biotinylated with biotinamidohexanoic acid N-hydroxysuccinimide ester purchased from Sigma Aldrich (P/N B2673). Unreacted ester groups were subsequently quenched with Tris buffer after a two-hour incubation period. Biotinylated antibody was added to the washed particle solution at an equivalent ratio of 1mg antibody per 1mL of stock particles. The particle solutions were then magnetically washed with PBS containing 0.01% Tween 20 three times following a two-hour incubation period. Free biotin was then added to the particle solution to bind any unreacted streptavidin on the surface of the particles. After 30 minutes, the particles were then magnetically washed three times and stored in PBS containing 0.005% Tween 20 and 0.005% bovine serum albumin (BSA). Control particles were prepared using the same base particle and reacting with a molar excess of free biotin and then washing three times and storing in PBS with 0.005% Tween 20 and 0.005% BSA. The presence of conjugated antibody on the particles was confirmed by reacting the particles with a α-mouse secondary antibody/horseradish peroxidase conjugate (Sigma Aldrich, P/N A4416), washing three times, and then developing with 2,2'-azino-bis(3-ethylbenzothiazoline-6-sulphonic acid (ABTS) with hydrogen peroxide. This procedure was repeated for the control particles. Developed solutions turned green for the antibody-conjugated particles and remained clear for the control particles.

Immuno-agglutination assay procedure

Titration assays were carried out in small volume terasaki plates (Nunc, P/N 438733). Plates were first blocked with PBS containing 0.1% Tween 20 and 0.1% BSA, and then rinsed three times with PBS containing 0.1% Tween 20. M13 bacteriophage suspended in PBS was added to the plate and then serially diluted down the rows of the plate with PBS. An equal volume of particle solution containing 3×10^6 particles per µL (in PBS with 0.005% BSA and 0.005% Tween 20) was then added to each well and mixed. An equal volume of water containing 25% glycerol and 0.02% Tween 20 was then added to each well. Particle solutions were allowed to react with M13 target for 30 min before depositing drops on the substrate for evaporation and image analysis.

Cross-sectional imaging procedure

A drop (1µL) of reacted particle solution was deposited on a substrate, and cross-sectional images were recorded with optical coherence tomography (OCT). The procedure and experimental set-up were identical to a previously reported study using a commercial OCT system (Bioptigen, Inc.).[6] The experimental set-up resulted in an optical resolution of approximately 8µm in the lateral direction, defined as the full-width half-max of the point-spread function of the system, and 6.4µm in the axial direction. Transverse digital sampling resolution was 3µm/pixel with an axial digital sampling resolution of 1.69µm/pixel. OCT files were converted to tagged image file (TIFF) format in Matlab, and ImageJ software was used to edit video sequences and image stacks.

Drop imaging procedure and signal analysis

Evaporated drops were imaged utilizing an Eclipse TE2000-U inverted microscope system (Nikon) at with a 10X objective. The slide was front-illuminated using a 144 LED stereo microscopy light (AmScope). Images of the dried drops were captured using a Zyla sCMOS

camera (Andor Technologies) and Elements AR software (Nikon Instruments). During capture, each drop was manually centred in the field of view of the objective and manually focused using focus guides integrated into the software. Final images were captured in 11-bit greyscale at a capture resolution of 0.34μm/pixel. All images were then processed in Elements to assess the degree of aggregation at the centre of the drop. In order to account for variation in drop size, each drop was measured in Elements by creating a threshold mask of the drop and then measuring the size of the map in pixels. This data was then converted to an equivalent diameter which was used for normalization purposes during processing. After equivalent diameters were calculated, all images were cropped to 340μm x 340μm and a circular region of interest with diameter of 340μm was selected. This region was selected because it was large enough to encompass central aggregates for all drops, but small enough so as to exclude refraction artefacts occurring at the periphery. Particle identification was then performed on the cropped images with a brightness threshold set at the midpoint of the 11-bit brightness spectrum (luminosity$\geq$ 1024). In order to exclude free particles and only count aggregates, particle identification was further restricted to include only objects greater than 50μm in size. This process was performed identically on both αM13-functionalized particles and biotin control samples.

Data was processed by averaging all captured data for each sample at each concentration resulting in n = 15 for each anti-M13 concentration (5 samples in triplicate) and n = 3 (one sample in triplicate) for each biotin control sample. Total particle intensity and mean total particle area were taken from the output of the particle identification process for each drop. These values were normalized to drop size by dividing by drop diameter squared for total particle area and dividing by drop diameter cubed for total particle intensity. Overall means for each test concentration were then calculated as a ratio to mean values for the 0pM test group and then limit of detection was determined using a logarithmic curve fit and interpolation to calculate the concentration at which projected area and intensity, respectively, would be three standard deviations above the 0pM mean.

Results and Discussion

The immuno-agglutination assay investigated here uses Marangoni flow in an evaporating drop to concentrate aggregated particles at the centre of a drop for easy optical detection. Figure 1a shows a cross-sectional representation of the theoretical Marangoni flow arising from the temperature and surface tension gradients in the drop of evaporating solution.[8] The direction of Marangoni flow is in the direction of the three-phase contact line (air-liquid-substrate) along the drop surface and toward the drop centre along the substrate. The temperature gradient from which these flow fields arise is caused by the non-uniform evaporative flux along the drop surface. Originally described by Deegan, the evaporation rate of a drop is greatest at the contact line due to the proximal location of ambient, unsaturated gas resulting in non-uniform evaporation along the air-liquid interface.[3-5] The extent to which non-uniform evaporative cooling effects result in a temperature gradient along the drop surface is determined by the rate of heat transfer from the isothermal substrate to the air-liquid interface.[16] These heat transfer rates are, in part, a function of both the drop height as well as the thermal conductivities of the substrate and liquid. If the thermal conductivity of the substrate is sufficiently low, then evaporative cooling dominates and causes the lowest temperature to occur at the contact line. Conversely, a highly thermally conductive substrate promotes sufficient heat transfer at the contact line to overcome evaporative cooling effects resulting in the greatest temperature at the drop edge and lowest at the centre. These temperature gradients cause surface tension gradients which in turn drive the Marangoni flow. According to Ristenpart et al, the drop is coolest at the contact line if the substrate has a thermal conductivity less than 1.45 times that of the liquid causing fluid to flow in the direction indicated in Figure 1a.[16] If the substrate has a thermal conductivity greater than 2 times that of the liquid, the flow direction is reversed. The PDMS substrate used in the research reported here has a thermal conductivity of 0.15 W/mK, well below 1.45 times the liquid thermal conductivity.[17] According to Ristenpart et al, the resulting flow direction should be the one shown in Figure 1a. Moreover, these Marangoni flow fields are

89

axisymmetric around the drop centre resulting in a toroidal geometry when viewed from above the drop. Figure 1b shows a three-dimensional rendering of these flow fields showing symmetry around the drop centre.
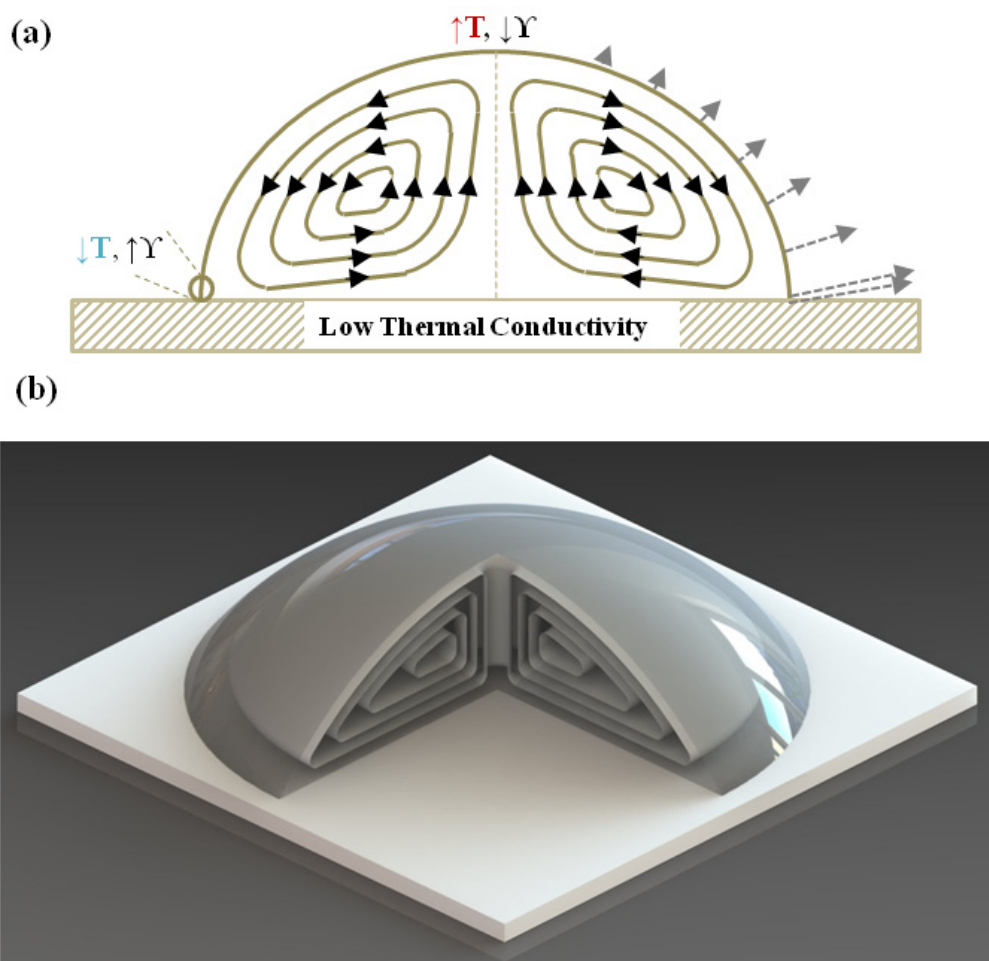
Figure 1. **(a) A non-uniform evaporation rate along the drop surface combined with a low thermally conductive substrate causes temperature (T) and surface tension (Υ) gradients that drive Marangoni flow, (b) A 3-D rendered drawing of the cross-sectional Marangoni flow in (a) shows radial symmetry around the drop center.**

These internal flows and biomarker-induced aggregation are the two basic elements of this approach. A schematic of the assay is presented in Figure 2. Particles (1μm diameter) are surface functionalized with monoclonal antibody that binds epitopes on the target biomarker (Figure 2a, left). In this proof-of-concept study, the bacteriophage, M13K07, is used as a model biomarker. The bacteriophage, commonly used for phage display, is a cigar-shaped viral capsid with 2,800 surface-bound epitopes. Particles become cross-linked in the presence of biomarker resulting in aggregate formation (Figure 2a, right). When a drop of this solution is deposited on a

PDMS substrate, Marangoni flow fields circulate particles in solution (Figure 2b). In the absence of biomarker, particles follow these flow fields and are eventually deposited across the substrate surface and predominately at the drop edge resulting in a ring pattern (Figure 2c, left). In the presence of biomarker, aggregated particles rapidly settle to the substrate and are then transported to the drop centre by the Marangoni flow fields resulting in a concentrated spot (Figure 2c, right). Due to non-specific particle binding events, a baseline amount of aggregated particles settle at the drop centre in the absence of target biomarker and represents noise in the system.
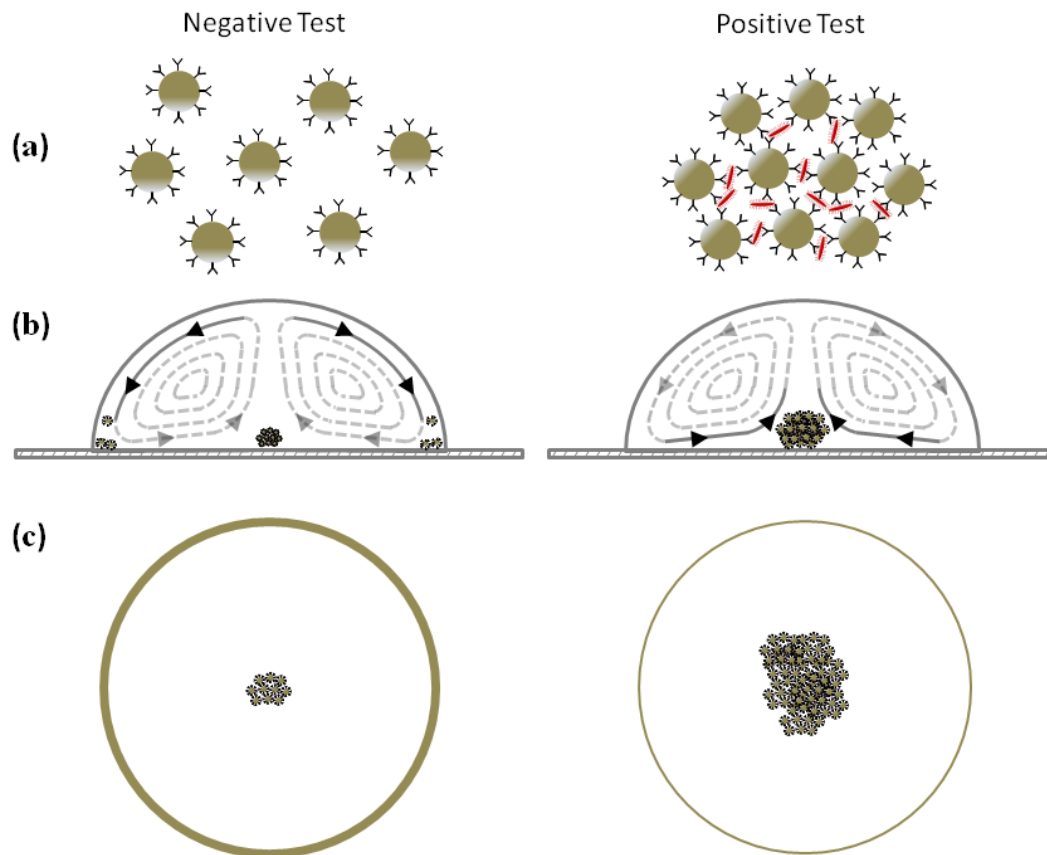
Figure 2. Schematic of the assay: (a) A sample is mixed with a solution containing 1µm-diameter particles that are surface-functionalized with αM13 antibody. Particles remain disperse in the absence of M13 target (left), and aggregate in the presence of M13 target (right); **(b)** A 1µL drop of the reacted solution is deposited on a PDMS substrate. Unaggregated particles are transported to the drop edge by the Maranogni flow fields while large aggregates settle to the bottom and become concentrated in the centre of the drop; **(c)** The final residue pattern of a negative test shows little-to-no aggregates in the centre (left) while a positive test shows an accumulation of aggregates in the centre (right).

A previously described technique for visualizing cross-sectional flow fields in evaporating drops was used to characterize the motion of aggregates in the assay.[6] Optical coherence tomography (OCT) is a real-time, interferometry-based imaging modality in which objects are detected by measuring sample backscatter from a rastered source laser. With micrometer-scale axial and transverse resolution, millisecond temporal resolution, and a depth-of-field >1mm, OCT is well-suited to the geometric and time constraints of flow fields in evaporating sessile drops.[6,18,19] Figure 3 shows time-lapse composite images of an OCT scan through the diameter of a drop containing 100pM of target (a) and 0pM target (b). Each image represents 40s and is generated by overlaying 200 sequential frames captured at a rate of five frames per second. Particles appear as white objects, and flow fields are visualized by the particle tracks that are generated in the composite image. Particles that have reacted with target biomarker in Figure 3a are aggregated and therefore appear larger than the particles in Figure 3b that do not have biomarker present. In both Figures 3a and 3b, the flow fields are in the direction noted in Figure 1a and Figure 2b, i.e. toward the contact line along the drop surface and toward the drop centre along the substrate. This direction of motion is apparent in the time sequence videos included in Supporting Information. These videos and the composite images in Figure 3 show that the flow fields slow down throughout the evaporative process. This is because the drop solutions contain glycerol, which is a hygroscopic material. As water evaporates, the glycerol content steadily increases having the effect of slowing the evaporation rate which consequently mitigates the surface tension gradient driving the Marangoni flow. This time-dependent change in glycerol also causes a changing refractive index with time. As a result, the OCT images in Figure 3 contain a shadowing effect at the early time points which is reduced as evaporation progresses. Glycerol is included in the drop solution in order to address the problem of salt crystallization that occurs upon complete evaporation of drops containing a physiologic concentration of salt (0.9%). In preliminary experiments, it was determined that this salt crystallization disrupts particle deposition patterns. By including glycerol in the solution, drop

evaporation ceases once the water vapour has completely evaporated leaving behind a residual amount of glycerol that prevents salt crystallization.
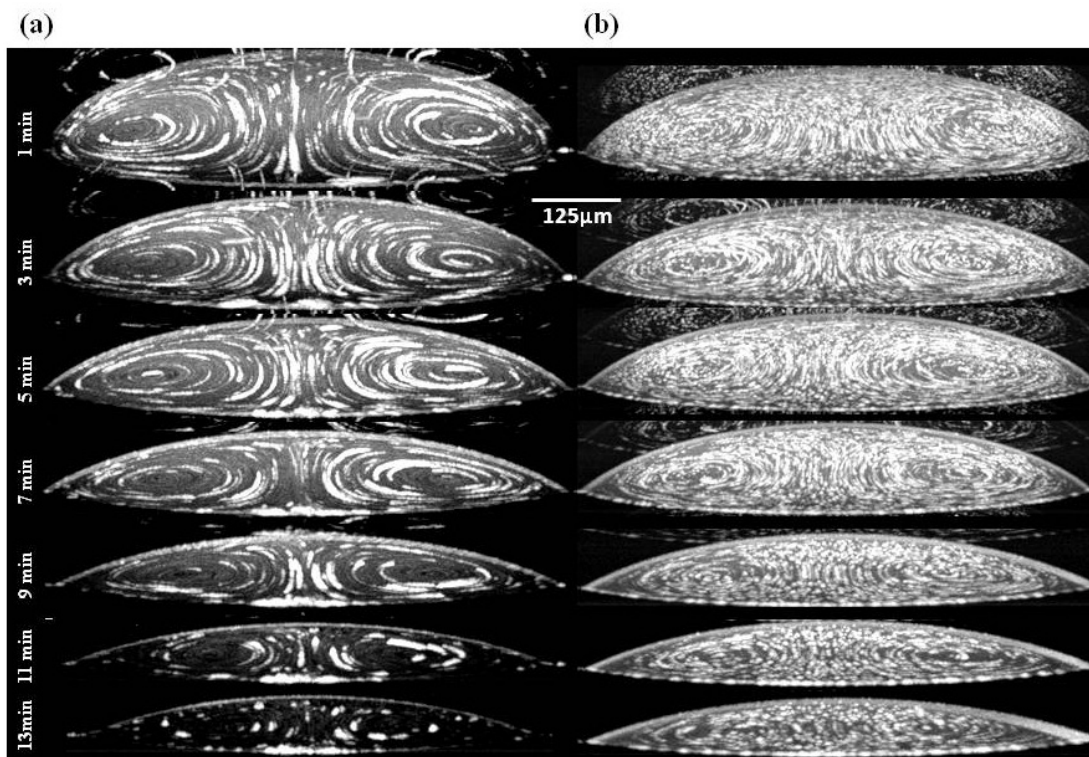
Figure 3. Time-lapse OCT composites taken through the diameter of an evaporating drop at seven different times during drop evaporation. The time sequence shows the accumulation of aggregates at the bottom centre of a drop containing 10^6 αM13-functionalized particles reacted with 100pM of M13 target (a) or 0pM M13 target (b). Each of the composite images consists of 200 consecutive OCT frames acquired at 5fps.

Importantly, Figure 3a shows that large aggregates settle to the PDMS substrate and are transported to the drop centre by the Marangoni eddy where the particle aggregates become increasingly concentrated with time. This phenomenon is even more apparent in the video sequences included in Supporting Information. Figure 3b, however, shows minimal aggregate accumulation at the centre because the particles remain mostly monodisperse in the absence of biomarker. In this case, particles continue to circulate in the Marangoni eddy. Some fraction of these particles becomes entrapped at the air-liquid interface due to surface tension effects and is

eventually deposited at the contact line as a result of the outwardly directed radial flow field. Other particles eventually settle along the substrate. Consequently, an evaporated drop of particle solution containing biomarker contains greater accumulation of particles at the centre than if no biomarker is present. The final deposition pattern of a 'positive' contains a large spot in the centre, which represents signal in the assay, and appears distinctively different than a 'negative'.
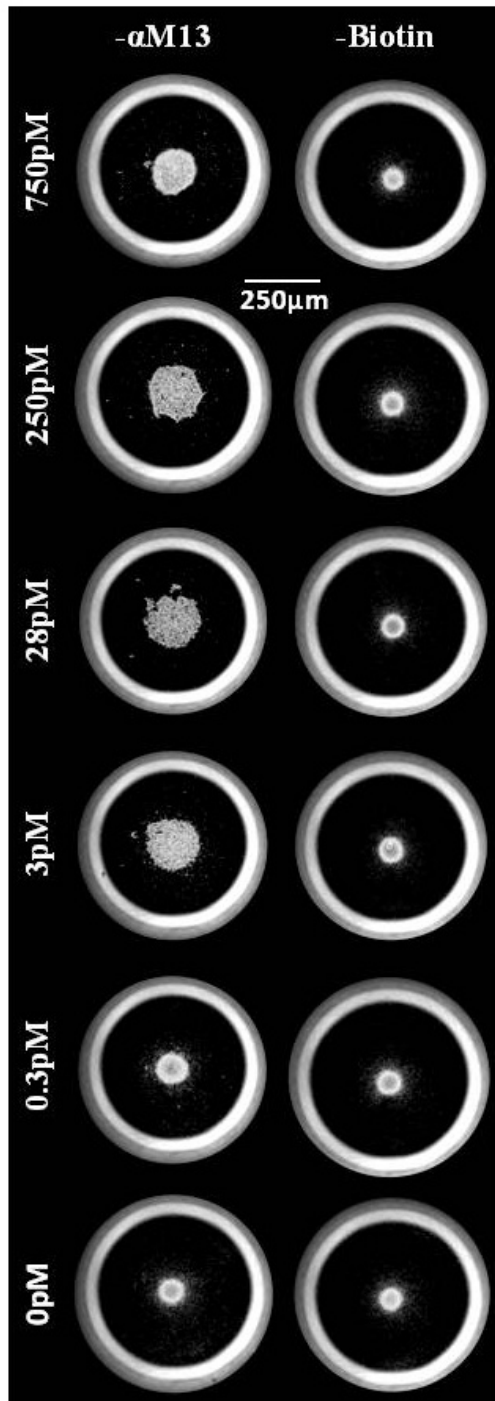
Figure 4. Change in particle deposition patterns produced by a decrease in M13 target concentration in 1μL drops containing 10^6 αM13 antibody-functionalized particles (left panel) evaporated on a PDMS substrate. The right panel is a negative control using biotin-coated particles. Signal in the assay is seen as a large spot in the centre of the drop at high concentrations of M13 target which decreases in size with less M13 target. The biotin control particles produce a signal similar in size to the 0pM sample at all M13 target concentrations.

Figure 4 shows phase contrast micrographs of these final deposition patterns at different biomarker concentrations. The patterns shown in the right panel are a negative control at each corresponding biomarker concentration using particles with a non-reactive surface. These particles are the same as the functionalized particles used in the left panel except surface-coated with biotin rather than αM13 antibody and therefore do not aggregate in the presence of biomarker. The images in Figure 4 show a general trend of increasing centre spot size with increasing biomarker concentration with the smallest centre spot occurring at 0pM of biomarker. The deposition patterns at 0pM biomarker appear essentially the same for the functionalized (left) and control (right). A small spot still appears at the 0pM concentration due to baseline aggregation that results from non-specific binding between particles. To quantify this aggregation, particle size distributions in the absence and presence of varying amounts of biomarker were optically measured with phase contrast microscopy (Supporting Information). This background noise could potentially be reduced in future designs by optimizing antibody conjugation techniques so as to maintain a monodisperse particle solution. Additionally, particle size and density parameters could be optimized to reduce this background noise.

Particles that do not aggregate are expected to accumulate at the drop edge. As a result, the ring structure should be larger in the 0pM sample and biotin controls compared to the −αM13 samples containing M13 target. However, it is not possible to verify this expected result based on the images in Figure 4 due to the refractive artefact that obscures the ring structure. This refractive artefact is caused by the residual glycerol and the underlying PDMS substrate. Since the particles are not fluorescent, but rather imaged under phase contrast light, it is difficult to characterize the final particle deposition patterns at the drop edge.

Signal in the assay was quantified by optically measuring the total area of aggregates in the centre of the drop as defined by a region of interest (ROI) that was 0.6x the mean diameter of the drops (578µm). This ROI size was chosen so as to exclude refractive artefact that occurs near the drop edge due to surface curvature of the fluid and refractive index of the residual glycerol.

Signal measurements were subsequently normalized by the drop diameter to adjust for volume variations. Sample drops at each biomarker concentration were deposited in triplicate and signal measurements for the triplicates were averaged. A sample size of five was used in the study for a total number of fifteen drops at each biomarker concentration. Signal-to-noise was then calculated by normalizing assay signal by the baseline signal that is generated in the absence of biomarker. These data are plotted against biomarker concentration in Figure 5a for both functionalized and control particles. The results show a concentration-dependent signal-to-noise for the functionalized particles that reaches a maximum value of 4.2 at approximately 28pM of biomarker. Signal-to-noise from the control particles remains statistically indistinguishable from the 0pM data point which indicates that particle aggregation in the assay is antibody-mediated. The signal-to-noise ratio of the antibody-functionalized particles decreases at greater concentrations of biomarker but remains more than three standard deviations above the zero at 750pM of biomarker.

Signal in the assay increases when aggregated particles are transported by Marangoni flow fields into the centre of the drop. With a fixed number of particles in solution, a greater biomarker concentration results in a greater mean aggregate size and a smaller fraction of unaggregated particles. However, this relationship reverses when available binding sites on the particles become saturated with biomarker. In this regime of biomarker concentration, aggregation is inhibited by the addition of biomarker because particles no longer compete for available binding sites making particle-particle cross-linking a less probable event. This previously described phenomenon, known as the Hook effect, is the reason why the signal-to-noise in Figure 5a has a parabolic shape with respect to biomarker concentration.[20,21] As a result, the dynamic range of the assay is limited to approximately four orders of magnitude in this proof-of-concept design. This limitation of the assay could potentially be improved in future designs by incorporating a range of antibody-to-particle ratios in the same particle solution. Preliminary data shows that this ratio significantly influences the size distribution of aggregated particles in a

titration with biomarker (Supporting Information). Additionally, the dynamic range of the proposed assay could be improved by evaporating an array of drops whereby the particle solution used in each drop has either a different antibody:particle ratio, or a fixed antibody:particle ratio with a different number of total particles.
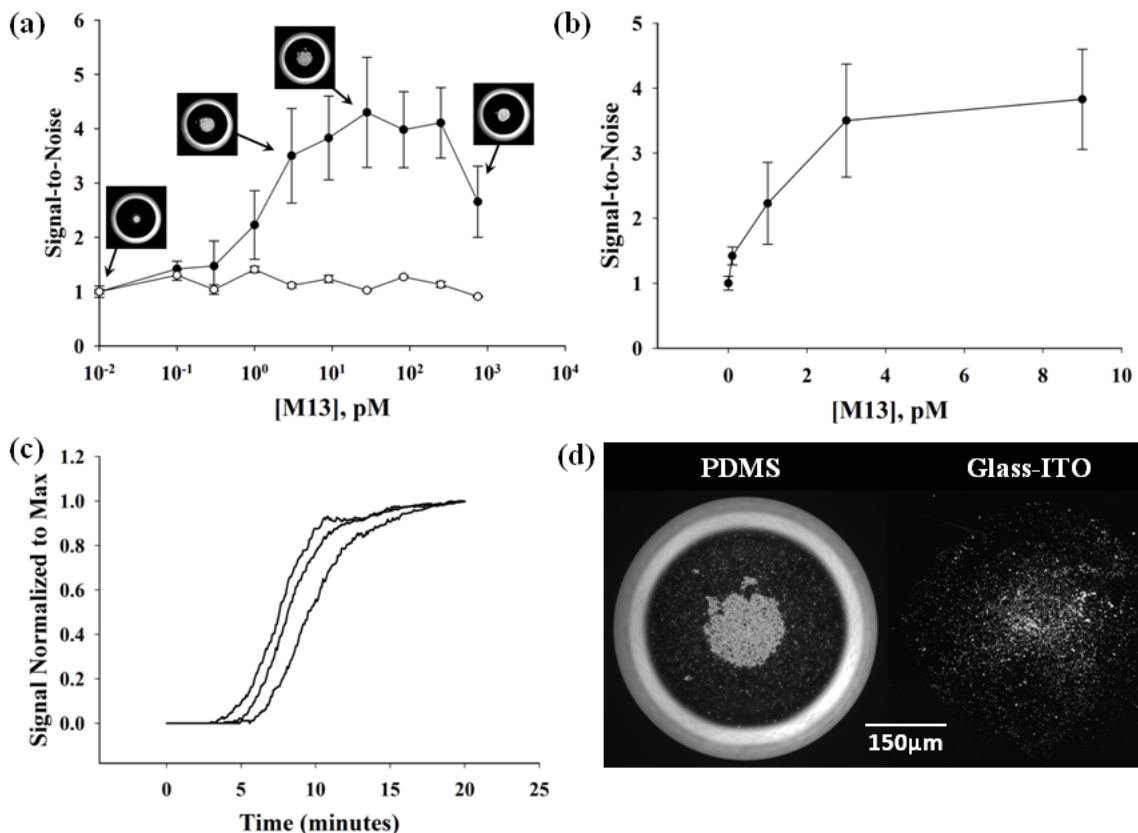
Figure 5. (a) Signal was measured as a function of M13 target concentration by measuring the area of aggregates in the centre of the drop using a predefined region of interest having a diameter = 0.6 times the mean drop diameter. Signal was normalized for drop volume and divided by the mean 0pM value to generate a signal-to-noise ratio. Mean values for all M13 target concentrations are plotted (log-linear) for n=15 +/- 1σ. (b) Signal-to-noise at the low M13 target concentrations are plotted (linear) for n=15 +/- 1σ. (c) Signal-to-noise, normalized to the maximum value for each of three drops containing 28pM of M13 target evaporated on a PDMS substrate, is plotted as a function of drop evaporation time. (d) Images of particle residue patterns produced by evaporating a drop of αM13-functionalized particles containing 28pM of M13 target on a PDMS substrate (left) versus a glass substrate coated with indium tin oxide (ITO, right).

The lower end of the signal-to-noise data from Figure 5a is re-plotted in a linear-linear format in Figure 5b. The limit of detection of the assay was determined by applying a second order curve fit to these data and calculating the lowest biomarker concentration at which signal-to-noise remains at least three standard deviations above the signal at 0pM of biomarker. This approach indicates a limit of detection of 96fM. Other methods of signal measurement, including total pixel intensity, number of objects, and mean object diameter, were also evaluated and found not to be as responsive to M13 target concentration as total aggregate area (data not shown).

Signal generation in the assay increases with time. As shown in Figure 5c, Marangoni flow fields begin transporting settled aggregates to the centre of the drop upon deposition on the PDMS substrate. These Marangoni flows persist until the evaporation-induced surface tension gradient along the surface of the drop is mitigated as a result of increasing concentration of residual glycerol. As a result, signal-to-noise in the assay increases throughout drop evaporation and is quantitatively shown in Figure 4c for three different drops. Signal-to-noise plotted against time shows an initial rise followed by a plateau. The rise is caused by the contribution of two different sources of signal: (1) transportation of aggregates to the centre that have already settled on the substrate, and (2) aggregates circulating in the Marangoni eddy that settle to the substrate at the drop centre. The subsequent plateau in these data is due to the diminished flow fields that occur later in the evaporation process. There is a slight dip in the signal after the initial rise for two of the data series, most likely due to the aggregates becoming increasingly concentrated and stacked at the drop centre. A time sequence of phase contrast images provided in Supporting Information shows particle aggregates migrating to the centre and the corresponding signal-to-noise as a function of time. The signal-to-noise reaches approximately 80% of maximum within 10 minutes of evaporation. It should be noted that 1μL drop volumes were used in this study. Since the hydrodynamics scale with drop volume, the time constant of the assay could potentially be lowered by decreasing the drop volume. The trade-off would be detectability of the signal in the assay. At the 1μL volume, the spot of aggregates that forms in the centre of the assay is

101

visually detectable. However, phase contrast microscopy was used in this study for more precise signal measurement. A likely implementation of the design would rely on a smart phone to capture an image of the evaporated drop and use a locally-stored image processing app to interpret, quantify, transmit, and store the test result.

The substrate on which the sample drop is evaporated is an important design parameter. Ristenpart et al have modelled that the presence and direction of Marangoni flow is dependent on the ratio of thermal conductivities of the substrate and drop fluid.[16] A drop of fluid placed on a substrate with sufficiently low thermal conductivity results in a temperature and surface tension gradient that promotes fluid flow along the drop surface directed toward the drop edge. Conversely, a high thermally conductive substrate causes flow in the reverse direction. Therefore, a substrate with sufficiently low thermal conductivity, like PDMS, is required to promote the Marangoni flow in the direction that concentrates biomarker-induced, aggregated particles at the drop centre for detection. According to this theory, a substrate with sufficiently high thermal conductivity produces these flow fields in the opposite direction and therefore will not generate signal in the assay. For example, Figure 5d shows the deposition patterns produced when a drop containing 28pM of biomarker is evaporated on a PDMS substrate versus an indium tin oxide (ITO)-coated glass slide. The ITO-coated slide has a thermal conductivity of approximately 3.95 W/mK, significantly greater than PDMS and sufficiently thermally conductive to generate the reverse flow condition according to Ristenpart et al.[22] Indeed, the final deposition pattern shown in Figure 5d is more evenly spread-out along the substrate than that which results on PDMS. However, time composite OCT images of the flow fields that occur in a drop evaporating on an ITO-coated glass slide still show Marangoni flow in the same direction as what is produced on a PDMS substrate (Supporting Information). The Marangoni flow fields on the ITO slide occur at a much slower rate than PDMS, which explains the greater concentration of aggregated particles at the drop centre on PDMS versus ITO. However, the reasons for this departure from the Marangoni flow conditions predicted by Ristenpart et al are not entirely

102

understood. Preliminary data show that a drop of particle solution in water evaporated on an ITO-coated slide does not produce Marangoni flow, but a drop of the same particle solution containing glycerol does produce Marangoni flow. In fact, the same observation was made for a PDMS substrate (Supporting Information) and on a regular glass slide to a lesser degree. The addition of glycerol to an aqueous solution may produce density and viscosity gradients in the evaporating drop that promote Marangoni flow in ways not well understood.

As previously described, Marangoni flow in an evaporating drop refers to eddy currents that result from a surface tension gradient at the air-liquid interface.[3,4,8,23,24] Deegan first postulated that the non-uniform evaporative flux across the surface of a drop necessarily leads to a corresponding temperature and surface tension gradient.[3,4] This surface tension gradient, which is radially symmetric, causes fluid to flow from regions of low surface tension to high surface tension. Fluid transport across these temperature and surface gradients results in a cross-sectional eddy current having toroidal geometry when viewing the drop from above. While this Marangoni flow is prevalent in organic solvents, previous studies have shown that it occurs minimally in aqueous drops because the surface tension of an air-water interface is easily affected by the presence of trace exogenous materials.[24] There have been conflicting reports about the effect of surfactants on Marangoni flow in evaporating drops. One study has shown the presence of surfactants to mitigate the surface tension gradient and prevent Marangoni flow.[25] Another group has shown a different type of surfactant molecule to promote Marangoni flow.[26] Drops in this study contain small amounts of the surfactant Tween 20, which may also contribute to the observed flow patterns.

Hu et al have shown through a numerical simulation that the presence of Marangoni flow is dependent on the drop contact angle, which changes with evaporation time.[8] They estimate that the surface tension-induced eddy currents cease at contact angles below ~14°. This is because the thermal conduction path to the isothermal substrate, which is the primary heat source, becomes sufficiently small at the drop centre, and evaporative cooling at the edge is sufficiently

large to eliminate the temperature and surface tension gradients at the drop surface.

Physical and chemical properties of an evaporating drop, like contact angle, non-uniform evaporation rates, and material concentrations, are dynamic and interdependent. Chemical, density, viscosity, temperature, density, and surface tension gradients change with evaporation time and likely affect Marangoni flow fields in ways that are not well understood. These phenomena are the focus of on-going studies.

The design parameters used in this initial biosensor design were chosen to demonstrate proof-of-concept for a low resource point-of-care assay. Several system variables could be optimized for specific future applications. Since the design uses an antibody as the biorecognition element, the assay could be adapted to many different disease types. The biosensor could generate a colorimetric signal by incorporating dyed or fluorescent particles. Assay limit of detection and dynamic range may be tuned by optimizing particle size, concentration, and density for a given disease application. Finally, the effects of glycerol and surfactant concentrations have not yet been fully elucidated and may be further modified to improve overall biosensor performance. The biosensor investigated in this study has the advantage of using a polydimethylsiloxane (PDMS) substrate, which is commonly used in microfluidics.[27] Therefore this design could potentially be integrated with existing PDMS-based microfluidic architectures, for example droplet-based microfluidic devices. These devices use electrowetting techniques to manipulate the motion and processing of drops on a PDMS surface.[28,29] The approach presented here could potentially be integrated with such technology to provide an optically detectable, multiplexed, and quantifiable test read-out strategy.

Conclusions

This work demonstrates the utility of a biosensor design that relies on the hydrodynamics of an evaporating drop to generate an optically detectable test result. This proof-of-concept study shows that antibody-functionalized particles aggregate in the presence of biomarker and when a drop of this solution is evaporated on a PDMS substrate, Marangoni flows concentrate the aggregates at the centre of the drop. The substrate material and solution conditions are important design parameters that affect the dynamics of the evaporation-induced flow fields and the extent to which aggregated particles become concentrated in the drop. Signal in the assay is based on the spatial distribution of particle depositions upon drop evaporation. Using standard microscopy to measure the test result, a femtomolar limit of detection is achievable. Future designs may incorporate a camera phone for signal measurement and interpretation, which would be more amenable to a point-of-care diagnostic useful in a low resource setting.
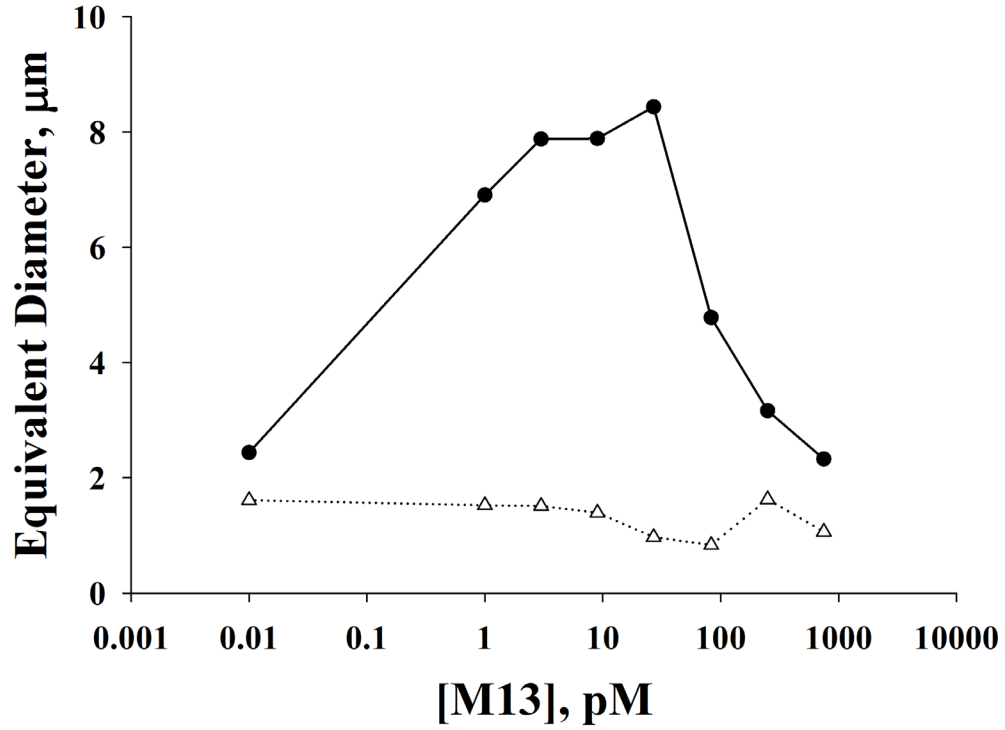
Figure S1. **Neutravidin-coated polystyrene particles (1μm diameter, Invitrogen P/N F8775) were surface-functionalized with αM13 antibody and reacted with the M13 target at varying concentrations. Resulting aggregated particles were sized using phase contrast microscopy. Mean equivalent diameter is plotted against M13 target concentration in a log-linear format.**
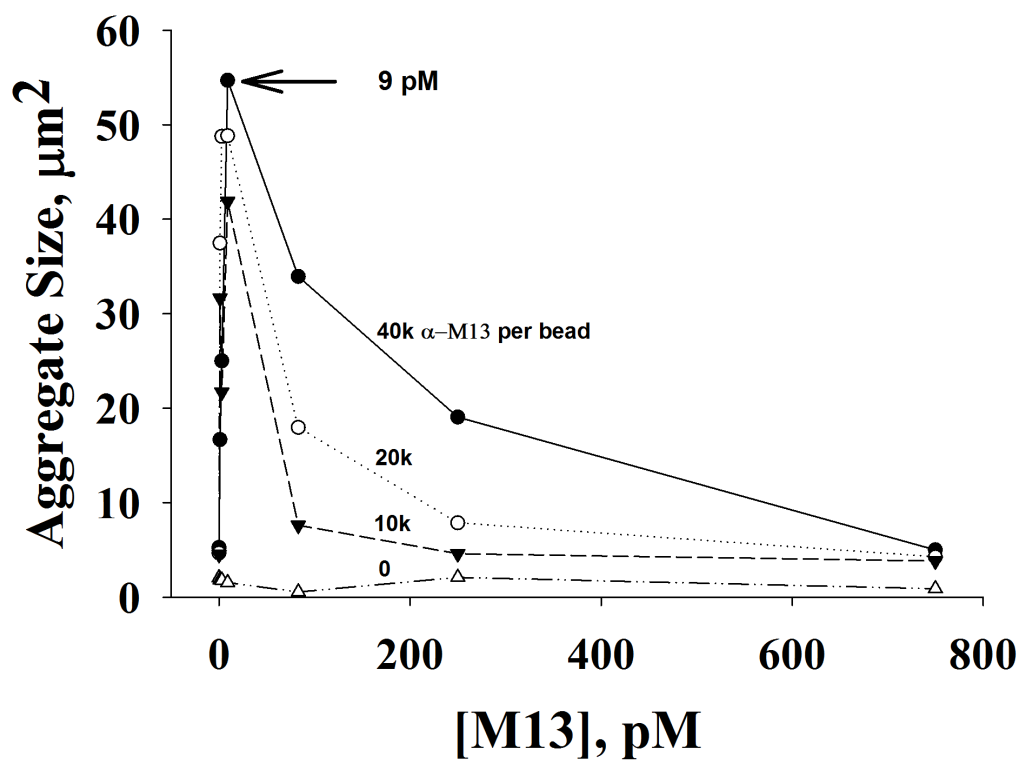
Figure S2. Neutravidin-coated polystyrene particles (1µm diameter, Invitrogen P/N F8775) were surface-functionalized with αM13 antibody at varying antibody:bead ratios and reacted with the M13 target at varying concentrations. Resulting aggregated particles were sized using phase contrast microscopy. Mean aggregate area is plotted against M13 target concentration in a linear-linear format.
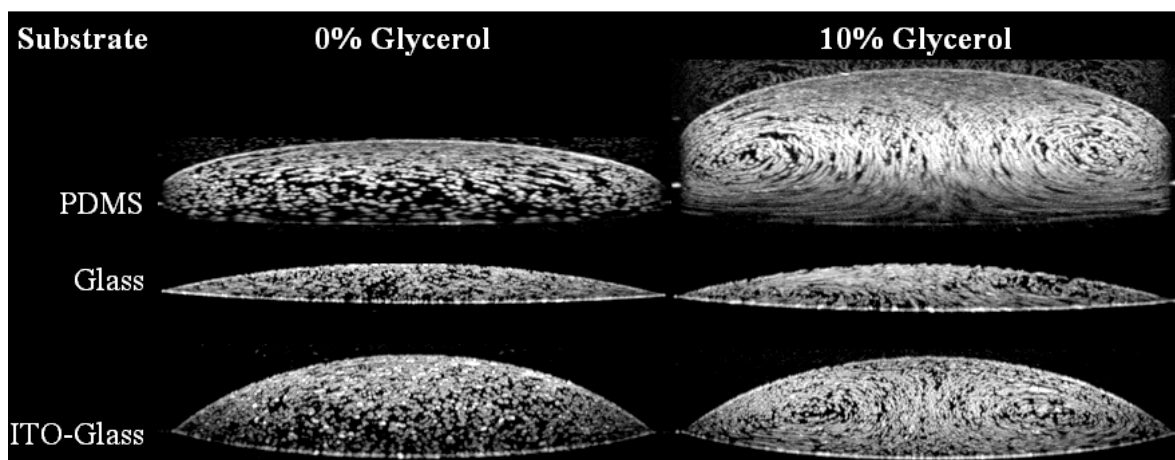
Figure S3. The effects of glycerol and substrate composition on Marangoni flow were evaluated by depositing 1μL drops of particle solutions containing 10^6 polystyrene particles (1m diameter, carboxylated, Bangs Laboratories, Inc) on PDMS, glass, and an indium-tin oxide (ITO)-coated slide. Cross-sectional flow patterns were imaged with OCT thought the diameter of the drop following a previously described protocol. Each time-lapse composite image consists of 200 consecutive OCT frames acquired at 5fps.
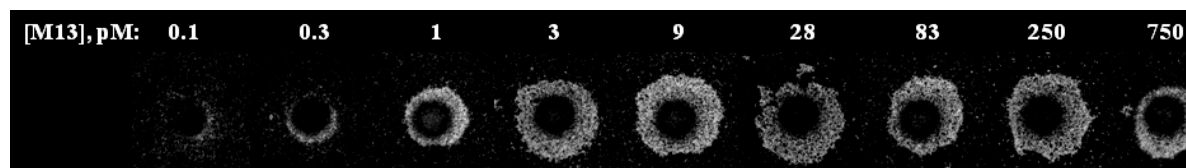
Figure S4. Signal generated from varying amounts of M13 target as seen through a mask that subtracts the background noise from the signal. Background noise is the amount of particles that accumulate in the center of the drop in the absence of target.
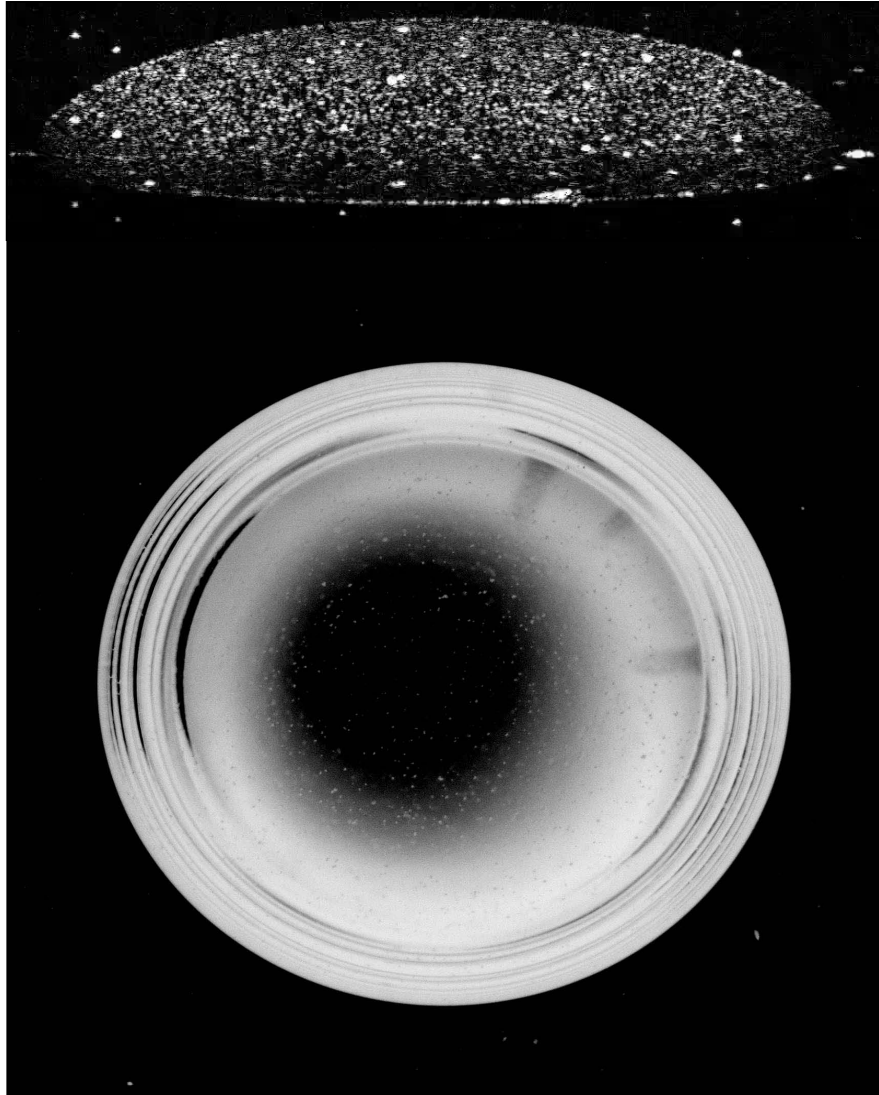
Video 1. A series of concatenated sequences taken with OCT through the diameter of a 1μL drop evaporated on PDMS shows reverse Marangoni flow patterns from the cross-sectional viewpoint (top). The drop contains 100pM M13K07 bacteriophage and 10^6, 1μm-diameter particles surface functionalized with anti-M13 monoclonal antibody. Flow patterns from the top-down viewpoint under identical experimental conditions are shown using phase contrast microscopy (bottom). Aggregated particles are shown to accumulate in the center of the drop from both viewpoints.

109
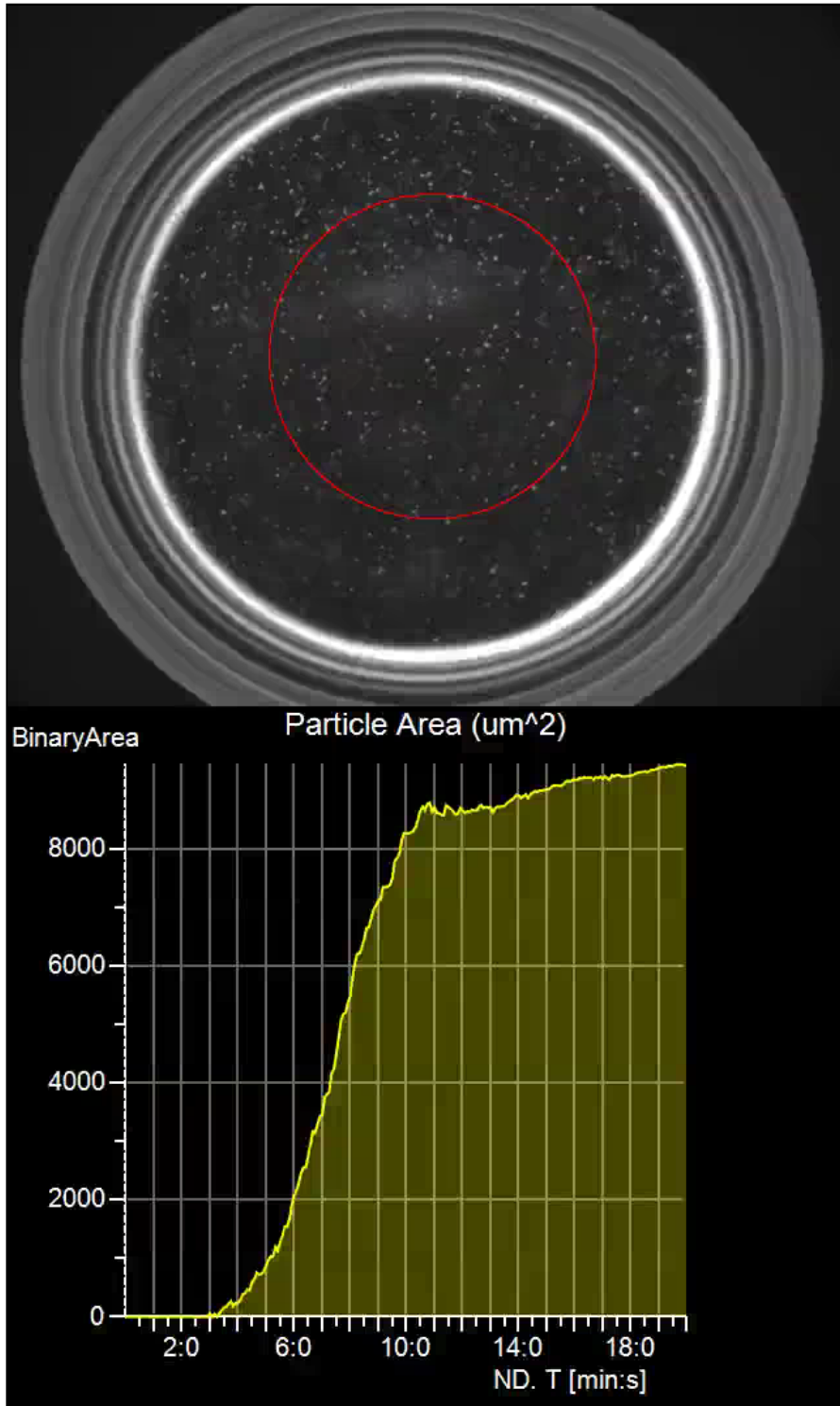
Video 2. A sequence taken with phase contrast microscopy of a 1μL drop evaporated on PDMS shows the development of signal as a function of time in a pre-defined region of interest (red circle). Signal is measured as the accumulation of particle area. The drop contains 100pM M13K07 bacteriophage and 10^6, 1μm-diameter particles surface functionalized with anti-M13 monoclonal antibody.

References

(1) Yager, P.; Domingo, G. J.; Gerdes, J.: Point-of-care diagnostics for global health. *Annu Rev Biomed Eng* **2008**, *10*, 107-44.

(2) Yager, P.; Edwards, T.; Fu, E.; Helton, K.; Nelson, K.; Tam, M. R.; Weigl, B. H.: Microfluidic diagnostic technologies for global public health. *Nature* **2006**, *442*, 412-418.

(3) Deegan, R. D.: Pattern formation in drying drops. *Physical Review E* **2000**, *61*, 475-485.

(4) Deegan, R. D.; Bakajin, O.; Dupont, T. F.; Huber, G.; Nagel, S. R.; Witten, T. A.: Contact line deposits in an evaporating drop. *Physical Review E* **2000**, *62*, 756-765.

(5) Deegan, R. D.; Bakajin, O.; Dupont, T. F.; Huber, G.; Nagel, S. R.; Witten, T. A.: Capillary flow as the cause of ring stains from dried liquid drops. *Nature* **1997**, *389*, 827-829.

(6) Trantum, J. R.; Eagleton, Z. E.; Patil, C. A.; Tucker-Schwartz, J. M.; Baglia, M. L.; Skala, M. C.; Haselton, F. R.: Cross-sectional tracking of particle motion in evaporating drops: flow fields and interfacial accumulation. *Langmuir* **2013**, *29*, 6221-31.

(7) Hu, H.; Larson, R. G.: Analysis of the microfluid flow in an evaporating sessile droplet. *Langmuir* **2005**, *21*, 3963-3971.

(8) Hu, H.; Larson, R. G.: Analysis of the effects of Marangoni stresses on the microflow in an evaporating sessile droplet. *Langmuir* **2005**, *21*, 3972-3980.

(9) Harris, M. T.; Widjaja, E.: Particle deposition study during sessile drop evaporation. *Aiche Journal* **2008**, *54*, 2250-2260.

(10) Wong, T. S.; Chen, T. H.; Shen, X. Y.; Ho, C. M.: Nanochromatography Driven by the Coffee Ring Effect. *Analytical Chemistry* **2011**, *83*, 1871-1873.

(11) Tarasevich, Y. Y.; Pravoslavnova, D. M.: Segregation in desiccated sessile drops of biological fluids. *European Physical Journal E* **2007**, *22*, 311-314.

(12) Tarasevich, Y. Y.; Pravoslavnova, D. M.: Drying of a multicomponent solution drop on a solid substrate: Qualitative analysis. *Technical Physics* **2007**, *52*, 159-163.

(13) Brutin, D.; Sobac, B.; Loquet, B.; Sampol, J.: Pattern formation in drying drops of blood. *Journal of Fluid Mechanics* **2011**, *667*, 85-95.

(14) Teste, B.; Ali-Cherif, A.; Viovy, J. L.; Malaquin, L.: A low cost and high throughput magnetic bead-based immuno-agglutination assay in confined droplets. *Lab Chip* **2013**, *13*, 2344-9.

(15) Trantum, J. R.; Wright, D. W.; Haselton, F. R.: Biomarker-Mediated Disruption of Coffee-Ring Formation as a Low Resource Diagnostic Indicator. *Langmuir* **2012**, *28*, 2187-2193.

(16) Ristenpart, W. D.; Kim, P. G.; Domingues, C.; Wan, J.; Stone, H. A.: Influence of substrate conductivity on circulation reversal in evaporating drops. *Physical Review Letters* **2007**, *99*.

(17) Eiermann, K.: Thermal conductivity of plastics in relation to structure, temperature and previous history. *Kunststoffe* **1961**, *51*, 512-517.

(18) Manukyan, S.; Sauer, H. M.; Roisman, I. V.; Baldwin, K. A.; Fairhurst, D. J.; Liang, H. D.; Venzmer, J.; Tropea, C.: Imaging internal flows in a drying sessile polymer dispersion drop using Spectral Radar Optical Coherence Tomography (SR-OCT). *Journal of Colloid and Interface Science* **2013**, *395*, 287-293.

(19) Drexler, W.: Ultrahigh-resolution optical coherence tomography. *Journal of Biomedical Optics* **2004**, *9*, 47-74.

(20) Fernando, S. A.; Sportsman, J. R.; Wilson, G. S.: Studies of the low dose 'hook' effect in a competitive homogeneous immunoassay. *Journal of immunological methods* **1992**, *151*, 27-46.

(21) Fernando, S. A.; Wilson, G. S.: Studies of the 'hook' effect in the one-step sandwich immunoassay. *Journal of immunological methods* **1992**, *151*, 47-66.

(22) Ashida, T.; Miyamura, A.; Oka, N.; Sato, Y.; Yagi, T.; Taketoshi, N.; Baba, T.; Shigesato, Y.: Thermal transport properties of polycrystalline tin-doped indium oxide films. *J Appl Phys* **2009**, *105*.

(23) Barash, L. Y.; Bigioni, T. P.; Vinokur, V. M.; Shchur, L. N.: Evaporation and fluid dynamics of a sessile drop of capillary size. *Physical Review E* **2009**, *79*.

(24) Hu, H.; Larson, R. G.: Marangoni effect reverses coffee-ring depositions. *Journal of Physical Chemistry B* **2006**, *110*, 7090-7094.

(25) Savino, R.; Paterna, D.; Favaloro, N.: Buoyancy and Marangoni effects in an evaporating drop. *Journal of Thermophysics and Heat Transfer* **2002**, *16*, 562-574.

(26) Still, T.; Yunker, P. J.; Yodh, A. G.: Surfactant-Induced Marangoni Eddies Alter the Coffee-Rings of Evaporating Colloidal Drops. *Langmuir* **2012**, *28*, 4984-4988.

(27) Folch, A.; Ayon, A.; Hurtado, O.; Schmidt, M. A.; Toner, M.: Molding of deep polydimethylsiloxane microstructures for microfluidics and biological applications. *J Biomech Eng-T Asme* **1999**, *121*, 28-34.

(28) Teh, S. Y.; Lin, R.; Hung, L. H.; Lee, A. P.: Droplet microfluidics. *Lab on a Chip* **2008**, *8*, 198-220.

(29) Cho, S. K.; Moon, H. J.; Kim, C. J.: Creating, transporting, cutting, and merging liquid droplets by electrowetting-based actuation for digital microfluidic circuits. *J Microelectromech S* **2003**, *12*, 70-80.

CHAPTER VI

CONCLUSIONS AND FUTURE DIRECTIONS

This dissertation comprises three manuscripts, which collectively establish a framework for designing a diagnostic assay based on the hydrodynamics of an evaporating drop. An initial design was evaluated using three particles and a Ni(II)NTA biointerface to generate a colorimetric pattern for distinguishing a positive from a negative test. This assay achieved a 200nM limit of detection in a water sample containing poly-l-histidine, a biomolecular mimic of the malaria biomarker, *pf*HRPII. This design was shown to have several disadvantages: (1) it requires precise alignment of the drop over a magnetic field, (2) a relatively high limit of detection, and (3) an inability to function properly in the presence of proteins and salts, which influence the motion of particles. To further investigate this latter observation, optical coherence tomography was used to characterize the cross-sectional flow patterns of different particle types in real-time under different conditions. The vertical distribution of particles was found to be influenced by relative humidity and particle density, which in turn affects the time at which particles reach the contact line. It was also observed that both the substrate and the presence of certain additives in solution, for example glycerol, promote eddy currents. These observations were used to revise the initial assay design by incorporating glycerol in solution and rely on eddy currents rather than the coffee ring effect for signal generation in the assay. Glycerol in the revised assay has a dual function: (1) as a hygroscopic material it prevents complete drop evaporation and therefore circumvents the salt crystallization phase that disrupts deposition patterns; and (2) it promotes the eddy currents responsible for developing signal in the revised assay. Antibodies were used as the biointerface in the revised assay to demonstrate potential applicability to a broad set of diseases. A limit of detection of 96fM was achieved using the M13K07 bacteriophage as a model system. This revised assay also has the advantage of not

requiring alignment over a magnetic field. Moreover, the assay was tested using solutions containing proteins and physiologic levels of salt thereby demonstrating potential for use in more complex biological samples.

Future studies should focus on investigating the effect of system variables on assay performance and evaluate the assay for detecting actual biomarkers in biological samples. Variables that should be considered for optimization include particle size, particle density, particle concentration, and glycerol and surfactant concentrations. One method for investigating particle size and density effects is to synthesize gold-coated polystyrene particles using different gold shell thicknesses. The thickness of the gold shell can be tuned during synthesis, which provides a means to investigate the effects of particle density. Additionally, the assay should be adapted for use in malaria testing by evaluating both Ni(II)NTA and antibody biointerfaces.

Other design considerations for future studies include integrating the assay with sample preparation and purification processes to improve overall performance. Also, the assay format may be adapted to an array of nanoliter drops that facilitates a multiplexing capability as well as reduce the overall test time while improving the visual detectability of the signal. One possible format might use a paper-based substrate pattern printed with hydrophobic and hydrophilic regions and particle reagents. This type of arrayed format would enable a single step process in which drops are automatically formed on the paper substrate in predetermined locations upon application of the biological sample to the paper substrate. Alternatively, an arrayed format may be integrated with a microfluidic device that includes pre-processing steps to improve overall assay performance.

An alternative drop-based design, briefly considered during this project, should be evaluated for feasibility. The design relies on cross-linking a label to large particles in the presence of biomarker, and these large particles then accumulate in the center of the drop due to surface tension interactions with the air-liquid interface (Appendix A). This design idea was preliminarily evaluated with OCT imaging. This biosensor design has the potential to work well

with biological fluids because development of signal relies not on colloidal interactions but rather surface-tension induced mass transport.

APPENDIX A

CENTER ACCUMULATION OF LARGE BEADS IN AN EVAPORATING DROP DUE TO
SURFACE TENSION FORCE FROM THE AIR-LIQUID INTERFACE

An alternate drop-based diagnostic design is based on the phenomena first described by Weon et al in which the descending air-water interface in an evaporating drop interacts with large particles in solution that are resting on the substrate.[1] The interface exerts a surface tension force on the particles that is directed toward the center of the drop causing the particles to migrate toward the center. This phenomenon could potentially be used as the basis for a diagnostic assay.

One implementation of this idea would incorporate a second, small (e.g. 1μm diameter) color-dyed particle in the drop in addition to a large bead (e.g. 50μm diameter), both of which are surface functionalized bind the target biomarker. If the biomarker is present, then the two particles are cross-linked and the small colored particle is pulled to the center of the drop producing a visually detectable signal. In the absence of biomarker, the colored bead is transported to the edge by the coffee ring effect producing a colored ring. A third, differently colored particle would also be solution to ensure the contact line is pinned in the presence or absence of biomarker. Alternatively, another implementation may incorporate a functionalized substrate that binds the large particle in the presence of biomarker preventing it from migrating to the drop center during drop evaporation.
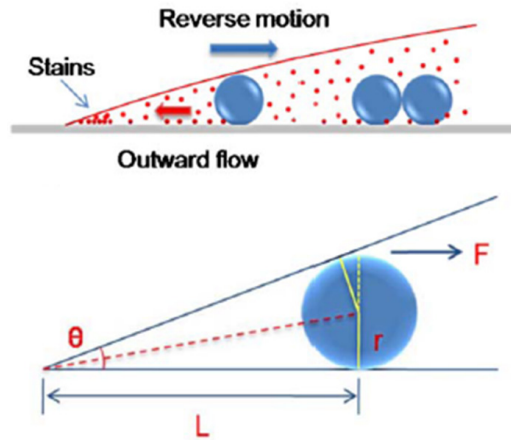
Figure 1. Forces on a particle interacting with the air-water interface.
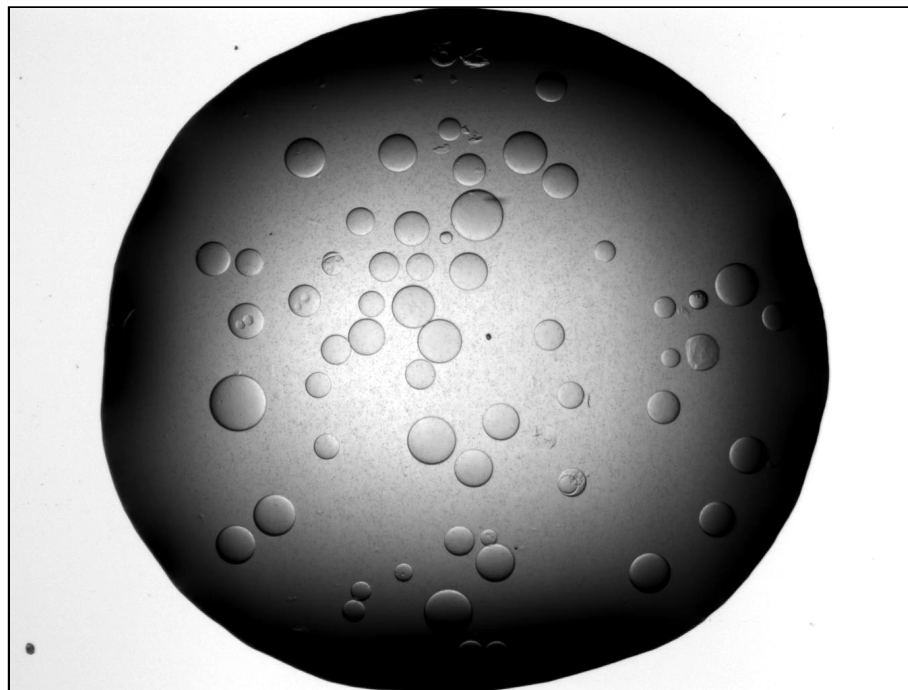
Video 1. A 1μL drop of water containing polydisperse Sepharose beads with a mean diameter of 80μm.
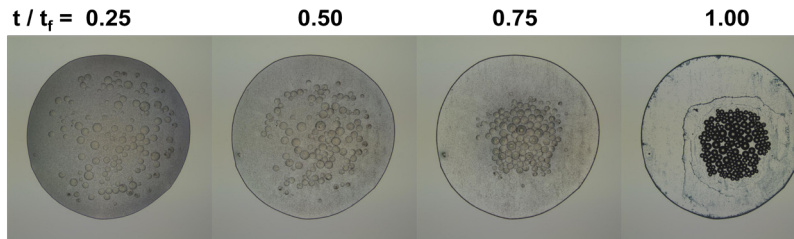
Figure 2. **Time lapse images with phase contrast microscopy of a 1µL drop of water containing polydisperse Sepharose beads with a mean diameter of 80µm and 10^6 1µm carboxylated polystyrene particles.**
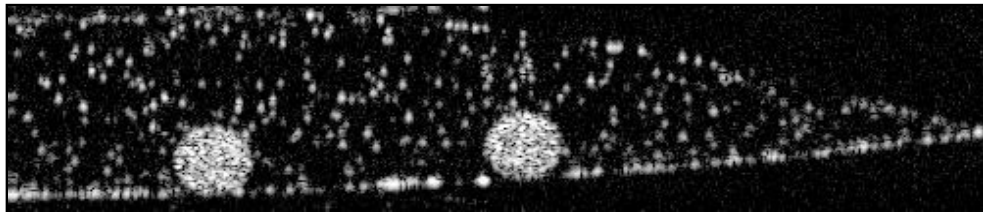
Video 2. **Cross-sectional sequence taken with OCT through the diameter of a 1µL drop containing polydisperse Sepharose beads with a mean diameter of 80µm and 10^6 1µm carboxylated polystyrene particles.**

References

(1)   Weon, B. M.; Je, J. H.: Capillary force repels coffee-ring effect. *Physical Review E* **2010**, *82*.

APPENDIX B

CROSS REFERENCE TABLE FOR LABORATORY NOTEBOOKS

Laboratory notebooks are numbered 1-6 on the spine. Notebook #'s 4 and 5 are three-ring binders and do not have numbered pages. Related data and notes from each experiment are stored electronically in a corresponding folder named according to date (e.g. "13_May 23").

Experiment	Date	Book #	Pg #'s
Establish relationship between degree of non-specific binding and key solution variables: salt & pH	4/13/2010	2	1-2
Characterize ring formation as function of time	4/14/2010	2	3-4
Evaluate anti-M13 functionalized particles in ring assay	4/18/2010	2	7-18
Demonstrate M13 capture with antiM13 functionalized bead	4/23/2010	2	25-28
Repeat 4/23 experiment with higher [tween] nad 10mM phosphate buffer	4/26/2010	2	29-31
SMCC-coupling of antiM13 to FeOx-PEG-NH2	6/3/2010	2	43-46
SMCC-coupling of antiM13 to PS beads	6/8/2010	2	47-50
Ring assay with anti-M13 beads	6/11/2010	2	51-54
Repeat coupling to 250nm FeOx beads	6/14/2010	2	55-58

Conversion of PS-COOH to -NH2 via ethylenediamine	6/18/2010	2	59-61
Coupling of antiM13 to FeOx-PEG-NH2 using one-step EDC method and ring assays to confirm	6/21/2010	2	62-65
Aggregation assay to verify successful conjugation from 6/21/2010	6/23/2010	2	66-67
Conversion of PS-COOH (Bangs Labs) to -NH2 via ethylenediamine and verification	7/7/2010	2	68-69
Couple PEG-MAL (SM(PEG)$_4$) to PS-NH2 beads and then conjugate reduced antiM13 to MAL group.	7/8/2010	2	70-71
Verify PS-PEG-antiM13 successful from 7/8/2010	7/12/2010	2	72-74
Verify antiM13 present on PS-PEG-antiM13 using anti-mouse secondary (AF555)	7/14/2010	2	75-76
Coupling of antiM13 to PS-proteinG beads	7/15/2010	2	77
2-particle assay using FeOx-PEG-antiM13 (6/22/2010) and PS-PEG-antiM13 (7/8/2010) plus M13	7/16/2010	2	78-80
Characterize non-specific interactions from 7/16/2010 assay	7/20/2010	2	81-83, 88-89

Couple antiM13 to PS-COOH (Bangs Labs), PS-NH2 (Spherotech), FEOx-PEG-NH2 (Micromod), and FeOx-COOH (Micromod) using one-step EDC coupling	7/22/2010	2	85
Aggregation assay with M13 using beads from 7/22/2010 conjugation experiment	7/29/2010	2	90-94
Compare functionalized particles with different surface chemistries with respect to M13 capture/aggregation	8/5/2010	2	98
Couple antiM13 to PS-COOH (green, Bangs Labs) and anti-4F2 to PS-COOH (red, Bangs Labs)	8/6/2010	2	99
Evaluate aggregate formation (antibody-antigen binding) as function of solution ionic strength using FeOx-COOH-antiM13 particles (coupled 7/22/2010)	8/9/2010	2	100
Evaluate Sigmacote silicone coating on glass slide for effect on PS-antiM13 non-specific binding to glass (particles settling inside the ring)	8/10/2010	2	101
Evaluate PS-COOH-antiM13 (coupled 8/5/2010) ring fomration on different slide chemistries: reg glass, amine-terminated, pegylated	8/11/2010	2	102
Conjugate biotinylated antiM13 to Dynal-streptavidin beads	8/12/2010	2	104-106
2-particle proof-of-concept using streptavidin-biotin conjugated particles	8/13/2010	2	107
Evaluate effect of BSA block and reduced ionic strength on 2-particle assay	8/16/2010	2	108-117

Couple antiM13 to Dynal and PS beads following 8/12/2010 protocol	8/18/2010	2	118-120
Evaluate degree of baseline aggregation of individual particles and particles together incubated with varying amounts of PLH	8/23/2010	2	122-123
Evaluate FeOx-NiNTA +PS-NiNTA aggregation response to varying amounts of [PLH] using lower []'s than Aug 23rd experiment	8/24/2010	2	124-125
6xHis peptide synthesis	8/26/2010	2	128-129
Determine if reason for Si-M-NiNTA and PS-NiNTA particles flocculating and falling out of soltuion when mixed together is due to lack of charge (Ni) on one or both of the particles.	9/4/2010	2	130-137
Using flow cytometry, characterize bead-bead interactions in presence of TAMRA-BNT2	9/15/2010	2	138-139
Repeat 8/24/2010 experiment (again using 250nm FeOx-NiNTA) but this time incorporating a control bead to see if @10uM PLH the control bead forms a ring with different color than (-)	9/16/2010	2	139
Using 96-well plate, evaluate 3-particle assay for ring change (with and without magnet) varying [PLH] across columns and [FeOx-NiNTA] down rows	9/23/2010	2	141-153
Characterize the limit of detection of the 3-particle assay	10/15/2010	2	154-156
Thoughts on alternate drop diagnostic designs	10/18/2010	2	157-158

Prove PLH does not displace FITC-labeled 6xHistidine pre-conjugated on surface of 1um PS-NiNTA particles	10/27/2010	2	160-162
Determine target type (PLH vs BNTII) and [target] to be used for remaining proof-of-concept studies	11/13/2010	2	163
Determine if reason for no signal at 4uM [target, binding sites] is due to ratioj of target vs particle binding sites	11/14/2010	2	164-165
Detemine if order-of-addition is reason for alck of signal at low [PLH]	11/15/2010	2	166
Determine optimal particle concentrations	11/19/2010	2	167-168
Determine limit of detection of 3-particle assay	11/24/2010	2	169-170
Methods used for functionalizing particle-Ni(II)NTA	1/7/2011	2	172-173
Compare large bead (5.78um diameter) to a small bead (0.97um diameter) with respect to the # of beads required to detect a ring in a dried drop. (3uL)	1/11/2011	2	177-179
Quantify # of NTA surface groups on 1um red particles by incubating with FITC-labeled 6xHis tags on 5-laser flow cytometer	1/19/2011	2	180-181
EDC-couple NTA to carboxy beads in varying ratios and quantify surface by fluorescamine absorbance detection of unbound NTA-lysine in supernatant.	1/26/2012	3	1-2

Compare limits of detection in a 3-particle assay using 7 different batches of beads	1/27/2012	3	3-7
Determine if pre-incubating FeOx-NiNTA particles with varying amounts of 6xHis affects limit of detection of 3-particle assay	1/29/2012	3	8-9
Alternative drop design for incorporating with "Extractionator"	1/29/2011	3	10-11
Determine if adding FITC-6xHis to the assay lowers limit of detection	1/30/2011	3	12-13
Determine if aggregation alone is sufficient to cause a shift in ring color as opposed to relying on a magnet	2/1/2011	3	15-20
Detemine how adding varying amounts of glycerol to a 3-particle assay affects ring formation and image appearance	2/1/2011	3	21
Characterize # NiNTA per PS particle by titrating with FITC-6xHis and running on flow cytometer	2/2/2011	3	22-23
Evaluate most recent samples from Keersten (SMCC-coupled amine beads, 100% NiNTA coverage) for [] on coulter counter and ring formation on plain glass	2/3/2011	3	24
Determine if pre-incubating PS bead with 6xHis lowers 2-particle assay limit of detection.	2/4/2011	3	25-29
Evalaute limit of detection in 3-particle assay using latest beads from Keersten that were surface modified using SMCC method and active ligand synthesized by Josh S. and 2-mercaptoethanol as backfill. Five coverage ratios: 50%, 10%, 1%, 0.1%, & 0%	2/9/2011	3	31

Comparisons of HRP-II concentration vs AuNP concentration	2/15/2011	3	32
Zeta potentials of EDC-coupled PS-COOH beads	2/28/2011	3	33
Evaluate latest PS particles obtained from Chemistry (one-step EDC coupled red beads @10%, 50%, 100% NiNTA coverage with aminoisopropanol as the inactive ligand in 2-particle assay and PLH as target	2/28/2011	3	36-41
Determine if adding MES buffer to two-particle assay mitigates non-specific interactions observed in 2/28 & 3/2 studies	3/3/2011	3	42
Determine if adding NaCl to H2O or MES mitigates non-specific binding between the PS-NiNTA bead and FeOx-NiNTA in presence of rcHRP-II	3/4/2011	3	43-44
Determine if rcHRP-II antigen generates same kind of non-specific binding as seen above using H2O, PS-NiNTA (10% NTA coverage), and starting [PS-NinTA]=1.6x10^6/uL	3/4/2011	3	45
Compare non-specific binding in two-particle assay using FeOx-NTA vs FeOx-NiNTA vs Sicaster-M-NiNTA	3/7/2011	3	46-47
Use flow cytometry to quantify non-specfic and specific binding between FeOx particle and PS particles having various surface chemistries in the presence of PLH	3/8/2011	3	48-49
Determine how using a Tris buffer affects non-specific binding in a 2-particle assay	3/8/2011	3	50
Ring assay with salt-aged particles	3/10/2011	3	53-55

Piranha versus H2O -treated slides using 0.5uL of PS-COOH beads	3/19/2011	3	57-58
Effect of varying distance between magnet and drop: 435nM PLH vs H2O	3/20/2011	3	59-60
Drop assay with "charge neutralized" particles: 435nM PLH vs BNTII	3/21/2011	3	61-62
Idea for amplification strategy in drop diagnostic	3/27/2011	3	66
Quantify particle-particle interactions on the flow cytometer and determine effect of solution ionic strength and presence of rcHRP-II or PLH	3/29/2011	3	67-68
Idea for amplification strategy in drop diagnostic	3/30/2011	3	71
Flow cytometry experiments to evaluate specific and non-specific interactions	4/8/2011	3	76-89
Particle summary table	4/20/2011	3	91
Evaluate particle size distributions on Coulter Counter before/after incubation with rcHRP-II at varying concentrations	4/23/2011	3	92-93
Evaluate non-specific binding of a 4-particle system under flow cytometry in presence of target (rcHRP-II) vs no target (buffer)	4/26/2011	3	94-101

127

Evaluate particle-particle interactions in functionalized 4-particle system with flow cytometry in presence of rcHRP-II or buffer	5/2/2011	3	102-108
Determine emission spectra for various particles exciting at each of the 5 wavelengths used by the 5-laser flow cytometer	5/5/2011	3	109-111
Determine minimum [Dynal-CoNTA] required to completely bind a given [rcHRP-II]	5/10/2011	3	113-114
Determine if MF-COOH particles form rings	5/10/2011	3	115
Evaluate liposomes under fluorescence microscopy and flow cytometry	5/16/2011	3	116-123
Functionalize PS beads with NiNTA with a PEG linker via toxyl chemistry	5/20/2011	3	124
Evaluate ring formation with MF-plain beads in H2O on PEG slide vs regular glass slide vs (+)-charged glass slide	5/20/2011	3	125-127
Evaluate ring formation of a variety of particle types	5/23/2011	3	128
Demonstrate target-mediated cross-linking between capture and reporter bead using flow cytometry.	5/25/2011	3	129-133
Characterize binding capacity of NiNTA functionalized beads from Keersten (6/6): MF-NiNTA (FITC), PMMA-NiNTA (CY3), PS-NiNTA (FITC)	6/8/2011	3	135-139

Ni content of several functionalized bead types via ICP	6/9/2011	3	141
Determine binding capacity of Dynal-CoNTA beads for FITC-6xHis tags and characterize fluorescence on flow cytometer	6/18/2011	3	142-147
Demonstrate proof-of-concept sandwich ELISA drop diagnostic using NiNTA-Atto550 as the reporter	6/24/2011	3	148-151
EDC-couple Lys-NTA ligand to MF-COOH beads	7/6/2011	3	152
Functionalize MF-COOH beads with NiNTA or aminopropanol via EDC/sulfo-NHS using a modified protocol (different from the one KR has been using)	7/8/2011	3	153-155
Try incorporating spacer in MF-COOH NTA conjugation. Found a paper that used DHLA as spacer on quantum dots. DHLA has a thiol group at one end, so try making beads thiol reactive using BMPH	7/14/2011	3	156-157
Aggregation studies with Dynal Co-NTA using Coulter counter and phase contrast microscopy	7/20/2011	3	159-169
Conjugate Josh Schwartz' ligand (thiolated NTA with 3 PEG groups) onto BMPH modified MF-COOH beads	7/25/2011	3	170
Discussions with Ray Mernaugh about antibody conjugations	7/27/2011	3	171
Calculation of Dynal bead diffucion coefficient	7/28/2011	3	172

Nickel ICP procedure and initial studies, including zeta potential measurements	7/29/2011	3	173-176
Particle -Ab conjugation with Ray Mernaugh	8/3/2011	3	178
Using EDC/sulfo-NHS chemistry, conjugate Lys-NTA ligand to several different types of particles under two different conditions: pH 6 (100mM MES buffer) and pH 9 (200mM borate buffer). Confirm conjugation via zeta & ICP	8/7/2011	3	179-180
Establish baseline zetas as function of pH for different beads	8/10/2011	3	181
Determine which is better bead for conjugating Ab's: PS vs MF, and optimize conjugation conditions (pH, Ab:bead ratio)	8/10/2011	3	182-183
Correspondence with MF bead vendor (miroparticles, Gmbh)	8/16/2011	3	184
Demonstrate proof-of-concept sandwich ELISA drop diagnostic using NiNTA-Atto550 as the reporter.	6/24/2011	4	
Conjugate anti-HRP to MF-COOH beads based on condition range established in 8/10-8/12 experiment.	8/16/2011	4	
Repeat MF-antiHRP conjugation using conditions established in 8/16/11 conjugation optimization experiment.	8/23/2011	4	
Optimize MF-NTA conjugation for [EDC/NHS] and [lys-NTA].	8/29/2011	4	

Image particle distributions in evaporating drops under OCT.	8/31/2011	4	
Goniometer measurements.	9/2/2011	4	
Determine what detergent is most effective at blocking non-specific antibody binding to MF beads.	9/4/2011	4	
Repeat of 9/4 experiment wuth subset of agents: Triton X-100, glycerol, CTAB, BSA, & Casein.	9/6/2011	4	
Conjugate MF-PEG-NTA-Ni with dPEG-SATA reagent using hydroxylamino HCL to deprotonate the thiol.	9/12/2011	4	
Measured Ni content using ICP of PSg-PEG-NiNTA beads, which have been functionalized starting with PS-COOH, EDC/NHS couple BMPH,SH-PEG8-COOH, EDC couple Cys-NTA, then charge.	9/9/2011	4	
Determine if pH (9 or 10) and EDC vendor (Sigma v Pierce) affects the MF-NTA conjugation efficiency. Confirm filtration plates effect on study outcome.	9/7/2011	4	
NOTES	9/16/2011	4	
Optimize parameters for 2 particle assay using MF-PEG-NiNTA and Dynal-CoNTA.	9/18/2011	4	
NOTES	9/20/2011	4	

Develop MF-PEG-NTA-Ni beads using MF-MAL + thiol-PEG-thiol + MAL-NTA.	11/2/2011	4	
Characterization of MF-PEG-NTA-Ni by DLS & Zeta. Performed by Joel.	11/2/2011	4	
Characterize MF-PEG-NTA-Ni beads by measuring aggregation in presence of HRP and HRP+imidizole.	11/9/2011	4	
Develop MF-mPEG as a control.	11/9/2011	4	
ELISA protocol from Keersten Ricks.	11/10/2011	4	
Perform ELISA to quantify MF-PEG-NTA-Ni binding capacity for rcHRP-II.	11/10/2011	4	
NOTES	11/14/2011	4	
Follow-up ELISA to quantify HRP binding capacity of MF-PEG-NTA-Ni beads.	11/17/2011	4	
ICP results	12/12/2011	4	
Develop MF-PEG-NTA-Ni beads using MF-MAL + thiol-PEG-thiol + MAL-NTA. Smaller thiol-PEG-thiol (8 units vs 111 units). Reduced SH-PEG-SH under more ideal conditions.	12/9/2011	4	

Quantify how much labeled 6xhis the MF-PEG-NTA-Ni particles can bind.	12/14/2011	4	
SEM imaging (Joel).	12/14/2011	4	
Determine if the MF-PEG-NTA-Ni beads surface-modified on 12/9/11 bind to Dynal-NTA-Co beads in the presence of rcHRP-II.	12/16/2011	4	
The paper, "Complex Protein Patterns in Drying Droplets" indicates that polystyrene particles generate more pronounced ring formations in NaHCO3 buffer than in phosphate buffers. Experiment intended to determine if this observation is found with droplets containing MF-MAL particles.	12/20/2011	4	
Using same particles as 12/20 experiment, evaluate particle distributions when dried on PEG slide.	12/22/2011	4	
Repeat MF-PEG-NTA-Ni conjugation following the 12/9/11 protocol.	1/2/2012	4	
Conjugate MF-PEG-NTA-Ni particles with varying stoichiometric ratios of SH-PEG-SH: SH-mPEG.	1/4/2012	4	
NOTES	1/10/2012	4	
NOTES	1/18/2012	4	
Summary of recent observations.	1/19/2012	4	

Determine if MF-plain beads bind Ag(I) and/or Au(III) readily just as they do Ni(II).	1/20/2012	4	
zeta measurements	1/21/2012	4	
Determine zeta potential of MF-plain (nile blue) particles as a function of pH. Also determine for a given pH whether or not MES vs H20 affects zeta potential.	1/24/2012	4	
Optimize conditions in which MF-plain beads non-specifically adsorb Ag(II) to their surface.	1/26/2012	4	
Determine if salt can be used to block non-specific binding of nickel to the surface of MF-MAL beads in different pH's and buffer systems.	1/28/2012	4	
Given the ICP date from 1/28 re-try conjugation following a revised protocol similar to that used on 12/9/11 and incorporate varying amounts of backfill ligand. Also want to charge a subset of particle with zinc.	1/29/2012	4	
Determine if pH affects ring formation with MF-plain	1/29/2012	4	
zeta measurements	1/30/2012	4	
Quantify 6xhis binding capacity of the MF-PEG-NTA-Ni particles with varying amounts of imidizole as quencher. Compare to MF-PEG-NTA-Zn and Dynal-CoNTA as positive control.	1/30/2012	4	
Determine if MF and PMMA beads non specifically bind to Dynal beads in drop assay.	1/31/2012	4	

Measure background metal adsorption of MF-MAL (FITC) and MF-MAL (RB) whhen charging with NiCl2 on ZnSO4 in MES.	1/31/2012	4	
Do Ellman's assay to quantify active maleimide groups on MF beads.	2/6/2012	4	
Evaluate MF-plain (nile blue) and MF-COOH (nile blue) metal binding characteristics with Cobalt, Silver, & Nickel.	2/13/2012	4	
Determine EDTA molarity required to strip Co off Dynal beads. This technique can then be used to determine how tightly metal ions are associated to other particle surfaces using data from this experiment as a standard.	2/14/2012	4	
Incubate MF-COOH (nile blue) beads with AgNO3	2/16/2012	4	
SEM imaging (Joel).	2/22/2012	4	
Quantify SH-PEG-SH (MW = 2,000) binding to AuPS particles (1um).	2/24/2012	4	
Quantify SH-PEG-RB (MW = 2,000) binding to AuPS particles (1um).	2/28/2012	4	
Follow-up to 2/28. Re-try quantifying SH-PEG-RB binding to AuPS.	2/29/2012	4	
Group meeting.	3/9/2012	4	

zeta measurements	3/5/2012	4	
Graft SH-PEG-RB and SH-PEG-SH to AuPS (Micromod) using place exchange approach. That is, conjugate a saturated, monolayer of SH-PEG-RB first, then exchange a certain % with SH-PEG-SH.	3/1/2012	4	
Further develop protocol to plate gold shell on PS-NH2 particles.	3/10/2012	4	
Further develop protocol to plate gold shell on PS-NH2 particles.	3/16/2012	4	
Develop gold-decorated polystyrene beads by covalently binding AuNPs to carboxylated PS via thiol groups.	4/21/2012	5	
Quantify how much labeled 6xhis (FITC) the PS-AuNP-NTA-Ni particles can bind.	5/3/2012	5	
cofee ring capture assay limit of detection.	5/3/2012	5	
Perform multi-particle ring assay titration using PS-AuNP-NTA-Ni particles functionalized on 4/21 with rcHRPII as the target.	5/9/2012	5	
Determine if LiCL present in evaporating droplets containing 1um PS-COOH particles causes same problems that NaCl does.	5/16/2012	5	
Perform multi-particle ring assay titration using PS-AuNP-NTA-Ni functionalized on 4/21 with poly-L-histidine as the target.	5/25/2012	5	

Antibody studies with Ray Mernaugh.	5/18/2012	5	
Proof of concept study using Dynal-NTA-Co and a labeled antibody in a ring assay with rcHRPII as target.	5/27/2012	5	
Assay with Dynal-NTA-Co particle and anti-HRP-labeled qdot using rcHRP-II as target.	5/29/2012	5	
Notes		5	
polystyrene Core -Au Shell particle Density (Zach)	6/1/2012	5	
Use flow cytometry to confirm cross linking between Dynal-NTA-Co and QD-arcHRPII particles.	6/3/2012	5	
Determine zone of equivalence for Dynal-NTA-Co: rcHRPII titration.	6/13/2012	5	
Determine effect of Tween 20 concentrationon drop formation with Dynal-Co(II)NTA particles in water.	6/15/2012	5	
Determine if the most recent gold-coated PS particles from CG form rings, "1X" Au.	6/25/2012	5	
Check ring formation using gold-PS particles received from CG designated as "2X"	6/26/2012	5	

Aggregation assay with rcHRPII as target to determine if latest PS-Au-Ni(II)NTA particles bind target and compare aggregation behavior to Dynal-Co(II)NTA positive control.	7/3/2012	5	
Surface modify gold-on-PS from CG with thiol-NTA ligand. Additionally, surface modify the control particle with mPEG8-SH.	7/27/2012	5	
fluid mechanics notes	7/14/2012	5	
Conjugate biotinylated-anti-HRPII antibody to Dynal-streptavidin beads.	7/16/2012	5	
Verify Dynal-PS cross linking using flow cytometry.	7/19/2012	5	
Conjugate reduced anti-HRPII antibody to PS-Au particles.	7/18/2012	5	
Determine how drop radius scales with drop volume. (Laura)	7/23/2012	5	
Verify antibody on Dynal and PS-Au particles conjugated with anti-HRPII on 7/16 and 7/18	7/24/2012	5	
distribution of particles in OCT drops (zach)	6/28/2012	5	
goniometer data (zach)	7/26/2012	5	

Determine if our hypothesis of why some particles accumulate on the drop surface can be used to reproducibly affect ring structure order using 3 different particles with different density.	7/30/2012	5	
Passively adsorb streptavidin to 1um particles evaluating effect of pH and buffer	7/31/2012	5	
Aggregation studies	8/1/2011	5	
Determine effect of pH on ring formation using Silica particles in water.	8/4/2012	5	
Conjugate biotinylated-anti-HRPII antibody to red fluorescent PS-neutravidin and pink fluorescent magnetic-Streptavidin particles.	8/12/2012	5	
Couple anti-HRP antibody to Sepharose-NHS beads.	8/12/2012	5	
Evaluate the effect of different buffering systems on the cross-linking between PS-biotin particles and sepharose-streptavidin beads.	8/13/2012	5	
Conjugate streptavidin to sepharose-NHS beads.	8/13/2012	5	
Try coffee ring assay using 4-different formats. A) Sepharose-streptavidin + PS-biotin in LiCl, sucrose, and LiCl+ sucrose B) Sepharose-antiHRP + HRP + PS-Ni(II)NTA C) Sepharose-antiHRP + HRP + PS-antiHRP D) Dynal-CoNTA + HRP + PS - Ni(II) NTA and PS-AuNP (200nm)	8/19/2012	5	
Determine to what extent variability in polystyrene particle density could be causing the particle flow observations under OCT that shows particles accumulating at the drop surface. Use Ficoll Paque Plus density gradient to verify PS density.	8/17/2012	5	

Try a new coffee ring assay format in which a liquid phase biotin-Ni(II)NTA reagent interacts with target (rcHRP-II) first, and is then captured by streptavidin/neutravidin-coated particles.	9/3/2012	5	
Try a new coffee ring assay format in which a biotin-biotin dimer serves as the target molecule that crosslinks two streptavidin coated particles.	9/3/2012	5	
OCT procedure	8/24/2012	5	
OCT data summary	11/30/2012	5	
OCT parameters	12/1/2012	5	
Evaluate whether interacting biotinylated antiHRPII with target HRPII first will facilitate cross-linking of two particles	9/29/2012	6	2-3
Discussions with Ray Mernaugh about failure in 9/29 experiment	10/1/2012	6	4-5
Check viability of rcHRP-II from CTK Biotech and neutravidin beads from Invitrogen	10/2/2012	6	6-7
Idea for using OCT and coffee ring phenomenon as a diagnostic tool	10/3/2012	6	8
Project status and next steps	10/5/2012	6	9

Verify rcHRP-II (from CTK Biotech) viability spectrophotometrically with AuNP-Ni(II)NTA (synthesized by Chris Gulka)	10/6/2012	6	10-11
Measure the dynamic viscosity of Ficoll-Paque and diluted Ficoll. This data will be needed to calculate settling velocities in Ficoll solutions	10/10/2012	6	12
Experiment to demonstrate crosslinking between Dynal-Co(II)NTA and glutathione sepharose beads via rcHRP-II (from CTK Biotech) containing a GST tag.	10/12/2012	6	13-14
Aggregation assay using polyclonal goat antiHRPII Ab from CTK with both Dynal-streptavidin and PS-neutravidin beads	10/14/2012	6	15-16
Prepare particle solutions in Ficoll for OCT experiments	10/15/2012	6	17-18
Characterize protein binding (rcHRP-II) of particles conjugated with biotinylated goat, polyclonal anti-HRPII	10/19/2012	6	19-22
Conjugation of antiHRPII and antiM13 to PS-neutravidin and agarose beads	10/21/2012	6	23
Verify PS-antiHRP (polyclonal from 10/21) aggregate in presence of rcHRPII and PS-antiM13 (as control)	10/27/2012	6	24-26
Verify I can get particles to aggregate using biotinylated IgG (ie test hypothesis 5a from pg 24) and evaluate different blocking agents	10/29/2012	6	27-31
Since Spherotech PS-streptavidin seem to work best, try functionalizing with biotinylated antiHRP-II (polyclonal) or antiM13 and re-do aggregation assay with rcHRP-II	10/30/2012	6	32-35

Biotinylate antiHRP mAb and antiM13 and couple to dynal-streptavidin and PS-neutravidin beads	11/1/2012	6	36-37
Aggreagation assay with the PS-proteinG, PS-neutravidin, and dynal-streptavidin beads	11/4/2012	6	38-43
Given lack of success with rcHRP-II, switch to M13K07 target. First try coupling with passive adsorption, then biotinlyation, and do aggregation assay	11/5/2012	6	44-48
Conjugate antiM13 to NHS-Sepharose 4 Fast Flow beads	11/9/2012	6	49
M13K07 phage characteristics	11/9/2012	6	50
Possible control particles	11/9/2012	6	51-53
Assay to determine if PS-antiM13 (passivle adsorbed, 11/5) will cross-link to Sepharose-antiM13 (11/9) in presence of M13, Seph-OH as control	11/11/2012	6	54-55
Conjugate biotinylated antiM13 (11/5/12) to PS-neutravidin beads	11/12/2012	6	55-'63
Using the same PS-antiM13 beads used in the 11/12 aggregation assay, cross-link these to sepharose-antiM13 or sepharose-OH as control in presence of M13	11/14/2012	6	64-66
Re-do aggregation assay with PS-antiM13 and Dynal-antiM13 but this time using different solution conditions	11/17/2012	6	67-71

Try coffee-ring assay with PS-antiM13 and Dynal-antiM13	11/20/2012	6	72
Passivle adsorb free biotin to PS-COOH	11/21/2012	6	73-74
Invention idea	1/4/2013	6	76-77
Evaluate flow patterns (Marangoni vs reverse Marangoni) of PS-COOH particles in different solutions and on different substrates	1/6/2013	6	78-84
Try stimulating the top of a 2.5uL drop using a Gaussian IR laser aligned with the drop to induce reverse Marangoni flow	1/17/2013	6	85-87
Try inducing regular Marangoni flow by using two lasers simultaneously	1/23/2013	6	88-89
Using same set-up as 1/23, Zach tried changing pulse and frequency settings and laser placement/toggle to induce Marangoni flow	1/25/2013	6	90
Goniometer operating instructions (from Alex Short)	1/31/2013	6	91
Since we weren't able to effectively induce Marangoni flow (see 1/23, 1/25), now want to see if we can start with conditions in which reverse Marangoni is present and then either enhance or inhibit based on IR laser placement (center versus edge). We've seen before that the presence of either NaCl or glycerol in teh drop produces reverse Marangoni flow on glass (1/6) - so we'll use this as starting condition	2/8/2013	6	92-93
Determine effect of heating/chilling drop solution before depositing on slide at ambient conditions	2/13/2013	6	94

Using a temperature controller and Flir IR camera to verify temperatures, determine the slide temp regime that promotes Marangoni versus reverse Marangoni flow.	2/15/2013	6	95-96
Determine how DMSO in water drops affects secondary flow patterns	2/16/2013	6	97-98
Determine effect of DMSO on dried patterns of drops	2/21/2013	6	99-100
List of particles on hand that could be used in OCT/ring formation experiments	2/22/2013	6	101
Further investigate effects of DMSO by comparing different particle sizes and substrates: glass vs PDMS -- first noticed center accumulation in drop	2/22/2013	6	102-105
Investigate flow fields with OCT on ITO vs glass vs PDMS for different solutions: betaine, NaCl, Ficoll, glycerol, LiCl	2/27/2013	6	106-116
Conjugate biotin and streptavidin to sepharose-NHS beads	2/28/2013	6	117-119
Verify presence of streptavidin and biotin on sepharose beads and Xenopore slides	3/1/2013	6	120-121
Passively adsorb antiM13 and avidin to piranha treated slides	3/2/2013	6	122
Evaluate flow fields with OCT of control particle solutions on PDMS from 2/22-2/23 experiments.	3/2/2013	6	123-124

Conjugate biotin-hydrazide to sepharose-NHS beads	3/10/2013	6	126
Try cross-linking sepharose beads to amine slide (Arrayit) and sepharose-biotin beads to a streptavidin slide	3/10/2013	6	126-129
Conjugate anti-M13 Ab to sepharose-NHS, couple antiM13 to streptavidin slide, try to cross-link	3/11/2013	6	130-131
Determine if M13K07 phage can cross-link sepharose-antiM13 (made 3/11/13) to a slide having an anti-M13 surface and cause beads not to migrate toward center of an evaporating drop	3/13/2013	6	132
Using Dynal-CoNTA beads and rcHRP-II, determine if reverse Marangoni flow on PDMS can accumulate biomarker-mediated aggregates att eh drop center resulting in a concentration-dependent signal	3/14/2013	6	133
Invention idea using counter-rotating eddies for solution-based signal generation to indicate presence of biomarker	3/14/2013	6	133-137
Re-do 3/14 experiment, but using Dynal-antiM13 particles and M13 phage to induce aggregation and then see if aggregates collect at the drop center on PDMS, glass, and ITO slides	3/15/2013	6	139-145
As follow-up to 3/15 experiment, determine what glycerol % is best for promoting center accumulation of aggregates consisting of Dynal-antiM13+M13.	3/21/2013	6	146-150
Run titration of PS-antiM13 against M13 to evaluate particle specificity/sensitivity against target	3/25/2013	6	151-153
Proof-of-concept to demonstrate detection of biomolecular interaction at the interface of counter rotating currents in an evaporating drop of miscible solutions	3/26/2013	6	154

Optimize and characterize limit of detection of drop assay in which reverse Marangoni flow concentrates signal at drop center	3/27/2013	6	155-162
Method for quantifying artifact in OCT imaging of evaporating drops	3/30/2013	6	163